The catalysis of CO2 electroreduction and related processes

Varela Gasque, Ana Sofia; Chorkendorff, Ib; Stephens, Ifan

Publication date:
2013

Document Version
Publisher's PDF, also known as Version of record

Citation (APA):
Varela Gasque, A. S., Chorkendorff, I., & Stephens, I. (2013). The catalysis of CO2 electroreduction and related processes. Department of Physics, Technical University of Denmark.

Technical University of Denmark

DTU

The catalysis of CO_2 electro-reduction and related processes

Ph.D. Thesis

Ana Sofia Varela

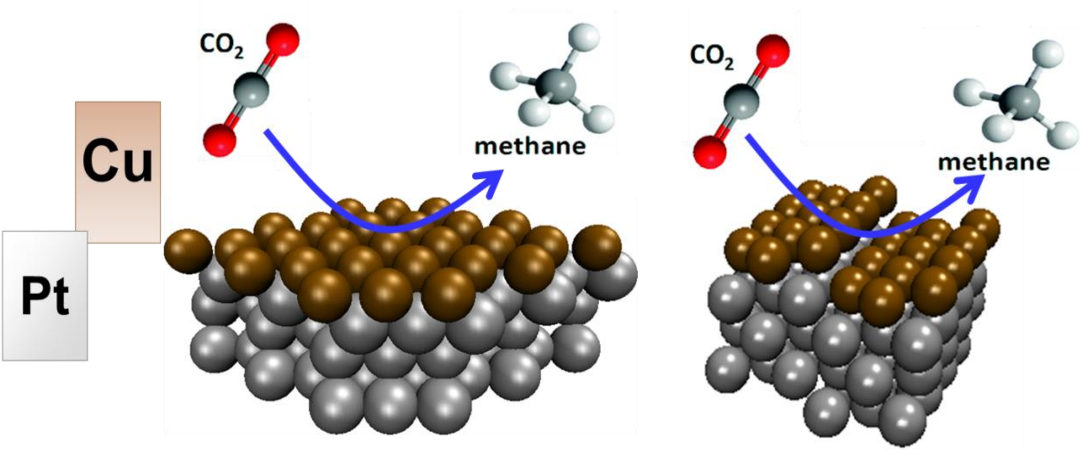

CINF
Center for Individual Nanoparticle Functionality

CASE
Catalysis for Sustainable Energy

TECHNICAL UNIVERSITY OF DENMARK

Catalysis of CO_2 eletro-reduction and related processes

Ph.D. Thesis

Ana Sofía Varela Gasque

01/04/2013

Supervisor: Professor Ib Chorkendorff
Assistant Professor Ifan Stephens

Center for Individual Nanoparticle Functionality.
Department of Physics

Preface

This Thesis is submitted in candidacy for the Ph.D. degree in Physics for the Technical University of Denmark. The work included here has been carried out in Center of Individual Nanoparticle Functionality (CINF), under the supervision of Professor Ib Chorkendorff, Professor Søren Dahl and Assistant Professor Ifan Stephens, from the 1st of April 2010 to the 31st of march 2013.

CINF is funded by The Danish Research Foundation, while my Ph.D. is part of Catalysis for Sustainable energy (CASE) research initiative founded by the Danish Ministry of Science, Technology and Innovation.

Acknowledgements

First of all I want to thank Professor Søren Dahl for giving me the opportunity to come to Denmark to work in an interesting project and to have this amazing life experience. I also thank Professor Ib Chorkendorff and Assistant Professor Ifan Stephens, for all the discussions we have had together and the good guidance they have given me throughout this project. I also appreciate a lot the opportunity they have given me to present my work in international conferences and to participate in summer schools where I've learned a lot.

I feel very lucky for having had the opportunity to work in a highly cooperative center as CINF. It has been a pleasure to work with all of you. Especially it has been great to share the work with all the people in the electrochemistry lab, I have learned from each one of you and enjoy your friendship. I want to acknowledge Dr. Wei Tang who started the CO_2 reduction project and taught me the basis for my Ph.D project. I also thank Dr. Aliaksandr Bandarenka who designed the fantastic set up I have been working on and taught me how to work with single crystals. I also acknowledge the good work of Jan Patrick Scholer, our glassblower, who has made great electrochemical cell incorporating our crazy ideas.

I really want to acknowledge all the support I have had from Zarko Jovanov, thank you for sharing with me the CO_2 reduction project, all the challenges, frustrations and the few good results that have come with it.

I want to thank Zarko Jovanov, Dr. Maria Escudero, Dr. Federico Calle-Vallejo, Elisa Paoli and Rasmus Frydendal for helping me proofread this Thesis and to Brian Knudsen for writing the *Resumé* in Danish. I also thank

Dr. Christian Schlaup for the STM images and the discussion about the results on the copper overlayers. I thank Mohammedreza Karamad for the structures figures and the discussion of the DFT results.

Furthermore, this past 3 years would not have been the same without all my friends that have been my family away from home. Especially, I want to thank Alan, Wei and Paco who helped me get started in my life in Denmark. I also thank Billie and Juanma that have been there for me all this time. It has been also great to have meet Elisa, thank you for your support these past six months, you are truly a good friend. I also want to thank Daniela, Lourdes, Maricruz and Alondra it has been great to have someone that understands the good and bad things of being so far from home. I want to thank Tao because it would be foolish not to admit that my life in Denmark would have been different, probably for the worse, if you hadn't been a part of it.

Finally, I want to thank my family and friends that, regardless of the distance, have been a part of my life. I miss you a lot, but it is also good to know that no matter where I am I have your support and friendship. In particular I thank Daniel and my parents, for all those skype talks and visits; I could not have done this without your encouragement. I dedicate this Thesis to you

Ana Sofia Varela

April 2013

Abstract

The present PhD research is focused on the electrochemical reduction of CO_2 to hydrocarbons. This process, coupled to renewable energy sources, such as wind and solar power, is an attractive alternative for the production of synthetic carbon neutral fuels and fine chemicals. Although many metals have been studied as catalysts for CO_2 electro-reduction, copper is the only one at which hydrocarbons are produced in considerable amounts. Hydrocarbon formation, however, requires a high overpotential (~1 V), which implies big energy loses. Furthermore, the selectivity of copper towards a particular product is low and a mixture of products is obtained. In order to improve the catalytic process, a better understanding of the factors affecting both the selectivity and the energy efficiency of this reaction is needed.

First of all, this work aimed at studying different polycrystalline copper surfaces as catalysts for the CO_2 electrochemical reduction. This allowed us to explore the effect of the surface morphology on the catalytic activity of copper. Our results suggest that the presence of steps and kinks on rough copper surface favors the CO_2 electrochemical reduction over the hydrogen evolution reaction. Furthermore, on rough surfaces the formation of ethylene is enhanced over methane production.

The next step has been studying the electrochemical reduction of CO_2 onto Cu overlayers on Pt single crystals. The purpose this work was to study the effect of having a strained Cu surface on the efficiency and selectivity of the reaction. Furthermore, by studding different crystal facets we can obtain information about the role of steps. Interestingly, the selectivity towards hydrocarbons on the copper overlayers is much lower than the obtained on polycrystalline copper. These results are consistent with a linear combination of Pt and Cu rather than an expanded copper surface. Furthermore, electrochemical scanning tunneling microscopy (EC-STM) studies indicate that in the presence of CO the Cu overlayer changes from a nearly flat to a granular structure exposing part of the Pt surface. These results illustrate the importance of *in situ* measurements in order to gain an insight into the catalyst surface structure under reaction conditions. This knowledge can be crucial for the understanding of the catalyst reactivity.

Finally, this Thesis is focused on the formation of a Cu/Pt (111) overlayer, as well as near surface and surface alloys. These studies show that the reactivity of the Pt(111) depends on the location of the copper atoms. The presence of copper both on the first layer and in the surface alloy strengthens the interaction between Pt and its adsorbates. In contrast, Cu atoms located in the second layer or in the near surface alloy lead to the opposite effect. These results are very useful for the rational design of catalysts for a variety of processes, as has been demonstrated in this work for the CO electrochemical oxidation.

Resumé

Den foreliggende Ph.d. forskning fokuserer på den elektrokemiske reduktion af CO_2 til kulbrinter. Når denne proces kobles til vedvarende energikilder såsom vind- og solenergi er den et attraktivt alternativ for produktionen af karbon neutrale syntetiske brændsler og fine kemikalier. Selvom mange metaller er blevet undersøgt for deres katalytiske egenskaber i forhold til elektroreduktionen af CO_2, er det kun kobber der har vist sig at danne kulbrinter i anseelige mængder. Dannelsen af kulbrinter kræver dog et meget højt overpotentiale (~1 V), hvilket er ens betydende med store energitab. Ydermere er selektiviteten for dannelsen af produkterne på kobber lav og der dannes derved en blanding af de forskellige produkter. For at kunne forbedre den katalytiske proces kræves der større viden omkring de faktorer der påvirker både selektiviteten og energieffektiviteten.

Forskningen var først og fremmest målrettet studier af forskellige polykrystallinske kobber overflader som katalysatorer for den elektrokemiske reduktion af CO_2. Dette har tilladt os at udforske effekten af overflademorfologi på den katalytiske aktivitet af kobber. Vores resultater indikerer at tilstedeværelsen af steps og kinks på overfladen af ru kobber favoriserer den elektrokemiske reduktion af CO_2 frem for hydrogen udviklingsreaktionen. Ydermere er produktionen af ethylen højere en produktionen af methan på de ru overflader.

Det næste skridt har været studier af den elektrokemiske reduktion af CO_2 ved Cu overlag på en Pt enkeltkrystal. Formålet med dette arbejde var at undersøge selektiviteten og effektiviteten for reaktionen på et ekspanderet Cu overlag. Vi kan ydermere opnå viden omkring steps roller ved at studere forskellige krystalfacetter. Det er interessant at selektiviteten for dannelsen af kulbrinter ved kobber overlag er lavere end ved polykrystallinsk kobber. Disse resultater er konsistente med en lineær kombination af Pt og Cu og ikke et ekspanderet kobber overlag. Forsøg med et elektrokemisk-skanning-tunnel-mikroskop (EC-STM) har ydermere indikeret, at tilstedeværelsen af CO ændrer Cu overlaget sig fra at være næsten helt fladt til at have en granulær struktur, med den konsekvens at dele af Pt overfladen bliver blotlagt. Disse resultater illustrerer hvor essentielle *in situ* målinger er for at kunne vinde indsigt i katalysatorens overflade struktur under reaktionsbetingelser. Denne viden kan være af afgørende betydning for forståelsen af katalysatorens aktivitet.

Endeligt fokuserer denne afhandling på formationen af et Cu/Pt(111) overlag såvel som næroverflade legeringer og overfladelegeringer. Disse studier viser at reaktiviteten af Pt(111) afhænger af hvor kobber atomerne befinder sig. Tilstedeværelsen af kobber i og på overfladen og i første lag forstærker interaktionen mellem Pt og adsorbater. Som kontrast har Cu atomer i andet lag og næroverflade legeringen den modsatte effekt. Disse resultater er meget brugbare ved design af specifikke katalysatorer til forskellige processer og er demonstreret i denne afhandling for den elektrokemiske reduktion af CO.

List of papers

Paper 1:

The importance of surface morphology in controlling the selectivity of polycrystalline copper for CO2 electroreduction

Tang, W.; Peterson, A. A.; **Varela, A. S**.; Jovanov, Z. P.; Bech, L.; Durand, W. J.; Dahl, S.; Norskov, J. K.; Chorkendorff, I. *Physical Chemistry Chemical Physics* **2012**, *14*, 76.

Paper 2:

Design of an Active Site towards Optimal Electrocatalysis: Overlayers, Surface Alloys and Near-Surface Alloys of Cu/Pt(111)

Bandarenka, A. S.; **Varela, A. S**.; Karamad, M.; Calle-Vallejo, F.; Bech, L.; Perez-Alonso, F. J.; Rossmeisl, J.; Stephens, I. E. L.; Chorkendorff, I. *Angewandte Chemie International Edition* **2012**, *51*, 11845.

Paper 3:

Electrochemical Hydrogen Evolution: Sabatier's Principle and the Volcano Plot:

Laursen, A. B.; **Varela, A. S**.; Dionigi, F.; Fanchiu, H.; Miller, C.; Trinhammer, O. L.; Rossmeisl, J.; Dahl, S. *Journal of Chemical Education* **2012**, *89*, 1595.

Paper 4:

CO_2 electroreduction on well-defined bimetallic surfaces: Cu overlayers on Pt single crystals

Varela A.S., Schlaup C.G. Jovanov, P.J., Malacrida P., Horch S., Stephens I.E.L, Chorkendorff I. *In prepapration* (Not included)

Contents

Chapter 1

1. Introduction

1.1 The energy challenge

Probably the biggest challenge that society is facing today is to ensure the energy supply for future generations. During the last decade the primary energy consumption has increased dramatically reaching 16.3TW in 2011, representing a growth of 2.5% with respect to the previous year. In 2011, all of the increase in energy consumption took place in emerging economies, mainly in China which accounts for 71% of the total growth[1].

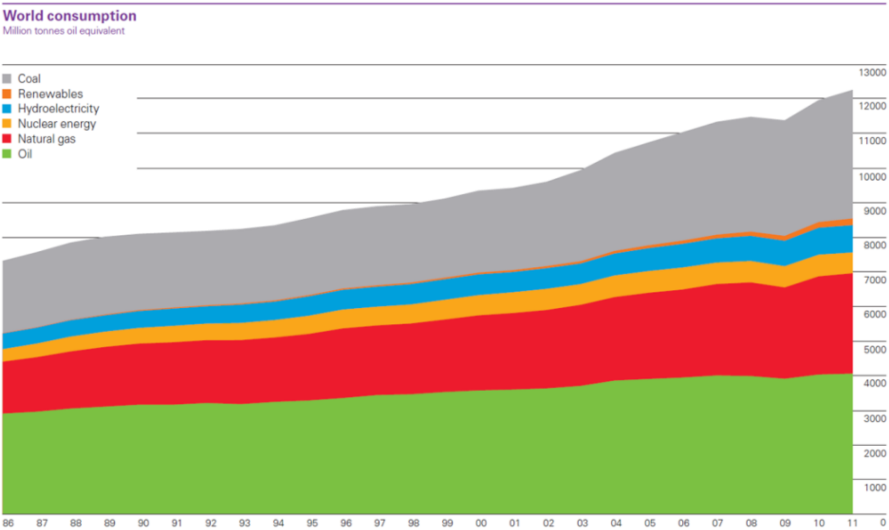

Figure 1.1: World's primary energy consumption in million tones equivalent, from 1986 and 2011. Figure from[1]

Fossil fuels still represent the main source of energy, accounting for 87% of the total production. However, from both an environmental point of view as well as availability of these resources, the need for other energy sources has become imminent. As is well known, fossil fuels are a limited resource. The proved reserves of oil would last only 54 years, at the production rate of 2011, while natural gas would last 63 years and coal 112. Furthermore, these resources are distributed unequally around the world, 48.1% of the proved oil reserves are in the Middle East whereas the reserves of the United State and European Union represent only 1.7% and 0.4% respectively. On the other hand, the US accounts for 20.1% of the oil consumption, the European Union for 15.9% while the Middle East represents 9.1%. According to this numbers, fossil fuels will not only run out in the not so distant future, but there are regions in the world that today rely on other countries to fulfill their energy requirements.

The need to achieve a secure and clean energy supply has encouraged new energy policies to promote lower energy consumption and usage of alternative energy sources. Under this scenario, renewable energies such wind and solar, play a crucial role as a CO_2 neutral alternative. Therefore the European Union has set the goal to increase the share of renewable sources in energy consumption to 20% in 2020[2]. Denmark has gone further, and in 2012 achieved a new energy agreement for increasing its share of renewable energies from 22% in 2010 to 35% in 2020. This will imply a reduction of 25% of the oil used in 2010 and a 60%

reduction of the coal consumption for the same period. This agreement also contemplates that Denmark should be independent from fossil fuels by 2050[3]. In this scenario electricity, produced mainly by wind power, will become the predominant energy carrier. Electricity production from wind and solar energy, however, fluctuates with the weather conditions and not necessarily matches the demand. Therefore to make the transition from an energy scheme dependent on fossil fuels to one based on renewable energies is crucial to find an efficient way of storing electrical energy[4].

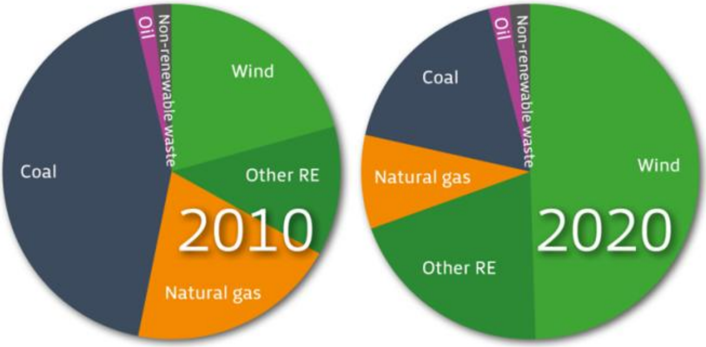

Figure 1.2: Electricity consumption by source in Denmark in 2010 and the expected for 2020. Figure from (Figure from [3])

One of the many options for storing electrical energy are batteries, however if we focus on figure 1.3 we can see that the energy density of such devices is considerably lower than that of the fossil fuels we have been using for the last decades.

Another option is to use the electrical energy to drive chemical reactions, which allows us storage of energy in chemical bonds[5].

This can be done by performing water electrolysis to produce hydrogen or by reacting water with CO_2 to form hydrocarbons. The second option is particularly attractive, since it can produce compounds with a high energy density such as methane and alcohols that can be used as energy carriers within in the existing technology[6].

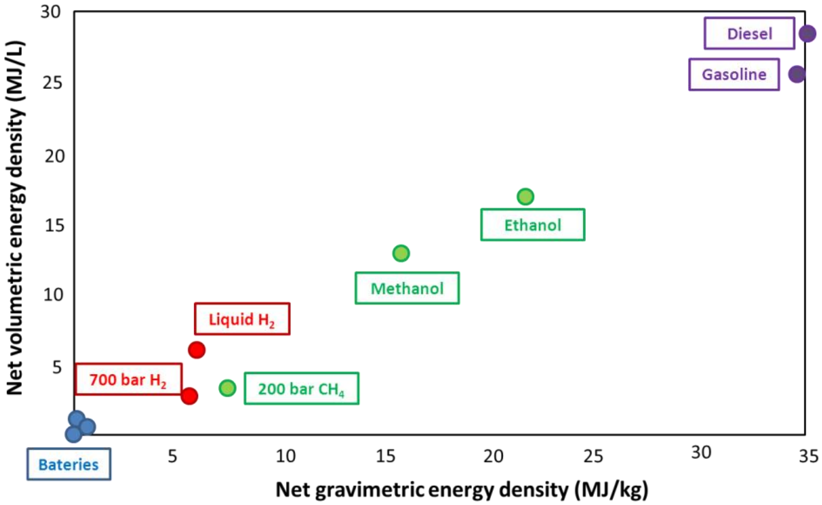

Figure 1.3: Volumetric energy density vs. gravimetric energy density of different energy carriers. (Figure adapted from[7])

1.2 CO_2 electrochemical reduction

There are different approaches to convert CO_2 to carbon based fuels, such as conventional heterogeneous catalysis to hydrogenate CO_2 into methanol using zinc and copper oxide as catalyst at high temperature and pressures. Another option is to use photosynthetic microorganisms, like algae, to transform solar energy into chemical energy.

The electrochemical approach allows mimicking the process occurring plants in which CO_2 and H_2O are converted into alcohols and hydrocarbons, but using electricity as a driving force instead of solar energy. When the electrical energy used for electro-reduction of CO_2 is generated from renewable sources, this process can be referred as *artificial photosynthesis,* since it involves the conversion of solar energy to carbon based fuels[8].

The electro-reduction of CO_2 is achieved by applying a potential difference between two electrodes in a device known as electrolyzer. When the potential difference is high enough, water oxidations occurs at the anode releasing protons and electrons, which are consumed in the cathode to reduce CO_2 and protons into hydrogen and hydrocarbons.

There are many different reactions that can occur at the cathode, depending on the catalyst and the reaction conditions. Some of them are shown below together with their equilibrium potentials:[9]

- $2CO_2 + 12H^+ + 12e^- \rightarrow C_2H_4 + 4H_2O$ $E_0 = 0.079$ V vs. RHE
- $CO_2 + 8H^+ + 8e^- \rightarrow CH_4 + 2H_2O$ $E_0 = 0.169$ V vs. RHE
- $CO_2 + 6H^+ + 6e^- \rightarrow CH_3OH + 2H_2O$ $E_0 = -0.030$ V vs. RHE
- $CO_2 + 2H^+ + 2e^- \rightarrow CO + H_2O$ $E_0 = -0.103$ V vs. RHE

- $CO_2 + H^+ + 2e^- \rightarrow HCOO^-$ $E_0 = -0.225$ V vs. RHE
- $2H^+ + 2e^- \rightarrow H_2$ $E_0 = 0.0$ V vs. RHE

While at the anode water is oxidized to evolve oxygen:

$$2H_2O \rightarrow O_2 + 4H^+ + 4e^-$$

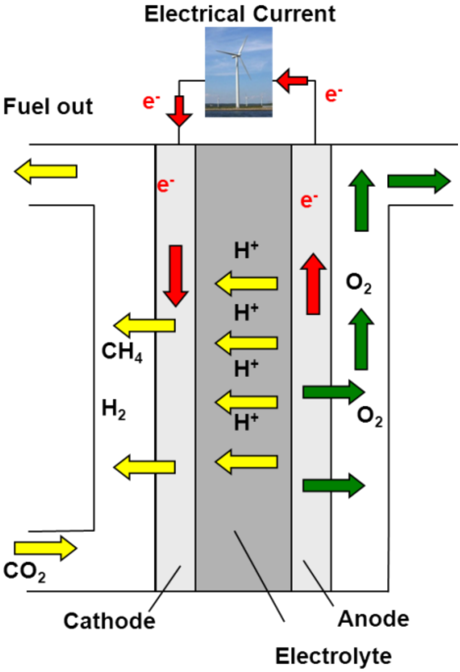

Figure 1.3: Schematic representation of an electrolizer for bulk CO_2 reduction.

According to the thermodynamics, CO_2 reduction products are formed at similar potentials as hydrogen. In practice, however, CO_2 is reduced at potentials below 0.0V and therefore the electro-reduction of CO_2 is accompanied by the formation of hydrogen.

Furthermore, the formation of hydrocarbons involves several electron transfers and intermediates making it a complex process, which requires a large overpotential.

The overall goal of studying the CO_2 electrochemical reduction is to understand how to selectively produce one of the many possible products at low overpotentials. For this purpose one can work with a homogenous catalyst[10], usually a transition metal complex dissolved in the electrolyte or a heterogeneous catalyst made of conductive material used as the reaction electrode. Many metals have been studied as heterogeneous catalysts for CO_2 electro-reduction in aqueous electrolytes, at which the reduction of CO_2 reduction is accompanied by hydrogen evolution reaction (HER).

Table 1.1 shows the selectivity, measured by Faradaic efficiency, of different metals towards the CO_2 electro-reduction. These results were obtained at a fixed current of $5mA/cm^2$. The potential at which this current was obtained depends on the activity of the catalyst. At a highly active catalyst the current of $5mA/cm^2$ is obtained at lower over potentials (less negative) than on catalyst with a low activity[9].

It is possible to classify the metals in table 1.1 in four groups according to the main products. There is a group of metals, such as platinum and nickel that are not active towards the CO_2 electro-reduction simply because they are highly active catalysts for the HER and therefore only protons are reduced at the cathode.

Me Tal	***E*** V vs RHE	***I*** mA/ cm^2	**Faradaic efficiency (%)**							
			CH_4	**C_2H_4**	**EtOH**	**PrOH**	**CO**	**HCOO**	**H_2**	**Total**
Ni	-1.18	5	1.8	0	0	0	0	1	89	92
Fe	-0.57	5	0	0.1	0	0	0	0	95	95
Pt	-0.67	5	0	0	0	0	0	0	96	96
Ti	-1.20	5	0	0	0	0	tr	0	100	100
Pb	-1.23	5	0	0	0	0	0	97	5	102
Hg	-1.11	0.5	0	0	0	0	0	99	0	100
Tl	-1.20	5	0	0	0	0	0	95	6	101
In	-1.15	5	0	0	0	0	2	95	5	100
Sn	-1.08	5	0	0	0	0	7	88	5	100
Cd	-1.23	5	1.3	0	0	0	14	78	9	103
Au	-0.74	5	0	0	0	0	87	1	10	98
Ag	-0.97	5	0	0	0	0	81	1	12	95
Zn	-1.14	5	0	0	0	0	79	6	10	95
Pd	-0.80	5	2.9	0	0	0	28	3	26	60
Ga	-0.84	5	0	0	0	0	23	0	79	102
Cu	**-1.04**	**5**	**33.3**	**25.5**	**5.7**	**3**	**1.3**	**9**	**20**	**103**

Table 1.1: Product distribution for the CO_2 electrochemical reduction on different metal (Adapted from [9])

There is a second group of metals that reduce CO_2 but cannot break the carbon-oxygen bond and the main product is formate. A third group of metals, where we find gold and silver, consists of those metals that can reduce CO_2 to CO, however, as they bind weakly towards CO it is not possible to reduce it any forward. On these metals the CO_2 reduction is accompanied by the HER generating a mixture of CO and H_2, also known *syngas*, which can be further reduced to hydrocarbons by Fischer-Tropsch catalysis.

$$(2n + 1)\ H_2 + n\ CO \rightarrow C_nH_{(2n+2)} + n\ H_2O$$

Finally, we can see that copper stands all by itself, being the only metal that produces hydrocarbons with high selectivity. However the reaction occurs at a high overpotential and gives a mixture of several products. Furthermore, it is not yet well understood how to control the selectivity of the CO_2 reduction towards the most desired products like methanol and ethylene[11].

1.2.1 CO_2 electro-reduction on copper

Since copper is the only metal that reduces CO_2 to hydrocarbons it has been widely studied as an electro-catalyst[12-22]. Different studies have shown that its efficiency and selectivity are strongly dependent on the reaction conditions, such as electrolyte[18], pH, temperature and working potential[15, 18].

Potential dependence

The product distribution as a function of potential was first studied by Hori and co-workers[14]. They observed that at potential less negative than -0.5V vs. RHE hydrogen is the only detected product, while CO_2 was only reduced at higher overpotentials (Figure 1.4). CO and $HCOO^-$ start to form at ~ -0.6V vs. RHE, reaching the highest efficiencies at around -0.8Vvs. RHE, which corresponds to an overpotential of about 0.9V. Hydrocarbons formation, predominately ethylene and methane, starts at -0.7V. Ethylene is the predominant hydrocarbon at between -0.7V and -0.9V while at -1.0V methane is the predominant product. The overpotential needed for producing high yields of hydrocarbons is ~ -1.0V, which represents an important energy loss.

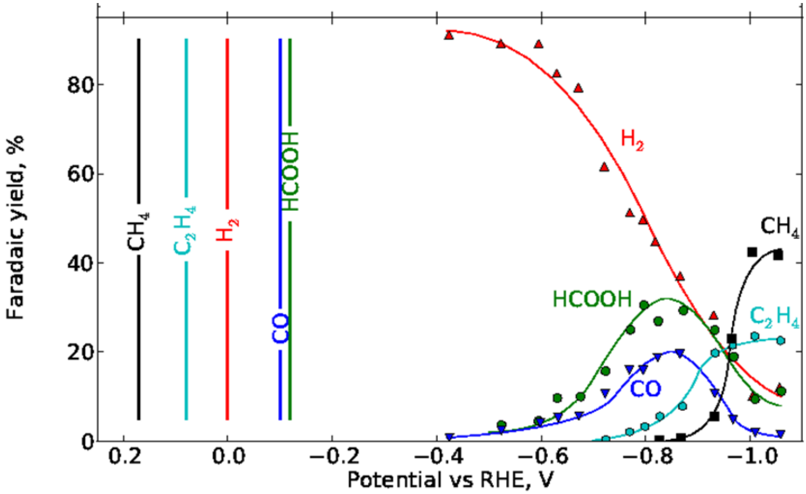

Figure 1.4: Product distribution as a function of potential obtained by Hori and co-workers. (Figure adapted from [23] data from[14])

More recently, Jaramillo and co-workers have studied the product distribution as a function of potential during the electrochemical reduction of CO_2 on copper electrodes[15]. They performed the reaction in a custom-made electrochemical cell that allowed a high concentration of reaction products in the liquid phase. They took advantage of these high concentrations and in combination with NMR, they were able to detect a total of sixteen reaction products.

Five of those sixteen products were reported for the first time. The potential dependence of the main CO_2 reduction products is consistent with the results from Hori *et al*. In addition, they found that the potential dependence for compounds with two or more carbon atoms is similar to that of ethylene, i.e. the efficiency towards these products had a maximum at around -1.0 V. On the other, methane production increased with overpotential. The different potential dependence between methane and ethylene suggests a different rate limiting step for the formation of these two products.

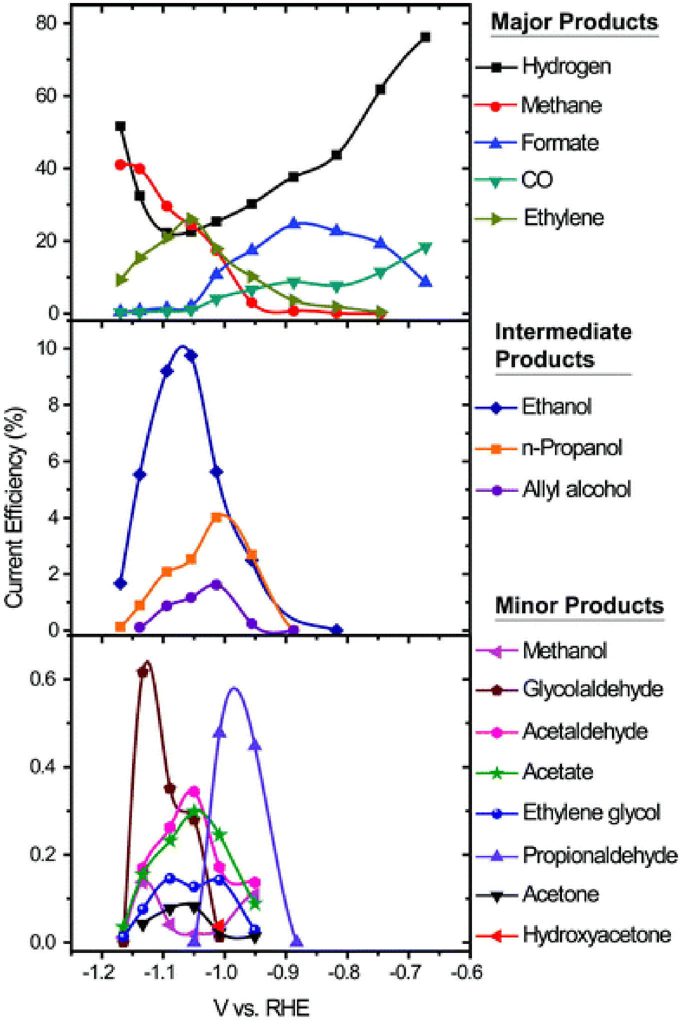

Figure 1.5: Product distribution as a function of potential obtained by Jaramillo and co-workers. (Figure from [15])

Electrolyte dependence

Hori and co-workers have also studied the effect of the electrolyte on the CO_2 electro-reduction.[14] They observed that the ratio between CH_4 and C_2H_4 is highly dependent on the working electrolyte. The formation of C_2H_4 and alcohols was favored in KCl, K_2SO_4, $KClO_4$ and dilute $KHCO_3$. In contrast, CH_4 production was enhanced in high concentration of $KHCO_3$ and phosphate buffer solutions.

This difference in selectivity is attributed to a different local pH. In electrolytes with low buffer capacity such as $KClO_4$ and dilute $KHCO_3$, the pH value in the vicinity of the cathode is expected to be considerably higher than in the bulk due to the consumption of protons during the reduction reaction. Therefore, in these electrolytes the CO_2 electrochemical reduction is occurring at basic pH. On the other hand, in electrolytes with higher buffer capacity, the local pH should be closer to neutral. This difference in pH affects the product selectivity since methane production is proportional to proton activity, while the formation of ethylene is independent of the pH[24]. Consequently, at high pH values, ethylene production is enhanced over methane.

Mechanistic insight

Experimental work on CO electro-reduction has shown a similar potential dependence and hydrocarbon distribution as for the CO_2 electro-reduction[18]. These results suggest that CO is an intermediate of the electro-reduction of CO_2 to hydrocarbons and that the rate limiting step occurs after the formation of CO.

Further experimental insight is challenging since the intermediates cannot be easily probed *in situ*. Theoretical computational modeling is also challenging as it needs to take into consideration the solvent and the electric field of the double layer[25]. Nevertheless, Density Functional Theory (DFT) has been proven to be useful for describing trends in electrocatalysis[26]. Taking into consideration the adsorption energies of the different reaction intermediates it is possible to calculate the overall free energy pathway for the reaction, as a function of potential.

The exact mechanism in which CO_2 is reduced to hydrocarbons is still on debate. Peterson *et al.[23]* proposed a detailed reaction path for the electrochemical reduction of CO_2 to methane on Cu (211). By taking into consideration the reaction free energies of elementary steps they found the lowest-energy pathway shown in Figure 1.6. The last step to become downhill, known as potential determining step, is the protonation of *CO to *CHO.

In a more recent study, Nie *et al.*[27] have taken into consideration kinetic barriers and found that on Cu(111) the protonation of *CO to form *COH is favored over the formation of *CHO. Furthermore, Nie *et al* propose that *COH would be further reduced to methane while *CHO would lead to the formation of methanol.

A full understanding of the CO_2 electrochemical reduction must also contemplate the reaction pathway for the formation of ethylene. This mechanism should account for the different potential and pH dependence observed experimentally for the formation of these two products.

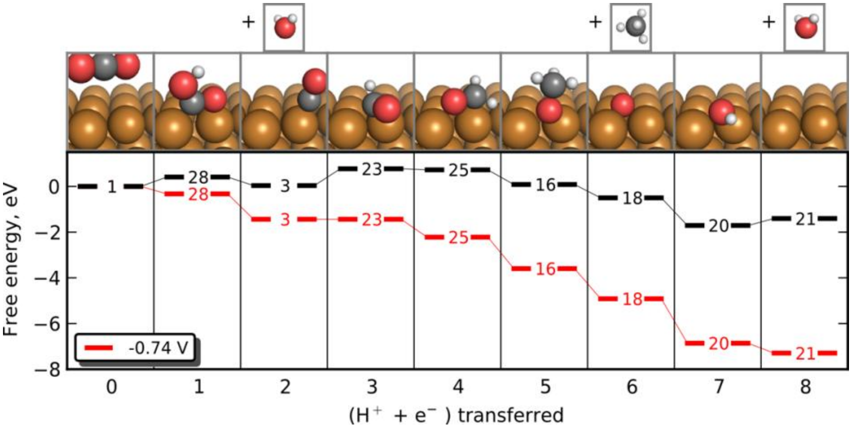

Figure 1.6: Elementary pathway for the CO_2 electro-reduction on Cu(211) including the corresponding the free nergy for each step at 0 V vs. RHE) and at the theoretical overpotential, -0. 74V vs RHE (Figure from [23])

Nørskov and coworkers have suggested that the formation of *CO to *CHO is also the rate limiting step for the formation of ethylene and that C_2 compounds are formed from a non-electrochemical surface reaction between adsorbed species, for example the coupling of *CHO to *OCHCHO*[28]. The fact that a proton transfer is the rate limiting step for the formation of methane and ethylene does not fully explain the difference in selectivity induced by the difference in pH.

Koper and co-workers have suggested that the C-C coupling occurs very early in the reaction, by the formation of a CO dimer[16]. However, Nørskov and coworkers have shown that the *CO dimerization is kinetically unfavorable[28], leaving the door open for more discussion regarding the reaction mechanism for the reduction of CO_2 to hydrocarbons and a better understanding of how the selectivity of this reaction is controlled.

1.3 Electro-catalytic activity of metals

1.3.1 Sabatier principle

A heterogeneous catalyst facilitates a chemical reaction by binding the reagents to the surface. While bound to the surface, the internal bonds of the reactants may be weakened and the formation of new bonds is facilitated.[29] In addition, the probability that the reagents interact with each other is increased by binding them to the catalyst surface. Once the products are formed, they also need to be desorbed from the surface. Therefore, the binding energies of the different intermediates to the surface play a crucial role in the efficiency of the catalyst. A good catalyst has to have a binding energy towards the key intermediates strong enough, so that the reagents will be likely to bind and react, but weak enough so that the products can easily desorb. This concept is known as the Sabatier principle and is well represented by plotting a catalyst's activity versus its binding energy towards the key reaction intermediate. This gives a peak shaped curve known as the Sabatier plot or volcano curve, where the top corresponds to the optimal binding energy.[30-32] Figure 1.7 shows the volcano plot for the HER. The only intermediate for this reaction is *H and therefore is the binding energy between H and the surface determines the activity of the catalyst.

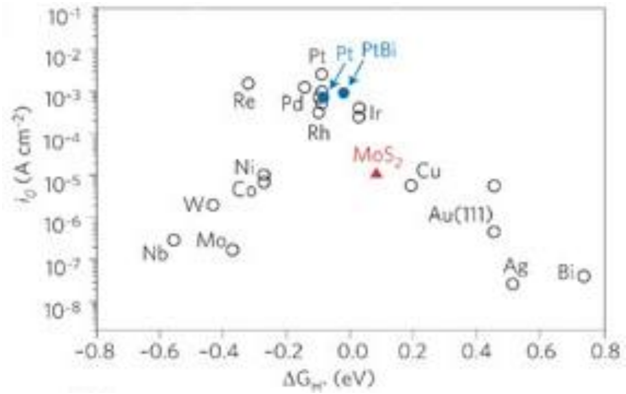

Figure 1.7: Volcano plot for the hydrogen evolution reaction, showing the activity of the material as a function of the *H binding energy.(Figure from[33])

The optimal catalysts are those close to the top of the volcano. The materials on the left side have a strong binding energy towards hydrogen so the products do not desorb easily. While the materials on the right side bind hydrogen weakly so the proton cannot be adsorbed on the surface to be reduced into hydrogen.

This clearly illustrates the difference between the reactivity and activity of a catalyst. The binding energy is a measure of the reactivity since it tells us how much the catalyst interacts with the reactants. Whereas activity is the measured rate of the catalytic reaction and depends on the catalyst reactivity.[34]

1.3.2 Reactivity of the metals

To understand the parameters, which control the reactivity of a metal it is necessary to know how the surface interacts with the adsorbates. When a molecule approaches the metal surface, first there is an attractive interaction due to Van der Waals forces. When the molecule moves closer to the surface, it can be chemisorbed causing rearrangement of the electronic configuration as illustrated in Figure 1.8[35].

The interaction between the valence level of the adsorbate and the sp-band of a metal causes a broadening and a downshift in energy of the adsorbent's valence level, which contributes to the binding between the adsorbate and the surface. In the case of transition metals the interaction with the d-band causes splitting of the adsorbates valance level in bonding and anti-bonding.

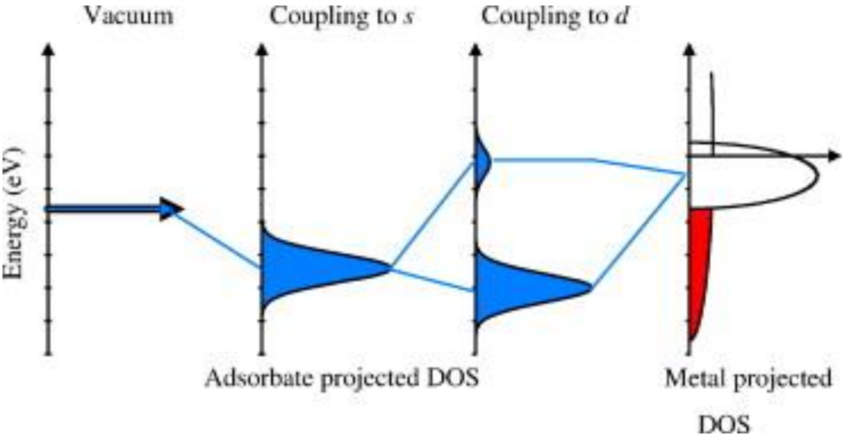

Figure 1.7: Schematic illustration of the bond formation between and adsorbate and a transition metal.(Figure from [35])

The resulting adsorbate levels below the Fermi level will be occupied and contribute the binding between the metal surface and the adsorbate. Based on this interaction, the d-band model proposes that the adsorption energy between an adsorbate and a transition metal is given by the coupling of the adsorbate valance states to the metal d-band.[36] The strength of this interaction can be related to the center of the d-band that can be varied by changes on the surface structure and by alloying.

Structural effect: The surface structure of a metal affects its electronic properties and thus its reactivity. For instance, the overlap between the electronic orbitals depends on the coordination number of the surface atoms. The electronic orbitals overlap is smaller in surfaces with low coordination numbers, like in steps and kinks than in close pack surfaces. A smaller overlap is reflected in a narrower d-band. The filling of the d-band and thus the Fermi level, however, should remain constant. Therefore the d-band is shifted upwards as illustrated in Figure 1.9.

Having a higher d-band center causes a stronger interaction between the metallic surface and the adsorbates. For this reason, steps and kinks tend to be more reactive than the close packed surfaces. The electronic orbitals' overlap is also affected by the interatomic distance, also known as *strain effect[37]*. Having an expanded surface also causes the d-band width to decrease and consequently an upwards shift of the d-band center. On the contrary having a contracted surface will make the d-band broader and its center will move downwards in energy.

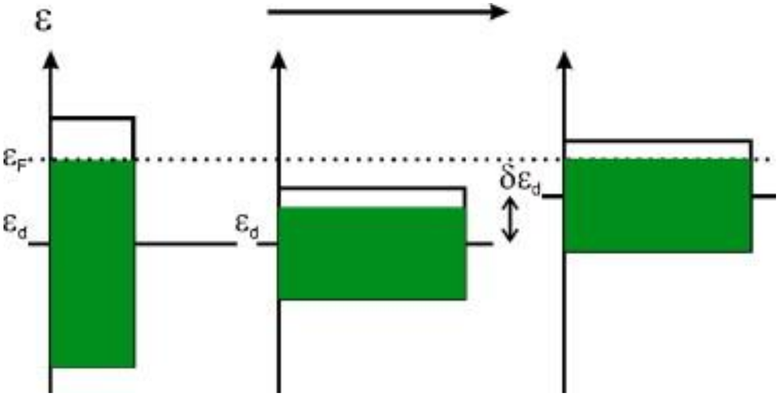

Figure 1.9: Schematic representation of how the d-band width affects the d-band center for a metal with a fixed number of d electrons. (Figure from [35])

Alloying effect: The reactivity of a metal can also be modified by alloying it. This change in reactivity can be attributed to a combination the *strain effect* and the *ligand effect.* As explained previously, the strain effect is due to a change in the electronic orbitals overlap leading to a narrower or broader d-band. As a result of this change in width the d-band is shifted.

The ligand effect corresponds to a change in the electronic structure of given metal by adding a solute metal. Depending on the nature of the solute atom the host metal can be made more or less reactive.

For most alloys it is difficult to distinguish between ligand and strain effect since the host atom will induce both a change in the lattice parameter and in the electronic structure. The same holds for overlayer structures, where a monolayer of one metal is deposited on top of another metal[38]. In these structures, the overlayer usually adopts the lattice constant of the substrate, resulting in a tensile or compressive strain on the surface. At the same time the substrate metal affects the electronic structure of the overlayer contributing to the ligand effect.

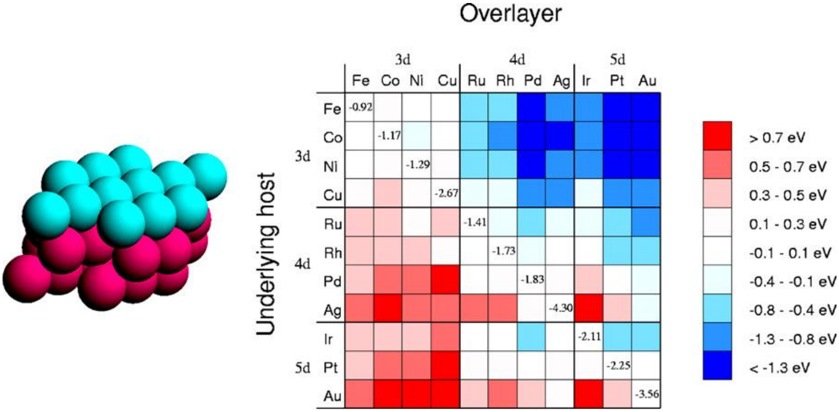

Figure 1.10: d-band changes for metal overlayers onto transition metal substrates. (Figure from [35])

DFT calculations have been used to predict the changes in the d-band center for metal overlayers on transition metal substrates. As it can be seen in Figure 1.10 the d-band center can be varied substantially by forming ovelayers. For example the d-band center of copper is shifted more than 0.7eV upwards by depositing it on Pt. This presents an interesting possibility for controlling the reactivity of metals by depositing it onto a different metal.

Many catalytic studies have been taken advantage of this possibility by using overlayer structures[39-41] and core-shell nanoparticles[42-46] as catalyst. The structure of this system, however, may not be always as simple as expected.[47-49] For example, Friebel and *et al*. used X-ray adsorption spectroscopy to demonstrate that Pt overlayer on Rh actually formed 3D islands, which agrees with observed activity towards the oxygen reduction reaction (ORR)[50]. Furthermore, under reaction conditions, the structure of bimetallic system may be modified, due to its interaction with adsorbates.[51-53] This surface rearrangements are reflected on the catalyst reactivity. Therefore, it is crucial to have insight into the catalyst surface structure under reaction conditions to have a good understanding of its catalytic activity.

1.4 Thesis outline

The main focus of this Thesis has been to study the effect of the surface structure of copper on the electrochemical reduction of CO_2. With this purpose we have studied polycrystalline copper surfaces with different roughness and Cu overlayers on Pt single crystals.

The electrochemical methods and surface science techniques used to study these surfaces are described in chapter 2. This chapter also covers the chromatographic techniques used for the quantification of the CO_2 reduction products.

The third chapter focuses on the study of three different polycrystalline copper surfaces. These surfaces were characterized by X-ray photoelectron spectroscopy and scanning electron microscopy before being tested as electrocatalyst. The catalytic studies showed a clear effect of the surface morphology on the activity and selectivity of copper. These results are analyzed considering the local pH effects as well as DFT mechanism insights.

The fourth chapter describes the formation of Cu overlayers on Pt single crystals. These structures were also tested as catalyst for CO_2 electro-reduction. In addition, electrochemical scanning tunneling microscopy (EC-STM) was used to characterize the surface in the presence of CO, which is well-known reaction intermediate. The EC-STM results are crucial in the understanding of the catalytic activity of Cu on Pt single crystals.

Finally, chapter 5 discusses de formation of Cu/Pt (111) surface alloy and near surface alloy. On these systems the location of the copper atoms affects the reactivity of Pt. This knowledge can be used to tailor the reactivity of Pt as demonstrated in this work for the electrochemical oxidation of CO.

Chapter 2

2. Experimental methods

2.1 Electrochemical set up

2.1.1 Electrochemical for polycrystalline copper

The measurements on the polycrystalline copper electrode were carried out in a costume made H cell, in which the working compartment was separated of the counter electrode compartment by a Nafion membrane (Figure 2.1).

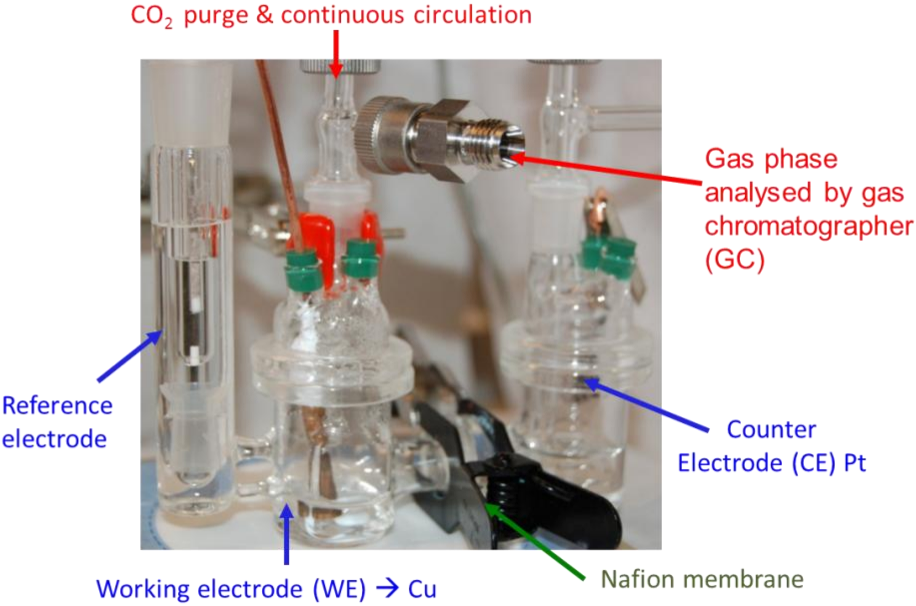

Figure 2.1: Photograph of the H cell used for polycrystalline copper studies.

A copper foil (25 mm x 12.5 mm, 1 mm thickness, 99.999%, Goodfellow) was used as a working electrode, a platinum wire as a counter electrode and Hg/$HgSO_4$ was used as a reference electrode. The working electrode compartment had an inlet used to purge it with N_2 or CO_2. The outlet was coupled to a gas chromatographer to analyze the gaseous products. During reaction conditions, the cell was turn into recirculation mode in such a way that the outlet gas was pumped back to the inlet.

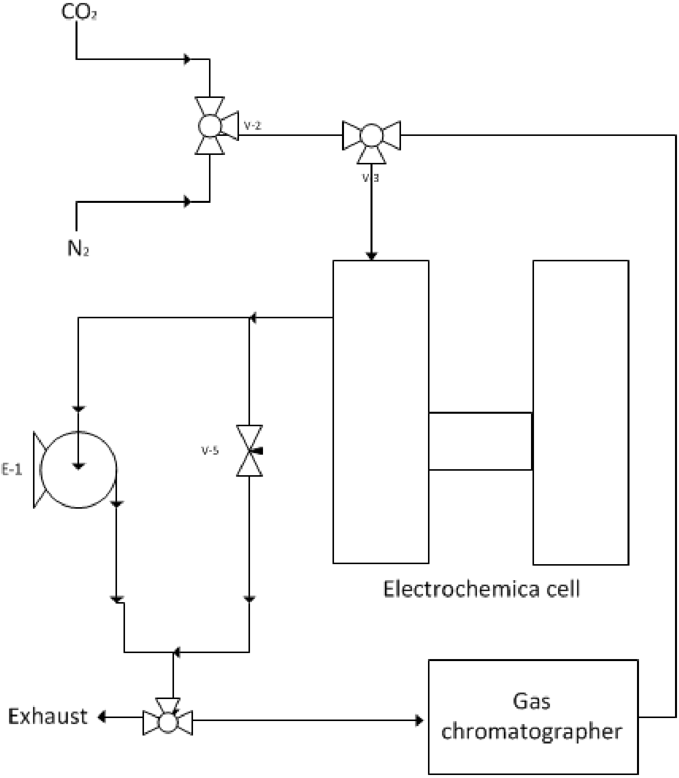

Figure 2.2: Process flow of the setup for polycrisalline studies

2.1.2 Electrochemical cell for single crystal studies

The single crystal studies were carried out in a costume made three-electrode electrochemical cell [54] (Figure 2.3).

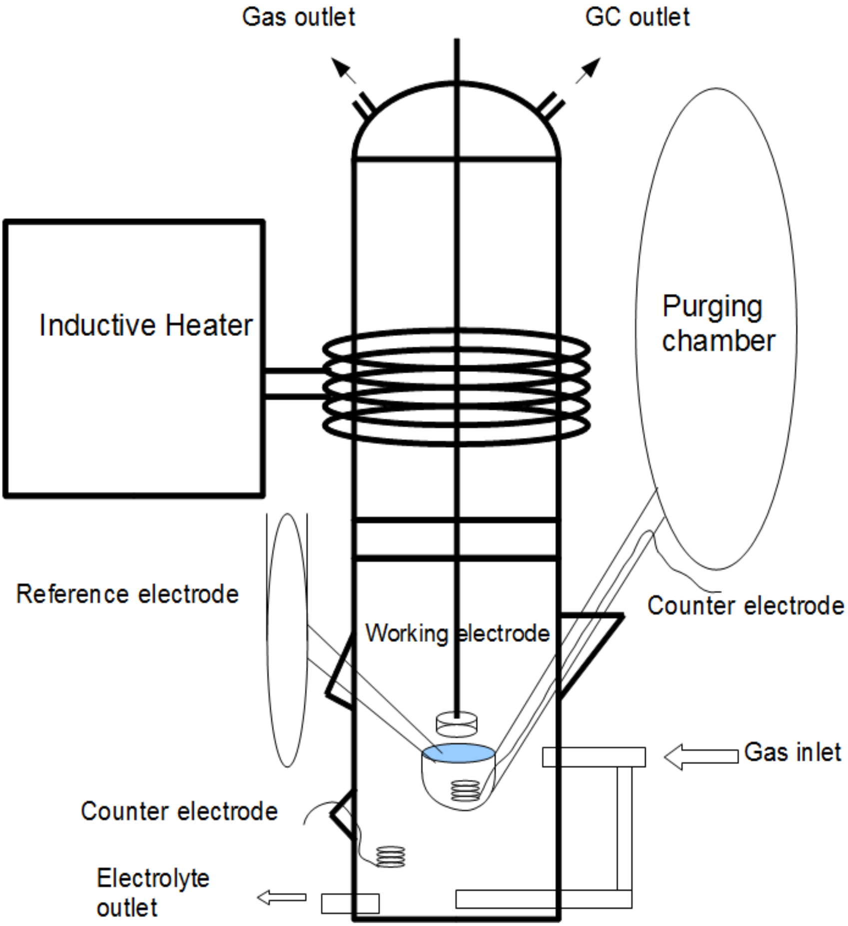

Figure 2.3: Scheme of the electrochemical cell for single crystal studies (Figure by Brian Knudsen)

In this cell, the single crystal hangs from a Pt wire attached to a glass tube that can be moved up and down to have the crystal at the desired height of the cell. The upper part of the cell, made of quartz, is coupled to an induction heater (SP15A from MTI corporation USA) that allows the annealing of the sample. This process is a thermal treatment used to obtain clean well-ordered Pt surfaces.[55] The crystal temperature during the annealing is controlled by a thermocouple in contract with the top part of the crystal.

After the annealing the crystal can be moved, without exposing it to air to the bottom of the cell, made of glass, where the electrochemical measurements take place. The working electrode is approached to the electrolyte to form a hanging meniscus, so that only the desired crystal face touches the solution. The small spoon inside the cell is used for measurements that only required small volumes, i.e. cyclic voltammograms and copper under potential deposition (UPD). The reference electrode ($Hg/HgSO_4$) is in contact with the electrolyte through a mobile capillary while the counter electrode is a platinum wire in the bottom of the spoon. For running electrochemical CO_2 reduction, the spoon is moved to a side allowing to work with a bigger volume and Pt wire in the side of the cell functions as a counter electrode. The Ohmic resistance becomes significant during the bulk electrolysis experiments. It is affected by the distance between capillary for the reference electrode and the single crystal that is different from one experiment to the other. Therefore the Ohmic resistance was measured for all bulk electrolysis experiments and used to correct the working potential value.

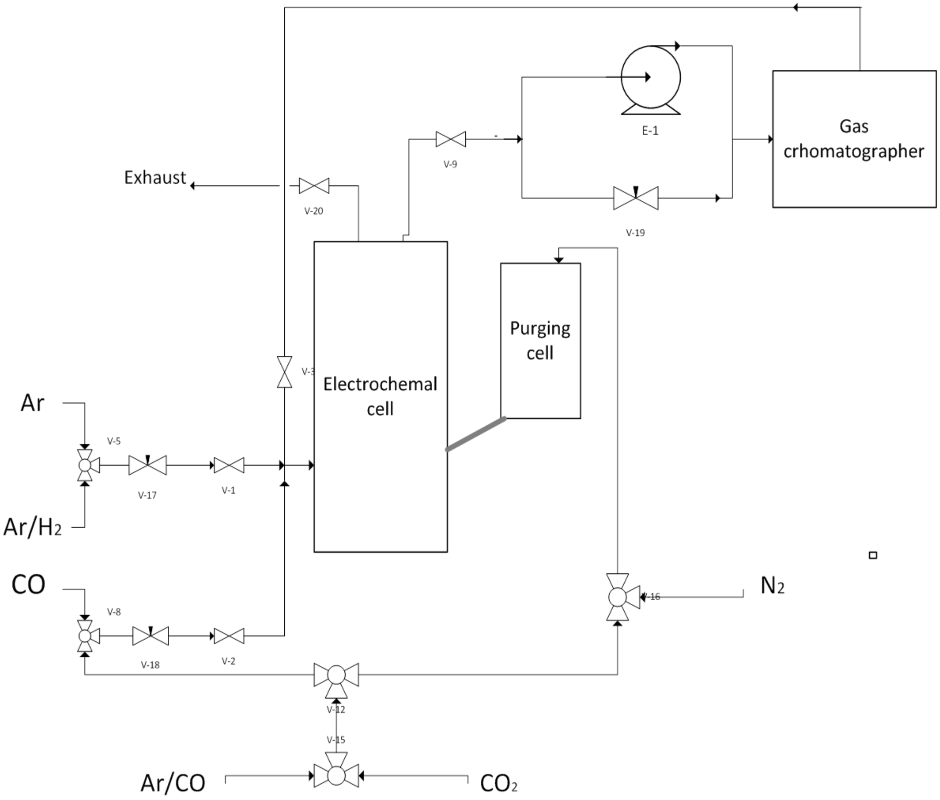

Figure 2.4: Process flow of the setup for single crystal studies.

Next to the main compartment, there is a purging chamber where the working electrolyte can be purged with N_2 or CO_2. When the valve connecting this chamber to the main one is opened, the electrolyte goes through the spoon into the main cell. This allows exchanging the electrolyte while having the working electrode under potential control.

The cell can be purged with different gases (Ar, CO_2, CO, 5%H_2 in Ar and 0.1% CO in Ar) through two different inlets. The bottom inlet allows purging the electrolyte when the cell is used in the full volume mode, while the gas passing through upper inlet goes only to the gaseous phase. At the top of the cell there are two outlets, one going to waster seal and a second one that allows the reaction gas go into intro recirculation or to the gas chromatographer for product analysis (Figure 2.4).

2.2 Electrochemical techniques

Before the experiments, the cell was cleaned for 24 hours in a “piranha” solution consisting of a mixture of 96% H_2SO_4 and 30% H_2O_2 (3:1) in order to remove any metal or organic impurities. Afterwards the cell was rinsed multiple times with ultrapure water (Millipore Synergy Pak UV >18.2 M Ω cm, 22±2°C) and sonicated at 50°C to remove sulfates. This procedure was also used for cleaning all the glass containing the electrolyte.

The electrochemical measurements performed in the polycrystalline cell were controlled by Biologic VMP2 potentiostat, while for the single crystal measurements we used a Biologic Instruments SP-150 potentiostat, both of which were controlled via the EC-Lab. All measurements were carried out using Hg/(HgSO4) as a reference electrode but they were converted to reversible hydrogen electrode (RHE) for a better comparison.

2.2.1 Cyclic voltammetry

Cyclic voltammetry was used in order to characterize the studied surfaces. This is a widely used electrochemical technique that consists of sweeping the potential back and forward at a fixed scan rate (dE/dt) while recording the current response (Figure 2.5). The obtained curve is known as cyclic voltammogram (CV), and its shape depends on the processes occurring at the electrode surfaces.

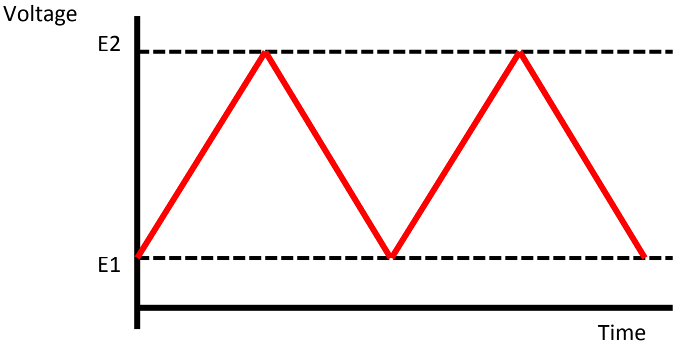

Figure 2.5: Potential as a function of time in cyclic voltammetry

During the anodic sweep (that is, going to positive potentials) oxidation reactions give a positive current, while in the cathodic sweep (going to negative potentials) the reductions processes are observed as a negative current. These processes are surface sensitive, thus the shape of the CV is given by the structure and the chemical nature of the electrode surface and of the composition of the electrolyte. For these reason, CVs are consider as a fingerprint of a surface. In particular, when working with single crystals, cyclic voltammetry is used to determine the quality and cleanliness of the surface (Figure 2.6).

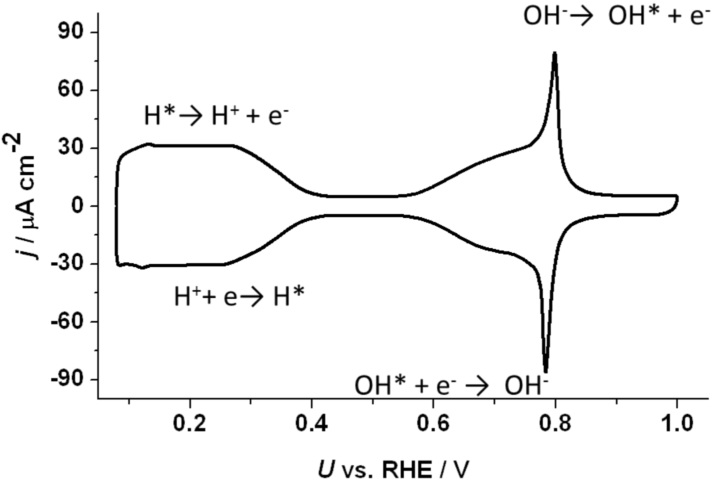

Figure 2.6: Typical voltammogram for Pt(111) in $HClO_4$

Cyclic voltammetry can provide thermodynamic and kinetic information of the processes occurring at the electrode-electrolyte interface, and thus can also be used to study electrochemical reactions, as it is shown in chapter 5 for the CO oxidation. After adsorbing CO onto the surface one can sweep the potential toward positive values, and observe a positive current due to the oxidation of CO (Figure 2.7). The less positive the oxidation peak occurs, the lower the barrier for the reaction is, meaning that the surface at which CO is adsorbed is a better catalyst for the electrochemical oxidation of CO.

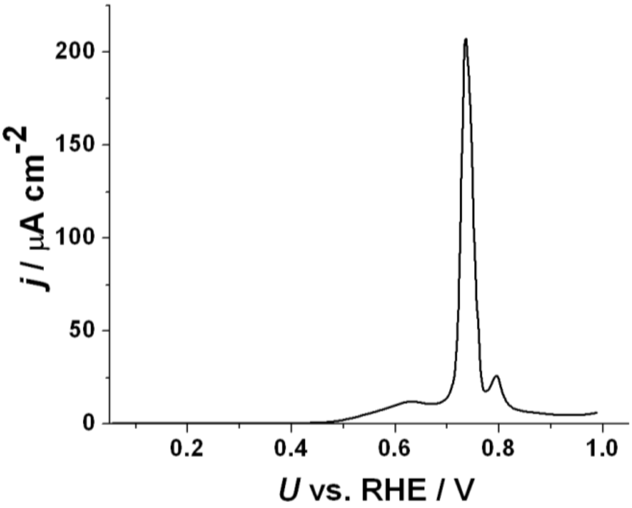

Figure 2.7: Electro-oxidation of adsorbed CO (also known as CO stripping) on a Pt electrode

2.2.2 Chronoamperometry

Chronoamperometry is a technique that consists of keeping the potential fixed and measuring the current as a function of time. This allows the adsorption of some species, such us Cu or CO, onto the surface (which in this work will be a Pt electrode). This technique is also used for driving electrochemical reactions such as bulk electrolysis. For this work the electro-reduction of CO_2 has been studied by chronoamperometry. The total charge measured during the reaction corresponds to the electrons used in the reduction reactions and thus it is proportional to the amount of products formed. The difference between the applied potential and the reaction equilibrium potential is known as **overpotential** and it is a measure of how much extra energy one needs to supply to drive the reaction.

2.3 Product analysis

2.3.1 Gas Chromatography

After CO_2 electro-reduction, the gas phase was analyzed by gas chromatography. This analytical technique allows to separate and to identify the different components of the gaseous mixture.[56] For the analysis, a small volume of the sample is mixed with a carrier gas, usually an inert gas such as helium or argon, known as mobile phase. This mobile phase passes through a column known as stationary phase. The components of the sample interact with the walls of the column and depending on how strong each compound interacts with the column it will take it longer or shorter time to elute through the column. A strong interaction between the column and a given product results on a long retention time, whereas a weak interaction implies a short retention time. The retention can be modified by changing the column temperature or the flux of the carrier gas. When the optimal conditions are used, the different compounds will have different retention times allowing its adequate separation. At the end of the column, the products are analyzed with the appropriate detector, giving a signal when one of the components of the sample leaves the column. (Figure 2.6). For this research the following types of detectors where used:

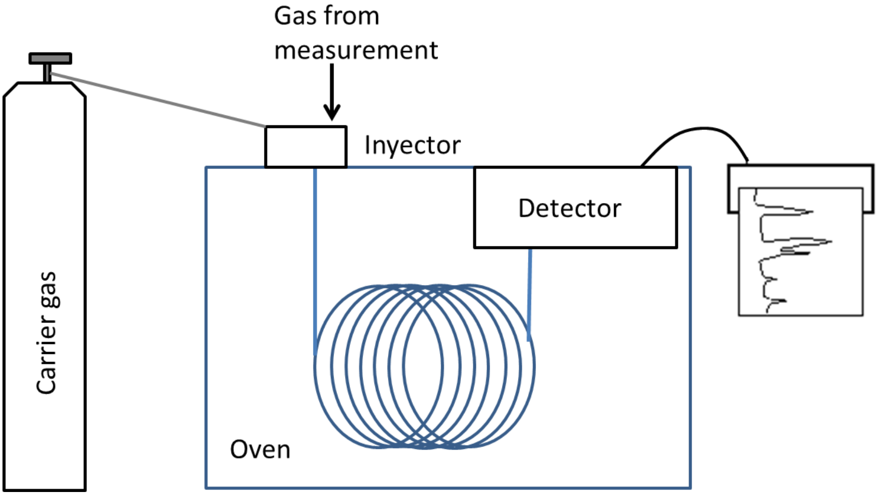

Figure 2.8: Schematic representation of a Gas chromatographer

Thermal Conductivity Detector (TCD): This detection method is used to detect both organic and inorganic compounds. It is based on the change of thermal conductivity of the carrier gas when another compound is present. For this work this detector type is used for the quantification of H_2, CO and for detecting N_2 in case of air leaking in.

Flame Ionization Detector (FID) This detection method is used commonly to detect organic compounds, since it works by passing the sample through a hydrogen flame and measuring the ions produced when burning the components of the sample. For this work this detector type is used for the quantification of CH_4, C_2H_4, C_2H_6 since higher hydrocarbons were not detected.

The area of the signal depends on the product being analyzed and is proportional to its concentration in the gas phase. Therefore the GC was calibrated with a mixture of %5 H_2 in Ar from AGA and with a sample gas containing 0.2% CH_4, 0.25% C_2H_4,0.15% C_2H_6, 0.15% C_3H_8 0.1% C_3H_6 and 1% CO in Ar from AGA. The calibration was done by passing the sample gasses through the working cell into the chromatographer at the same flux used during the reaction. First the appropriate temperature and flow were determined and then, the obtained area for a given concentration was used to establish the relationship between the area and the concentration of each product.

$$Area = \alpha \;\; Product$$

Equipment details: The gas chromatographer (Agilent 6890), was equipped with a thermal conductivity detector (TCD) through HP-Molecular Sieve 5A and flame ionization detector (FID) through HP-PLOT. The gas chromatographer was operated at 40C using argon as a carrier gas.

2.3.1 High performance liquid chromatography (HPLC)

This chromatographic technique has been used to determinate the products present in the liquid phase. As gas chromatography, HPLC allows to separate the compounds of a mixture based on their different interaction with a mobile and a stationary phase only that the mobile phase is liquid.

For the analysis, a small volume of the sample is mixed with a solvent that is forced to pass through the column applying a high pressure. The components of the mixture move through the column with different rates that can be varied by modifying the flow, the temperature and the composition of the mobile phase. When the polarity of the mobile phase is increased, the polar compound of the sample interacts stronger with it and elutes faster. At the end of the column there is a detector that allows to identify the product based on their retention time. The detector has to be adequate so that all the components of the sample give a signal when going out the column (Figure 2.7).

Diode Array Detector (DAD): It allows detecting products based on their absorption of UV/ visible light. A DAD detector has the peculiarity of having multiple photodiodes arrays to obtain information from a wide range of wave lengths.

Reflective Index Detector (RID): It is based on the difference of refraction index between the mobile phase and the sample. It works by shining a beam of light through a dual compartment flow cell. One compartment contains the mobile phase a reference and through the second one passes the column eluent. When something different that the mobile phase goes into the second compartment the refractive index will be different of cero giving a signal. (Figure 2.7)

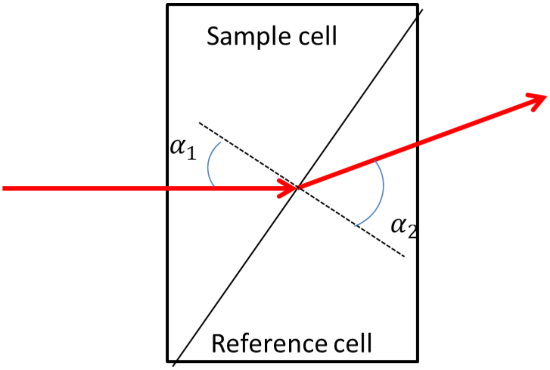

Figure 2.9 Sachem showing the principle for the reflective index detector (Figure adapted from[57])

As in gas chromatography, in liquid chromatography, the peak area is proportional to the concentration of each product. For calibration the HPLC we used solutions of known concentrations with the possible products, formic acid, acetic acid, acetaldehyde, methanol and ethanol in water and in $KHCO_3$.

Equipment details: The HPLC used for these studies is an Agilent 1200 series equipped with an autosampler, degasser, quaternary pump, reflective index detector and a diode array detector. The column is an Aminex HPX-87H (Bio-Rad). The HPLC has been run at room temperature using 0.005M H_2SO_4 at a flow rate of 0.6mL/min.

2.3.3 Efficiency and selectivity quantification

Gas chromatography and HPLC provide information concerning the concentration of different compounds, which is used to calculate the amount of products formed during the reaction. This information is insufficient to compare the performance of different electrocatalysts since the amount of products also depends on the catalyst area and the current passing through it. Therefore in this work the catalytic results are given as faradaic efficiencies and partial current densities.

Faradaic efficiency: It is a measure of how selective an electrocatalyst is towards a particular product and it is given by the percentage of the total charge that is used in the formation of each product. A high faradaic efficiency towards a given product (close to a 100%) indicates that the electrocatalyst has a highly selective, yet does not provide information on its activity.

It is important to mention that the faradaic efficiency depends not only on the amount of product formed, but also on the amount of electrons needed to reduce CO_2 into that particular product. Therefore, if the same amount of CO and methane is formed the faradaic efficiency towards methane would be 4 times larger, since there are 8 electrons involved in the formation of methane and only 2 in the formation of CO.

Partial current densities density: Indicates the current used in the formation of a product per unit of area of the catalyst. Contrary to the faradaic efficiency, the partial current density gives information on how active a catalyst is towards a given product but not on its selectivity.

2.4 Surface characterization

This section describes the techniques that were used to characterize the electrode surfaces, since the results will be discussed in later chapters. However, I would like to state that these measurements were done by other people working at CINF.

2.4.1 X-ray photoelectron spectroscopy (XPS)

XPS is a surface characterization technique that relies on the photoelectric effect, illustrated in Figure 2.10. It consists of irradiating the sample with photons of sufficient energy to be absorbed by an electron bellow the vacuum level[58, 59]. This electron is then able to escape the surface with a given kinetic energy (E_{kin}) that depends on the energy of the incident photon ($h\nu$) and the biding energy of the electron (E_{bin}).

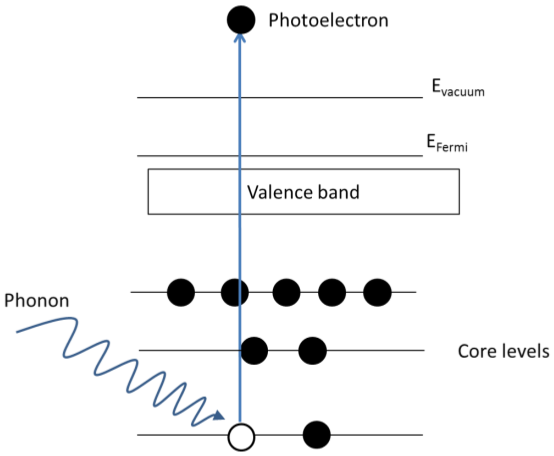

Figure 2.10: Schematic representation of the photoelectric effect

When working with a known energy for the incident photon, the kinetic energy of the photoelectrons can be measured and related to their binding energy according to the following equation:

$$E_{kin} = h\upsilon - E_{bin} - \phi_{analyzer}$$

$$\phi_{analyzer} = work\ fuction\ of the\ analizer$$

The X-rays used for XPS measurements can penetrate several nanometers into the sample. However, the main free pad of the emitted electrons in the energy range of 5-1500eV have a mean free path between 0.5 to 2 nm. This means that XPS is a surface sensitive technique since only the electrons emitted near the surface region can be detected.

From the XPS measurements one obtains a density of electrons as a function of its binding energy, which is characteristic of each element and therefore can be used to determine the surface composition of the sample. Furthermore, since the binding energies of the core electrons are affected by the chemical environment of the atom, XPS also provides information about the chemical state of the elements present in the sample.

Angle resolved XPS

Using this technique is possible to obtain a concentration depth profile of a sample.[60] When the emitted electrons are detected at an angle other than 0 with respect to the surface, the depth from which the electrons can be detected is decreased as a factor of cosθ (figure 2.11)

Based on this principle is possible to vary the angle between the sample and the normal of the sample to change the surface sensitivity of the XPS measurements. The data obtained from a set of different angles can be converted into a sample depth profile.

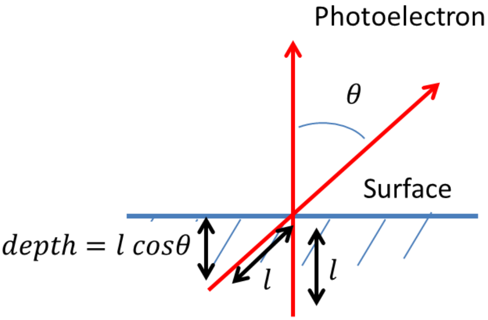

Figure 2.11: Scheme showing the relation between the detection angle and depth. (Adapted from[61])

Equipment details: The XPS system (Sigma Probe, Thermo Scientific) used a monochromated Al Kα source for incident radiation and a six-channel detector for measurement of photoelectrons.

2.4.1 Scanning Electron Microscopy (SEM)

Scanning Electron Microscopy is a technique that takes advantage of the shorter wavelength of the electrons in comparison to the visible light, used in optical microscopy, to get images with a higher resolution.

It consists on directing a beam of high energy electrons, also known as primary electrons, towards a sample in an ordered pattern. When the primary electrons interact with the sample secondary electrons are emitted together with back scattered electrons and X-rays (Figure 2.12). The secondary electrons come from the region near the surface and contain topographic information, so these electrons are detected to generate an image of the sample.

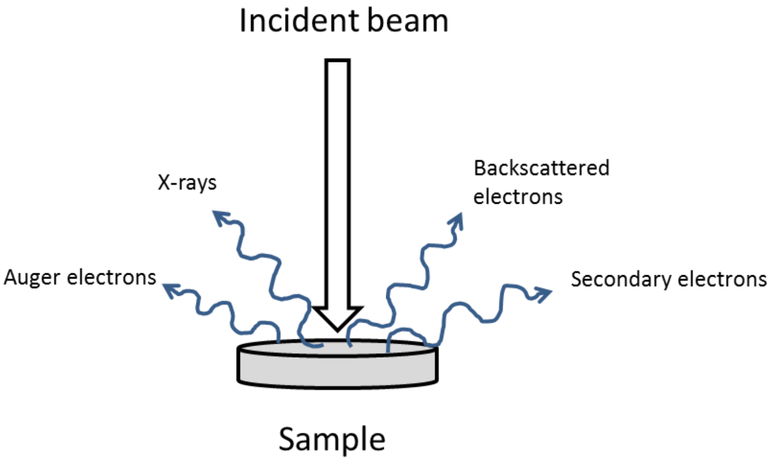

Figure 2.12: Schematic representation of the interaction between the electron beam and the sample

Equipment details: The images presented on this thesis are obtained with and SEM, FEGSEM 200F digital scanning microscope.

2.4.3 Scanning Tunneling Microscopy (STM)

It is a microscopy technique based on the concept of quantum tunneling that allows imaging a sample with atomic resolution. The analysis is conducted by bringing a conducting tip very close to the surfaces to be studied and applying a voltage difference between the tip and the sample (U_t, potential bias).[62] The applied voltage allows electrons to tunnel through the vacuum between the tip and the surface generating a tunneling current (*it*, typically of a few nanoampers). This tunneling current decays exponentially with the distance between tip and sample and it is proportional to the potential bias and the local density of states at the Fermi level.

The STM may be used in two scanning modes: *Constant current mode*, in which the separation between the tip and the substrate is readjusted when the tunneling current deviates from a predetermined value (Figure 2.13), or *constant height mode* in which the tunneling current is monitored while the tip is scanned at a fixed distance from studied surfaces.

Electrochemical STM (EC-STM)

An *in situ* electrochemical STM allows imaging the surface through a layer of electrolyte while controlling the potential at the studied surface. An EC-STM can be therefore used to study the surface structure while cycling the potential.

Equipment details The EC-STM measurements were carried out in custom made set up which combines a standard electrochemical cell with a Besocke-type scanning tunneling microscope. For the electrochemical two Pt wires act as counter and pseudoreference electrodes.

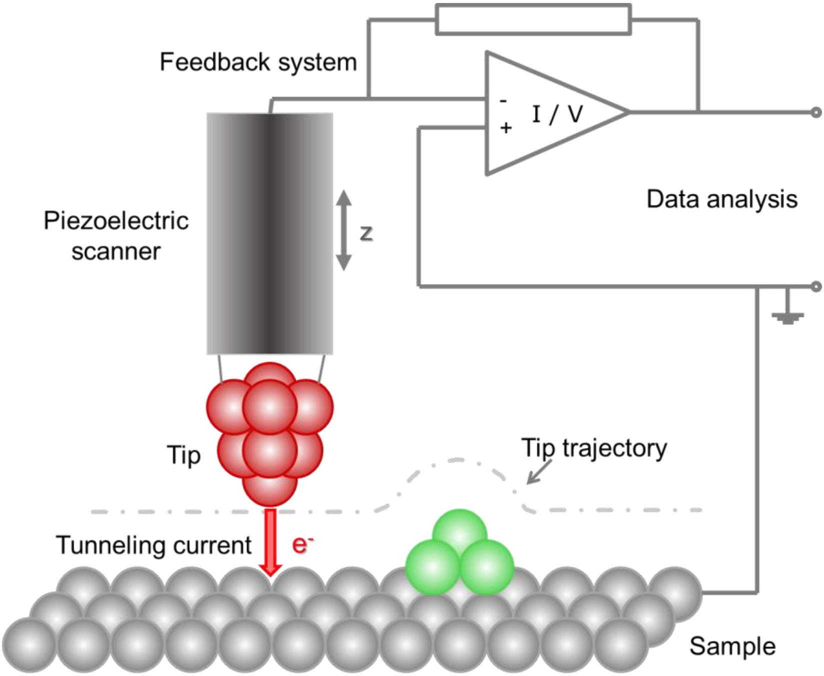

Figure 2.13: Scheme of the STM operation in constant height mode. (Figure from[63])

2.5 Testing the single crystal set up for CO_2 reduction

The cell for single crystal studies has many features that make it an excellent set up for working with single crystals. However, some of its characteristics may not be the first option when it comes to studying CO_2 reduction. For instance, having a hanging meniscus does not allow a strong agitation which may lead to mass transport limitations. In addition, having the working and the counter electrode in the same compartment may lead to the re-oxidation of the reduction products at the anode leading to an error in product quantification.

For this reason one important part of this work has been focused on ensuring that this cell is adequate for studying CO_2 electro-reduction. With this purpose we have studied polycrystalline copper (10 mm x 10.mm, thickness 1mm, 99.999%, Goodfellow) as electrocatalyst for CO_2 reduction as a reference. The foil was cleaned by electropolishing in H_3PO_4 applying a potential of 2V between the Cu foil and a Pt wire.[24]

Figure 2.14 shows the results after 15 minutes of reaction in 0.1 M $KHCO_3$ (pH 6.8) solution prepared by bubbling CO_2 into 0.1M KOH (Merck, Suprapur) until the pH was stable.

This figure shows our results for the faradaic efficiencies as a function of potential together with the results from Hori’s[14] and Jaramillo’s[15] groups.

It is possible to see that despite some discrepancies there is a similar trend. Ethylene and methane start forming at around -0.7 V. Close to this value ethylene production is favored over methane, while as we get closer to -1.0V methane formation is dominant. We also observed that closed to -0.7 V the production of hydrogen starts decaying from around 80% to close 50%. In our working set up CO was only detected at -0.95 and -1.0V vs RHE due to the low sensitivity of our GC towards CO. Volumetric CO concentration lower than 0.1% are bellow GC detection limit, so CO can only be detected when the partial current are sufficiently high.

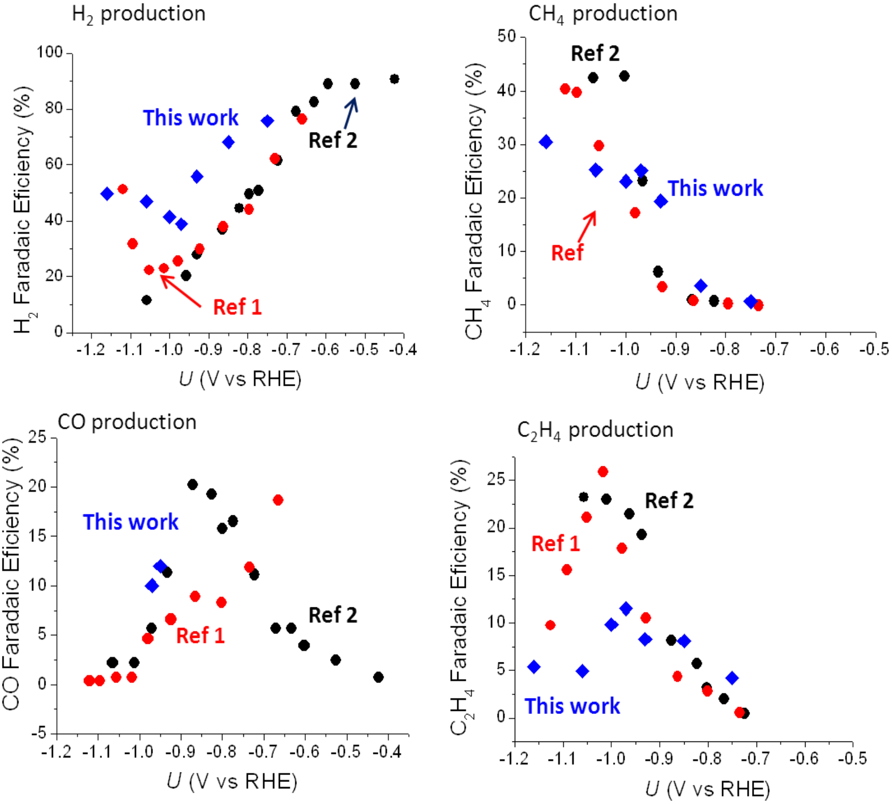

Figure 2.14: Faradaic efficiencies of the CO_2 reduction on polycrystalline copper compared with literature results[14, 15]

The discrepancies between the results in our setup and the values in literature are bigger at higher over potentials at which high current densities are expected. In such conditions the difference of mass transport and local pH caused by a different diffusion layer thickness will become more important and may account for some of the observed discrepancies.

Since we are aware that different diffusion layer thickness may influence the catalytic results, we determinate it for the single crystal setup when the catalyst is a foil completely immersed in an electrolyte (like the copper bench mark) and for a single crystal in a hanging meniscus configuration. The diffusion limiting current for the oxygen reduction reaction (ORR) on a Pt foil and on a Pt(211) is used to estimate the diffusion liming current. This value can be used to estimate the thickness of the diffusion layer assuming Fick difusion for O_2 (Figure 2.15).

Using this simple model we determinate that when working with a foil the thickness of the diffusion layer when working with the foil is 0.0062cm and 0.0070cm when working with the single crystals. These results are in the same order of magnitude leading us to believe that the catalytic results obtained on the single crystals can be fairly compared to our Cu benchmark.

$$i_{limit} = r4F \qquad\qquad r = \frac{D_{O_2}C_B}{\delta}$$

Where:

$r = reaction\ rate$

$C_B = Bulk\ O_2\ concentration$

$D_{O_2} = O_2 difussion\ cofficient$

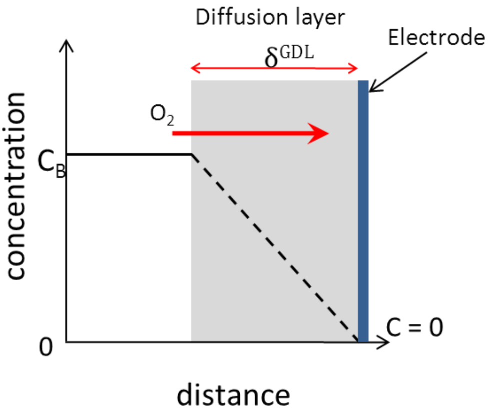

Figure 2.15: Scheme of the difussion layer. Showing the concentration of O_2 as a function of distance to the electrode.

Chapter 3

3. Surface morphology effect on the selectivity of polycrystalline copper

The effect of the surface morphology of copper on its catalytic activity towards CO_2 was studied by comparing three different copper surfaces. The morphology of the samples was studied with scanning electron microscopy (SEM) while the composition was determined by X-ray photoelectron spectroscopy (XPS). Cyclic voltammetry was used as an initial evaluation of the electrolytic activity of the samples. In addition bulk electrolysis was performed to determinate the selectivity of the surfaces. These catalytic studies showed a strong effect of the copper surface morphology on the activity and selectivity of the catalyst. The rough surfaces exhibit a higher selectivity towards CO_2 reduction over hydrogen evolution, in particular towards ethylene production. These results are discussed based on the effect of local pH and considering the mechanism insight from density functional theory.[64]

3.1 Sample preparation

The studied surfaces were prepared from a copper foil (25 mm x 12.5 mm, thickness 1mm, 99.999%, Goodfellow) and pretreated following a different procedure to obtain three surfaces with different roughness.

Electropolished copper: Prepared by electropolishing, applying a potential of +2 V between the copper electrode and a platinum cathode in phosphoric acid (1 mol/L) for 20 minutes, followed by rinsing the copper electrode with deionized water (18 MΩ). During the electropolishing procedure the surface impurities and part of the copper itself are oxidized and dissolved into the electrolyte. The protruding parts of the surfaces will dissolve easily resulting in a smooth clean surface, as has been seen in scanning tunneling microscopy (STM) studies [65-67]

Nanoparticles-covered copper: This sample was prepared *in situ* in two steps. First, an electropolished copper electrode was cycled between -0.6 and +1.15 V vs. RHE at 20 mV/s in N_2 saturated $KClO_4$ (0.1 M, Aldrich, 99.99%). Since the cyclic voltammetry was performed on a non-buffered solution, the pH of the electrolyte was shifted from 7 to 10.5 due to proton consumption during hydrogen evolution reaction at potentials below 0 V vs. RHE. Figure 3.1, shows the cyclic voltammogram obtained at pH 10.5. This CV shows a wide oxidation peak starting at +0.55 V vs. RHE that we attribute to Cu oxidation. The increase in current density at more positive potentials could be assigned to both copper dissolution and porous bulk oxide formation. On the cathodic scan, the first reduction peak, at +0.7 V vs. RHE, most likely corresponds to the reduction of CuO to Cu_2O in agreement with the thermodynamic potential predicted by the Pourbaix diagram (Figure 3.2). The second peak at +0.35 V vs. RHE is attributed to the reduction of Cu_2O to metallic Cu. The third reduction peak, centered around +0.05 V vs. RHE, could be assigned to removal of adsorbed hydroxide species before hydrogen evolution occurs. Desorption of OH^- species involves an electron transfer as well as an increase in the local pH, which then shifts potentials on the RHE scale towards more negative values and causes the peak to look broad. Finally, hydrogen evolution appears as an exponential increase of the cathodic current, which also causes a pH shift towards higher values.

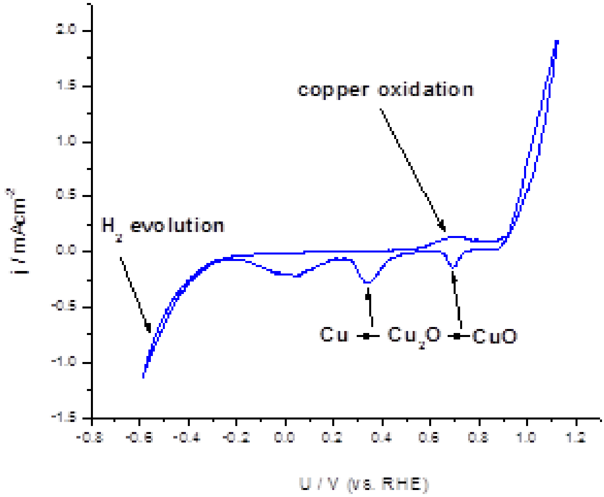

Figure: 3.1: Cyclic voltammogram for the oxidation of a Cu foil in 0.1 M $KClO_4$ purged with N_2 at pH 10.5 (First step in the formation of Cu nanoparticles). The current density is normalized by the geometric area of the electrode surface.

According to the Pourbaix diagram of copper[68], the species present in alkaline solution are not expected to be Cu^{2+} ions, but rather CuO_xH_y species which are likely to be responsible for giving the electrolyte its yellow-brownish color.

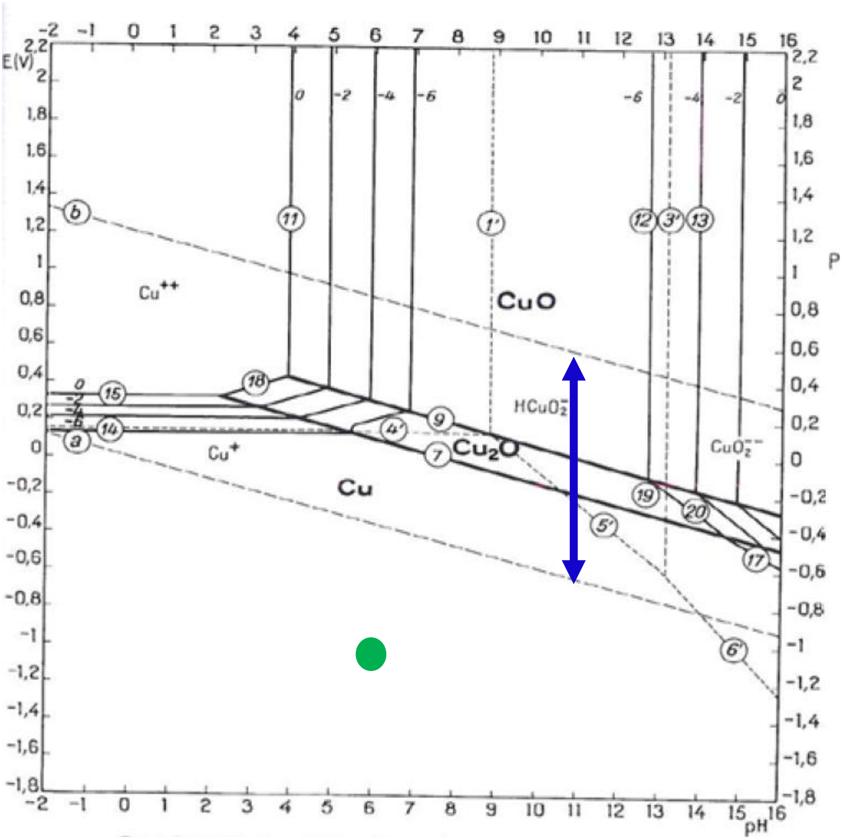

Figure 3.2: Pourbaix diagram for copper in water at 25°C. The blue arrow indicates the potential range where the Cu electrode was cycled during the first step of the nanoparticles formation and the green dot the conditions at which the copper was re-deposited. (Adapted from[68])

In the second step, the copper species in solution were re-deposited by applying a negative potential of -1.3 V vs. RHE in the same $KClO_4$ solution saturated with CO_2, which lowers the pH to a value of ~6. This procedure results in the formation of a rough copper surface due to the formation of copper nanoparticles at the surface, giving the electrode a dark appearance as shown in Figure 3.3.

Figure 3.3: Cu electrode as received (left) and Cu electrode covered with nanoparticles (right).

Sputtered copper: This surface was prepared by argon sputtering of an electropolished copper surface. During this procedure the sample was bombarded with 3 keV Ar^+ ions and 4 µA emission current for 10 min, removing approximately 30 monolayers (~10 nm) from the surface. When the Ar^+ ions hit the sample, they remove copper from the surface generating holes. This process is also accompanied by copper re-deposition and subsequent island formation, giving rise to a slightly rougher surface with respect to the electropolished one.

3.1 Surface characterization

3.1.1 Scanning electron microscopy (SEM)

The surface morphology of the different electrodes was analyzed using SEM. The results show a clear difference in the roughness of the three samples (Figure 3.4).

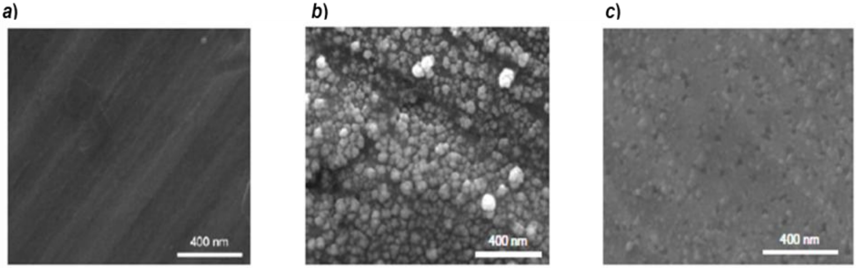

Figure 3.4: Scanning Electron Microscopy for the three surfaces: (a) electropolished surface, (b) copper nanoparticle covered surface and (c) sputtered surface.

The SEM image of the electropolished copper shows a smooth surface, where a low number of defects in comparison to the other two samples is expected. Based on this image and on previous STM studies[66], we believe that the electropolished surface is dominated by low indexed terraces such as (100) and (111), but will also contain a significant number of low-coordinated surface sites such as steps and kinks.

The nanoparticle-covered copper exhibits a surface covered with nanoparticles with sizes between 50 to 100 nm, which roughen the surface. Estimated from the SEM image, the surface area of Sample B is greater than the geometric surface area of the electrode by a factor of 2-3.This surface clearly contains significant amounts of under-coordinated sites.

Finally, the SEM image of sputtered (or sputter-cleaned) copper shows a surface with an intermediate roughness between the electropolished sample and the nanoparticles-covered sample.

3.1.2 X-Ray Photoelectron Spectroscopy (XPS)

The surface composition of the three samples was analyzed by XPS. The sputtered copper only shows the signals belonging to clean metallic copper, with practically no oxygen present. The previous result is not surprising since this sample has been prepared under Ultra High Vacuum (UHV) conditions and has not been exposed to air before the XPS measurements. On the other hand, the electropolished and nanoparticles-covered copper, which were transferred under ambient conditions, show a clear peak at 352 eV consistent with the presence of oxygen at the surface (Figure 3.5*a*). In addition, all three surfaces exhibit the following signals for copper: Cu 2p3/2 at 932.4 eV and Cu 2p1/2 at 952.2 eV, corresponding to metallic copper or copper (I) (Figure 3.5 ***b***). To differentiate between metallic Cu and Cu_2O, we focus on the Auger signal[69] provided in Figure 3.5*c*. Consistently with the lack of oxygen, the Auger spectrum of the sputtered sample corresponds to clean metallic copper. The Auger signal of the electropolished sample also corresponds to metallic copper, whereas the nanoparticles-covered surface shows an Auger peak associated to the presence of Cu_2O. These last two samples were transferred in air, suggesting that the formation of Cu_2O is also related to the surface preparation method and not only to air exposure.

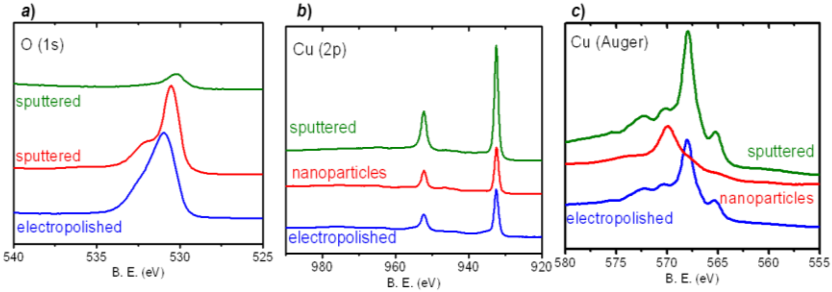

Figure 3.5: XPS spectra of the three surfaces (electropolished, nanoparticles-covered and sputtered): (a) O(1s) signal, (b) Cu(2p) peak (c) Auger peak.

The electropolished copper was prepared applying a positive potential in a phosphoric acid solution (pH 1.5), in conditions under which, according to the Pourbaix diagram of copper, the stable species should be Cu^{2+} and no oxide species are expected. The nanoparticles-covered copper was prepared in 0.1M $KClO_4$ solution in a basic pH range where Cu_2O can be formed. Unfortunately, from the XPS measurements we cannot conclude whether the nanoparticles were oxidized during the re-deposition step, or simply by the exposure of the copper surface in contact with a basic electrolyte to air.

Aiming at clarifying the stage at which Cu_2O was formed, we studied the Auger signals on the sputtered sample in the following cases: under UHV conditions, air exposed (30 min) and after being dipped into a 0.1M $KClO_4$ degassed solution and transferred in air (Figure 3.6). The XPS spectra of these three samples show that the exposure of copper foils to air leads to slightly oxidized surfaces. On the other hand, after dipping the sample into the electrolyte and transferring it in air, Cu_2O is clearly formed on the surface. The last treatment resembles the nanoparticle formation since in both cases the Cu foil is in contact with 0.1M $KClO_4$ and air, indicating that Cu_2O can be formed while transferring the sample and exposing it to air.

This means that XPS measurements are insufficient to determine whether there was also Cu_2O formation while the nanoparticles were prepared. Only *pseudo-in situ* XPS measurements, in which the samples are transferred under inert atmosphere, would allow identification of the surface oxidation state in the electrochemical cell and the active phase under reaction conditions.

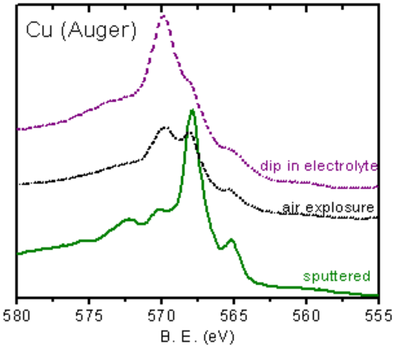

Figure 3.6: Auger peak for a sputtered sample, sputtered sample after air exposure and sputtered sample after immersion in $KClO_4$. The results indicate that Cu_2O is formed when copper is exposed to air and when immersed in electrolyte.

Unfortunately, we are not able to perform this type of measurements to determine whether Cu_2O is present during the reaction. It is highly unlikely, however, that the active phase is a form of copper oxide, rather than metallic Cu as there is a significant driving force for the reduction of copper oxide under reaction conditions, i.e. ~-1.5 V overpotential relative to the Nernst potential of the reduction of Cu_2O to metallic Cu at pH ~6 and -1.1 V vs. RHE. *In situ* STM studies have shown that at the most ~-1 V overpotential is required to completely reduce Cu oxide to form ordered Cu(111) terraces in 0.1 M NaOH,[70] suggesting that at our working conditions (~-1.5 V overpotential) the surface should be fully reduced. Moreover, Le *et al*.[71] found that a Cu-oxide catalyst was reduced to metallic Cu at an overpotential of -1.3 V, relative to the Cu/Cu_2O reversible potential in CO_2 saturated 0.5 M $KHCO_3$.

3.3 Electrochemical measurements

The three surfaces were also characterized by cyclic voltammetry in N_2 and CO_2 saturated 0.1M $KClO_4$. The electrolyte was cleaned by pre-electrolysis to remove traces of impurities applying -1.0V to a Pt wire during 2 hours.

Since the experiments were carried out in a non-buffered solution, the pH value had to be monitored throughout all the steps of the electrochemical process. The as-made electrolyte has a pH of 7±0.5. After the pre-electrolysis, the pH shifted to values close to 8 due to proton consumption. As we are studying a reduction process, the samples where cycled to negative potentials where hydrogen evolution takes place, resulting in a decrease of proton concentration. Surprisingly, the protons formed at the counter electrode do not diffuse fast enough from one compartment to the other, causing a pH shift of the electrolyte in the working compartment towards higher values. As a result of this pH change the CVs in N_2 were recorded at pH values of 11±0.5. This demonstrates the importance of keeping track of the pH value of the electrolyte when working with non-buffered solutions, especially when high current densities are involved.

When the solution was saturated with CO_2, the pH value shifted again to 6±0.5, due to the formation of carbonic acid. It is well known that CO_2 reacts with water to form H_2CO_3, a diprotic acid that is in equilibrium with the deprotonated species:

$$CO_2(aq) + H_2O \leftrightarrow H_2CO_3$$
$$H_2CO_3 \leftrightarrow H^+ + HCO_3^-$$
$$HCO_3^- \leftrightarrow H^+ + CO_3^{2-}$$

To make a fair comparison of the onset reduction potentials in saturated N_2 and CO_2 electrolyte, it is crucial to plot the cyclic voltammograms in the reversible hydrogen electrode (RHE) potential scale, to account for the pH difference. We have used the alignment of the Cu(I)-oxide formation peak, to ensure that the correct pH value was used to establish the RHE potential. According to the Pourbaix diagram of Cu these peaks appear at the same potential against RHE regardless of the pH. The Cu(I)-oxide formation peak is easily identified in the CVs performed in N_2 saturated electrolyte, where an oxidation process due to the formation of copper oxide (I) is observed at around 0.65 V and its reduction is observed during the cathodic scan at ~0.3 V vs. RHE. The previous potential values are consistent with the thermodynamic potential of Cu to Cu_2O at 0.47 V vs. RHE.

The electrochemical reactions which we are focusing on in this work are CO_2 electroreduction and its competing reaction (HER), both occurring at negative potentials vs. RHE. When the electrolyte is saturated with N_2, the cathodic current observed below 0.0 V can only be attributed to the HER. Figure 3.*7a* shows the N_2 voltammograms for the three studied surfaces, where it can be seen that the onset potential for the HER is clearly affected by the surface morphology. The electropolished copper surface shows an exponential increase of cathodic current starting at -0.45 V, whereas the onset potential for hydrogen evolution at the nanoparticles-covered surface and the sputtered surface occurs at lower overpotentials. Moreover, we can also observe a difference in geometric current densities obtained at the three surfaces. This could partially be attributed to the difference in active surface area. However, we can consider that the electropolished sample and the argon-sputtered sample have roughly the same surface area. Therefore, the difference in onset potential and current values between these two electrodes can only be attributed to surface morphology. Furthermore, the difference between the current values for the electropolished electrode and the nanoparticles-covered electrode is greater than the expected from the difference in surface area. For instance, at -0.6 V the current is 4.5 times higher on the nanoparticle-covered surface than on the smooth one. The surface area increase contributes only with the previously estimated factor of 2-3.

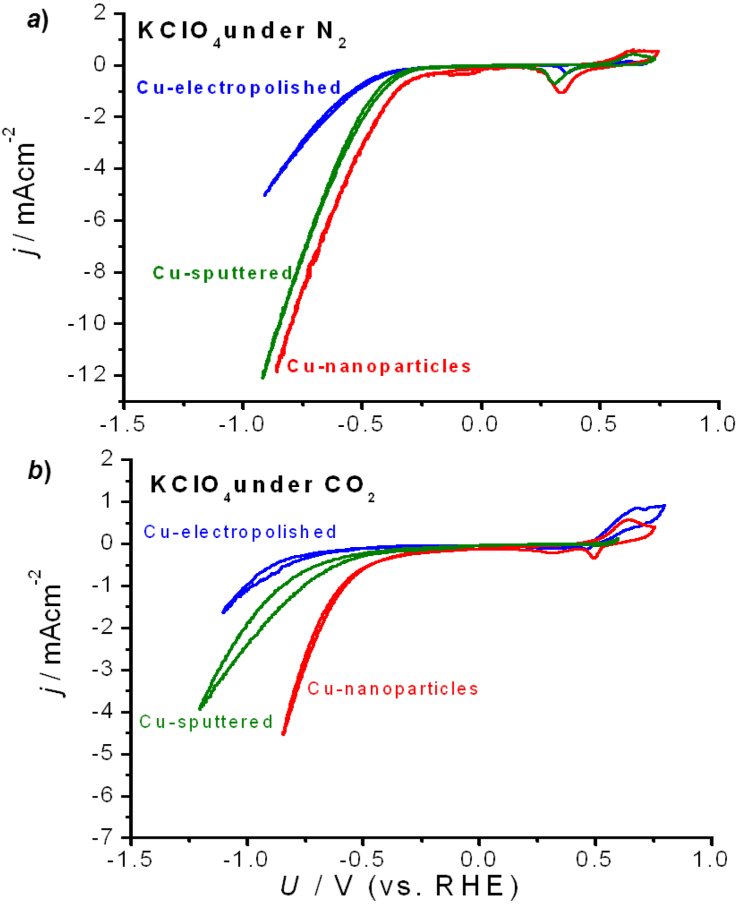

Figure 3.7: Cyclic voltammogram of the electropolished copper surface, copper-nanoparticle-covered surface and sputtered copper surface in 0.1 M $KClO_4$ purged with N_2 (a) and CO_2 (b). The current density is normalized by the geometric area of the electrode surface.

Both the lower overpotential for the reduction current and the higher current density observed on the roughened surfaces suggest that these surfaces have a better electrocatalytic activity towards HER.

When the CVs are recorded under CO_2 (pH 6.0±0.5), we observe a cathodic current due to two reduction processes, HER and CO_2 electroreduction (Figure 3.7.b). On the CVs recorded under CO_2, the onset potentials (defined as the potential at which the current density exceeds 1 $mA/cm^{2)}$, is also shifted towards positive potentials when the surface is smoother. We observed an onset potential on the nanoparticles-covered surface of -0.6 V, while it was -0.8 V for the sputtered surface and -1.0 V for the electropolished surface. The current density is also larger on the roughened surfaces than on the smooth ones. For instance, at -0.75 V vs. RHE, the current density of the nanoparticle-covered surface is 10 times higher compared to the electropolished surface. The difference in active surface area is not enough to explain the difference in geometric current densities, so most of the difference in current density could be attributed to the effect of the surface morphology on the electro-catalytic activity of copper towards CO_2 reduction.

A comparison of the CVs under N_2 and CO_2 shows that larger current densities and lower overpotentials are obtained when cycling under N_2. These results can be an indication of adsorbed species during CO_2 reduction, which block the active sites for hydrogen evolution. According to Hori *et al [24]* the CO_2 reduction reaction proceeds with the formation of adsorbed CO as an intermediate product. At low overpotentials the Faradaic current is provided by two competing reactions:

$$*CO_2 + 2H^+ + 2e^- \rightarrow *CO + H_2O$$

$$2*H^+ + 2e^- \rightarrow H_2$$

(The "" indicates that it adsorbs on the surface)*

3.4 Catalytic testing

The three surfaces were studied as electrocatalysts for CO_2 reduction by applying a constant potential of -1.1 V vs. RHE in CO_2 saturated electrolyte (0.1M $KClO_4$) and measuring the gaseous products after 15 minutes of reaction. The Faradaic efficiencies and partial current densities towards the different gaseous products are shown in Figure 3.8. After this reaction time it was not possible for us to detect any liquid products, given that with the working parameters the detection limit of the HPLC was ~2mM. To be able to quantify the liquid products the reaction was run during 24 hours on the electropolished sample. According to the HPLC analysis, the only liquid product is formate, produced with a faradaic efficiency of 7.5%.

The first thing that is worth noticing from our bulk electrolysis results is that on all surfaces ethylene formation is favored over methane. This is different from what has been observed in $KHCO_3$ electrolyte, where methane is usually the dominant hydrocarbon product at potentials below -1.0V (Figure 2.14).

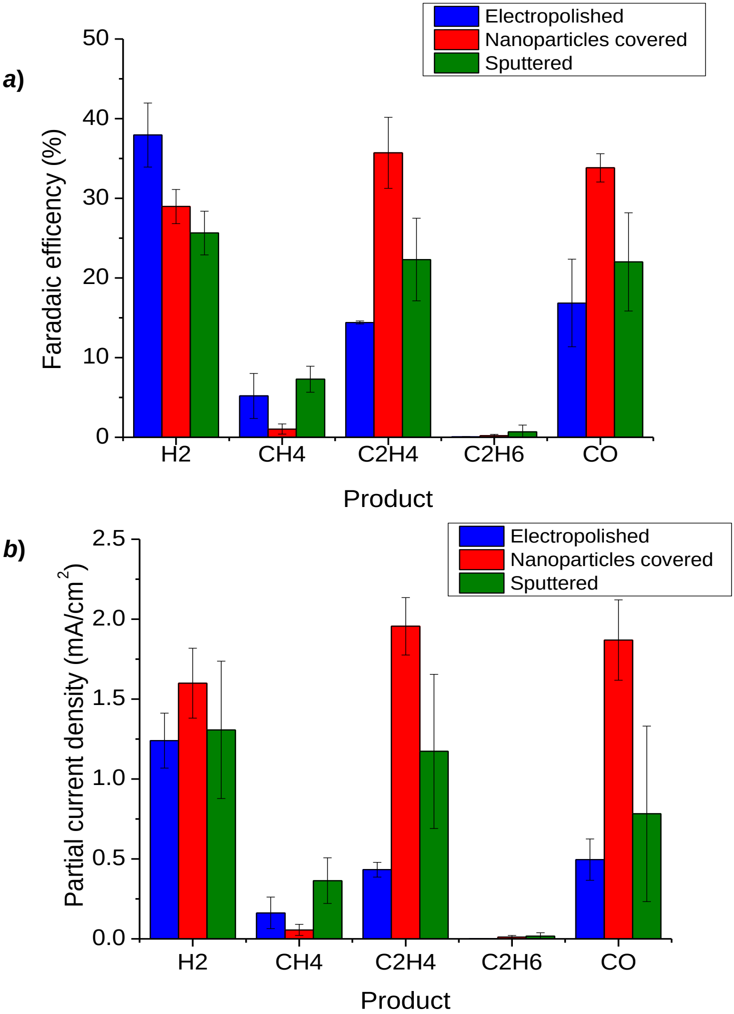

Figure 3.8: Faradaic Efficiency and partial current densities for the products of electroreduction of CO_2 on three surfaces in CO_2-saturated 0.1 M $KClO_4$ at -1.1 V vs. RHE

These discrepancies might be attributed to a higher local pH when working in a non-buffered solution such as $KClO_{4,}$ since it has been shown that high pH favors ethylene formation over methane[14, 21].

Gupta *et al.[72]* have studied the cathode surface pH during the CO_2 electro-reduction in $KHCO_3$ solutions. According to their results, the surface proton concentration is significantly lower than in the bulk. Furthermore, the local pH depends on the total current density and the buffer capacity of the electrolyte.

Figure 3.9, taken from the works of Gupta and co-workers shows local proton and CO_2 concentration as a function of buffer strength (concentration of $KHCO_3$) when the current density is 5mA/cm^2

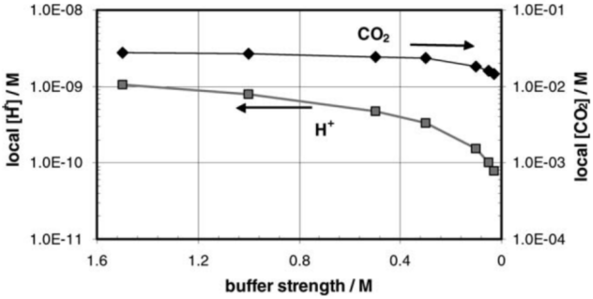

Figure 3.9: Proton and CO_2 local surface concentrations as a function of buffer strength (from 1.5M $KHCO_3$ to 0.03M $KHCO_3$) when the CO_2 reduction current is 5mA/cm^2 (From[72]).

According to Figure 3.9 the local pH is always higher than in the bulk, which depending on the $KHCO_3$ concentration ranges from 6 in 0.03 M $KHCO_3$ to around 8 in 1.5 M $KHCO_3$. The difference between the bulk and the surface pH is greater when the buffer capacity is low, reaching more alkaline local pH values as the concentration of $KHCO_3$ decreases. Consistently, studies of CO_2 electroreduction in different $KHCO_3$ concentration have shown that a lower buffer capacity enhances ethylene formation, presumably due to a higher local pH [14].

Our results are obtained in CO_2 saturated 0.1 M $KClO_4$, which has an extremely low buffer capacity, suggesting that the local pH should be higher than when CO_2 reduction is performed in $KHCO_3$. A higher local pH can account for the improved production of ethylene over methane in 0.1 M $KClO_4$ compared to published results in $KHCO_3$[14, 15].

From the results in Figures 3.8 and 3.7 we can also see that the catalytic activity of the three surfaces is significantly different. The analysis of the gaseous products shows also that the studied surfaces have different product selectivity. Performing CO_2 electrolysis measurements on rough surfaces decreases the selectivity towards hydrogen evolution and favors CO_2 reduction. In addition, the ratio between the products of CO_2 reduction is also affected by the surface morphology. The electropolished surface produces C_2H_4 with the Faradaic efficiency of 14% and CH_4 with 5%. On the other hand, on nanoparticles-covered surfaces ethylene formation is enhanced to a 36% Faradaic efficiency, while the selectivity towards methane is only 1%. Sputtered copper, which has an intermediate roughness between the electropolished and the nanoparticles-covered sample, exhibits intermediate Faradaic efficiency towards C_2H_4 (26%) and the highest Faradaic efficiency towards CH_4 (8%) of all three surfaces. While the methane/ethylene ratio is different on the studied surfaces, our results indicate that CO and ethylene formation follows the same trends. Higher CO production seems to favor the formation of ethylene, suggesting a correlation of these two products.

If we now focus on the partial current densities (normalized to geometric surface area), we notice that the nanoparticles-covered sample has the highest partial current towards H_2, C_2H_4 and CO and the lowest CH_4 partial current density.

Overall, these results suggest that the production of ethylene is favored on roughened Cu surfaces, while methane formation is suppressed. Our observations are consistent with published results which also suggest a dependence of the surface morphology on the catalytic activity of copper. Branco and co-workers[19] showed that by modifying a copper electrode through copper electrodeposition, i.e. making it rougher, methane formation was suppressed. A more recent paper by C.W. Li *et al[22]* presents results on roughened copper obtained by reducing a thick layer of Cu_2O. Using this preparation method they have achieved an extremely rough surface (roughness factor ~30) in which the reduction CO_2 to CO requires 0.2 V less overpotential than on polycrystalline Cu. Furthermore, on this surface the only hydrocarbons detected are C_2H_4 and $C_2H_{6.}$

The difference in selectivity between the rough and the smooth surfaces can be explained by two different effects: a different **local pH** due to different current densities and a difference in **surface morphology**.

3.4.1 Local pH effect on the selectivity of different copper surfaces

The enhanced production of C_2 compounds on rough surfaces may be partially explained by a local pH effect. On rough surfaces the geometric partial current densities are higher than on the smooth ones. Therefore, as a general trend, a higher local pH can be expected on the rough surfaces in comparison with smooth surfaces, which inhibits methane formation. The exact value of the local pH, however, varies from system to system since it is determined by the current densities, the buffer capacity of the electrolyte and the thickness of the diffusion layer. On extremely rough surfaces like the ones studied by Kanan and co-workers,[22] where high current densities are obtained, the effect of the local pH should play a more significant role than on moderately roughened surfaces.

On the surfaces studied here we could expect a considerable difference in the local pH, as the total current densities varies by a factor of 2.5 and the reaction takes place in an electrolyte with a low buffer capacity. This difference can influence the selectivity of the reaction, favoring ethylene formation on the nanoparticles-covered sample on which a higher local pH is expected.

3.4.2 Surface morphology effect on the selectivity of different copper surfaces

The different facets present in each surface also play a key role in the catalytic activity of the different copper surfaces. As has been shown by Hori and coworkers[13, 73], the crystal orientation of copper has a strong effect on its catalytic activity. Their work has been carried out at a constant current; consequently the local pH does not play a role since it should be the same on all the studied surfaces. Hori *et al*. observed that on stepped surfaces, like Cu(311), Cu(511) and Cu (711), the reaction occurs at lower potentials for a specific current density compared to the low index facets Cu(111) and Cu(100). They also concluded that the selectivity ratio between CH_4 and C_2H_4 depends strongly on the crystal orientation. They reported that Cu(111) produced CH_4 with a Faradaic efficiency of 50.5% and C_2H_4 with an efficiency of 8.8 %. On the other hand, the stepped surface Cu(711) exhibited only a modest Faradaic efficiency of 3.8% towards CH_4 and 51.6% towards C_2H_4. These results indicate that steps are more selective towards ethylene production while terraces are more selective towards the formation of methane.

3.4.3 Mechanism insights

To have a better understanding of the difference in catalytic activity of the different crystal orientations, we can use the input from Density Functional Theory (DFT) on the HER and CO_2 reduction at different copper facets (fcc(111), fcc(100) and fcc(211)). DFT studies give insight into the reaction pathways based on the free energy diagrams of products, reactants and reaction intermediates.

For HER, the only intermediate is adsorbed hydrogen (*H), meaning that the theoretical activity of a given surface depends only on the free energy of *H.

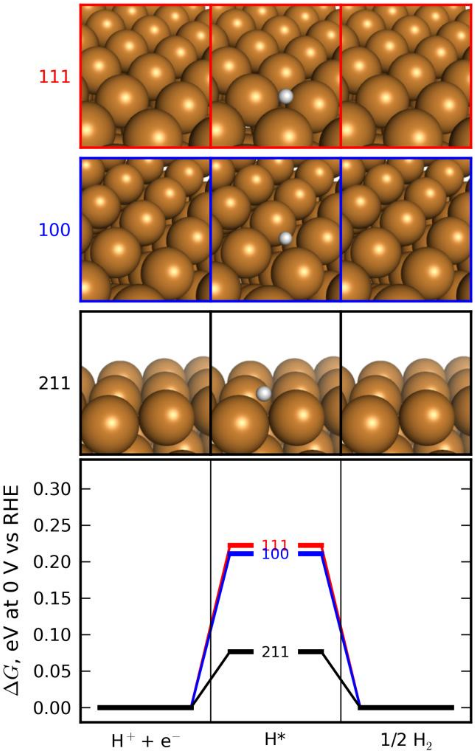

Figure 3.10: Calculated free energies of the hydrogen evolution reaction on the (211), (111), and (100) surfaces of a Cu fcc crystal

The work of Duran *et al*, [74](Figure 3.10), predicts that the stepped sites (211) have higher activity for HER than the (111) and (100) terraces, due to a lower *H free energy on Cu(211) than on Cu(111) and (100). The prediction of higher activity for a stepped surface is in agreement with the higher current obtained during cyclic voltammetry of the nanoparticles-covered sample, which contains a higher number of steps and kinks.

We studied the CO_2 electrochemical reduction using the mechanism proposed by Peterson *et al[23]*, where the elementary proton-electron transfer steps have been proposed for the process of reducing CO_2 to methane on a (211) copper surface. They have proposed that the rate limiting step is the reduction of *CO to *CHO. Furthermore, in a recent paper, Nørskov and coworkers[28] have suggested, that this is also the rate limiting step for the formation of ethylene and that C_2 compounds are formed from a non-electrochemical surface reaction between adsorbed species, for example the coupling of two *CHO moieties to form *OCHCHO*.

Based on these calculations, we used the free energies of the transformation of *CO to both *CHO and *COH with the aim of understanding the different catalytic activity of different copper surfaces. Figure 3.11 compares the energetics of *CO protonation on the (111), (100), and (211) surfaces at 0 V vs. RHE. It can be seen, that according to the thermodynamic analysis, on all surfaces the route to *CHO is favored over the route to *COH. Additionally, the (211) surface facilitates the formation of *CHO relative to the (111) and (100) surfaces.

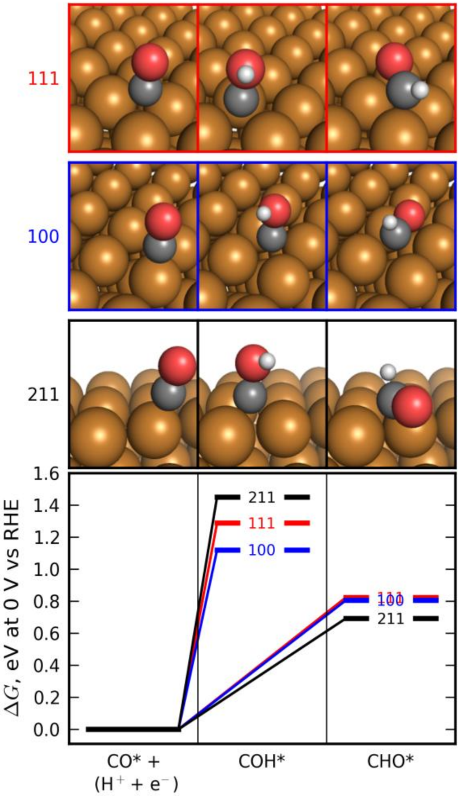

Figure 3.10: Calculated free energies of water oxidation on the (211), (100), and (111) facets of the Cu crystal at 0 V vs RHE. According to these calculations, a potential of -0.31 V vs RHE is necessary to reduce the (211) step sites to enable hydrogen evolution

These results indicate that if the rate limiting step in hydrocarbon formation is the protonation of *CO to *CHO, roughened surfaces should be more active towards CO_2 reduction, thus explaining the higher current densities obtained on the nanoparticles-covered sample. Bear in mind, however, that this is purely a thermodynamic analysis and no kinetic barriers were considered. A recent study by

Nie *et al*. concluded that *COH formation is kinetically favored over that of *CHO, in contrast with the conclusions drawn from thermodynamics[27].

It has been suggested, that the high selectivity towards C_2H_4 and the suppressed CH_4 production on the rough surfaces may be attributed to a high coverage of *CHO that facilitates the C-C coupling. In my opinion, however, the difference in selectivity towards methane and ethylene on different copper surfaces is not fully explained by a mechanism in which both products share the same intermediate. Furthermore, there are studies showing that the formation of methane depends on proton concentration[24], while the formation of ethylene is independent of pH. This is consistent with *CO protonation being the limiting step for methane formation, but it also suggests that the limiting step for ethylene production should be a different one with no proton transfer involved in it or before to ensure pH independence.

Unfortunately, the discussion of the difference in selectivity towards methane and ethylene remains highly speculative since the mechanism for the formation of ethylene is still on debate. On one hand, Koper and co-workers have suggested that the C-C coupling occurs via the formation of a CO dimer.[16, 21] While, Nørskov and coworkers proposed the C-C bound is formed after *CO is protonated since *CO dimerization is kinetically less favorable than other C-C couplings, e.g. CHO-CHO coupling.[28]

3.5 Conclusions

i. This work presents an easy *in situ* electrochemical method to activate polycrystalline copper and make it more selective towards the production of ethylene by surface roughening.

ii. Surface pretreatment and thus surface morphology of the copper electrode affect both activity and selectivity for the CO_2 electro-reduction in aqueous solutions. Rough surfaces exhibit higher activities and higher selectivity toward CO_2 reduction products, in particular ethylene. On the other hand, rough surfaces exhibit lower selectivity towards the production of hydrogen.

iii. Working with neutral non-buffer solutions requires extreme care to establish the correct pH under working conditions. The bulk pH in a CO_2 free electrolyte is extremely sensitive to high current densities that affect the equilibrium between H_2O, H^+ and OH^-. In CO_2 saturated electrolyte the formation of carbonic acid permits to keep the bulk pH constant. The buffer capacity of the electrolyte, however, would be low causing important differences in local pH, which should be taken into account.

iv. The morphology effect can be explained by the different facets present in each surface. Smooth surfaces contain predominately low index facts such as (111) and (100), while roughened surfaces have a greater number of under coordinated sites. According to DFT calculations, uncoordinated sites simulated using a (211) surface are more active towards HER and CO_2 reduction. Note, however, that (211) surfaces are short (111) terraces with (100) steps and thus, more modeling is required to determine the effect on the activity of terrace length and coordination and the kind of steps.

v. To get a better understanding of the difference in selectivity towards methane an ethylene, it is necessary to make a detailed mechanistic study of the C-C bond formation and consider other factors such as the local pH.

Chapter 4

4. Copper overlayers on Pt single crystals as electrocatalyst for CO_2 reduction

This chapter focuses on the catalytic activity of copper overlayers on Pt(111) (Cu/Pt(111)) and on Pt(211) (Cu/Pt(211)) towards the CO_2 electro-reduction. The aim of these studies was to investigate whether having an expanded Cu surface would improve the catalytic activity of pure copper[37].. Furthermore, by studying this reaction on different facets we can obtain information about the role of steps on the CO_2 electro-reduction.

The efficiency and selectivity of the copper overlayers was investigated by cyclic voltammetry and bulk electrolysis experiments. In addition we have carried out experiments to determine the stability of the overlayers in the presence of CO, which is a well-known intermediate of the CO_2 electro-reduction.

4.1 Surface preparation and electrochemical characterization

4.1.1 Pt single crystals

This study was carried out using Pt(111) and Pt(211) single crystals with 10mm in diameter. The area of the crystals was chosen to be as big as possible to have high reaction currents and facilitate the quantification of the reaction products.

Before any experiments the Pt single crystals were annealed at 850±20°C in a 5% H_2 in Ar atmosphere for 3 min, followed by annealing in a 1% CO in Ar atmosphere for 1 min at 850±20°C. After annealing the crystals, they were characterized by cyclic voltammetry in argon saturated 0.1 M $HClO_4$ (Merck, Suprapur) and in 0.1 M $KHCO_3$ between 0.05 V and 1.0 V vs. RHE (Figure 4.1). The $KHCO_3$ solution was prepared by bubbling CO_2 through a 0.1 M KOH solution (Merk, suprapure) until the pH value was stable (pH=6.8).

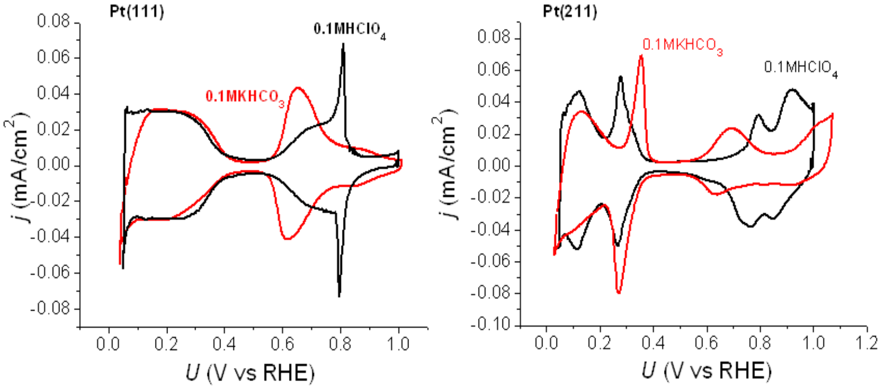

Figure 4.1: Cyclic voltammograms at 50mV/s of Pt(111) (left) and Pt (211) (right) in argon saturated 0.1M $HClO_4$ (black line) and 0.1M $KHCO_3$ (red line)

The CVs in $HClO_4$ for both surfaces are consistent with those in literature.[75, 76] The region between 0.05 and 0.4 V, historically known as the hydrogen UPD region, is clearly different for the two crystals. In the case of Pt(111) this signal appears almost flat at the top, while for the Pt(211) two distinct peaks are observed at approximately 0.1 V and 0.3 V. For Pt(111) the CV exhibits the characteristic reversible signal for *OH adoption between 0.6 V and 0.8V with a peak current density of approximately 70 μA/cm^2. When the electrolyte is exchanged to 0.1M $KHCO_3$ the *OH signal is suppressed, presumably due to the physisorption of HCO_3^-. *[77, 78]*

4.1.2 Copper overlayers

Copper was deposited by underpotential deposition (UPD)[79, 80] on to the Pt crystals. This process consists of the deposition of Cu on top of a different metal at potentials less negative than, allowing the formation of up to one monolayer of copper on the substrate.

$$E_{eq} = E° + \frac{RT}{2F} ln \frac{a_{Cu^{2+}}}{a_{Cu}} \qquad \textit{(eq. 4.1)}$$

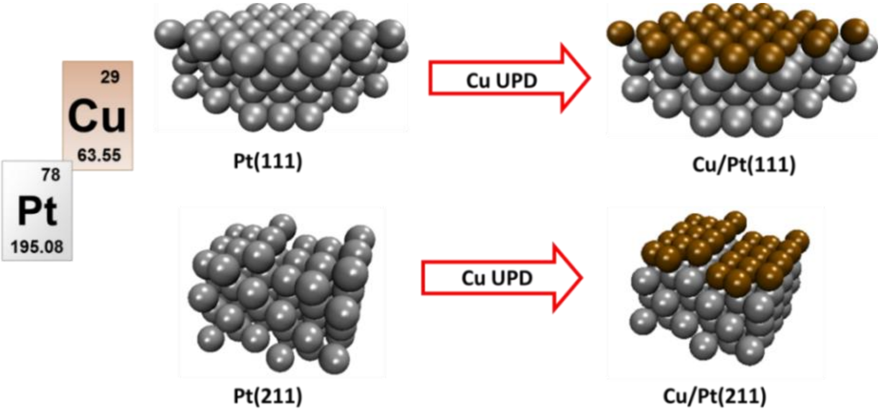

Figure 4.2: Schematic representation for the formation of the Cu overlayers on Pt(111) and Pt(211)

During the Cu UPD each Cu atom sits on top of a Pt atom resulting in an expanded Cu surface that retains the lattice parameters of Pt. On this structure the reactivity of copper is modified due to a combination of ligand and strain effects. As discussed in the introduction, the copper d-band is shifted upwards when deposited onto platinum. This makes the strained copper surfaces more reactive than pure copper.

Copper was deposited from a 3 mM $Cu(ClO_4)_2$ solution in 0.1 M $HClO_4$ (prepared from CuO 99.9995% Alfa Aesar and $HClO_4$ Merck, Suprapur). To ensure the formation of only one monolayer, the potential was kept at 0.32 V vs. RHE, for 2 minutes. At these conditions a pseudomorphic Cu overlayer on Pt should be formed. The deposited amount of Cu was controlled by measuring the charge required for the anodic dissolution of the Cu overlayer (Figure 4.3), known as Cu stripping.

Figure 4.3 shows the Cu stripping after holding the potential at 0.32 V in 3 mM $Cu(ClO_4)_2$ solution in 0.1 M $HClO_4$ for two minutes. On Pt(111) the dissolution of copper appears at ~0.42V more positive than the Nernst potential for Cu oxidation, consistent with copper being stabilized by the Pt substrate. The obtained oxidation peak is an extremely sharp feature indicating a strong attractive interaction between copper atoms.[81] When the first copper atom is removed, the whole overlayer becomes unstable and it is all oxidized at the same potential. This is clearly not the case for the overlayer on

Pt(211) where a broad signal is obtained. Furthermore, Cu oxidation starts at 0.4 V which corresponds to near bulk oxidations that is expected to be formed on steps sites.[82]

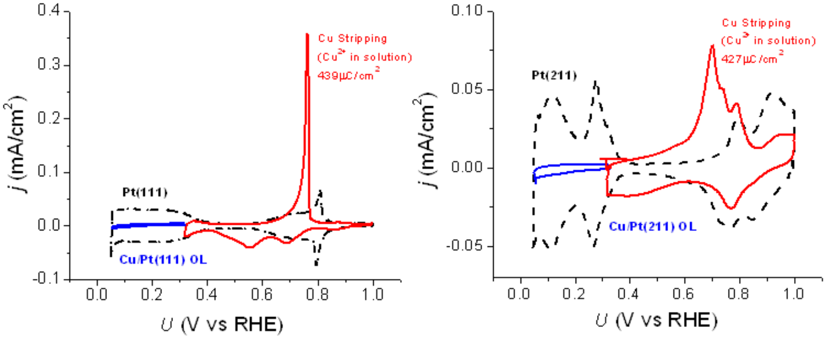

Figure 4.3: Cyclic voltammograms at 20 mV/s of Pt(111) (left side) and Pt (211) (right side) in 3mM CuClO4 and 0.1M $HClO_4$ solution after holding the potential for 2 minutes at 0.32V vs. RHE (red line). Compared with the cyclic voltammograms at 50mV/s of the clean Pt single crystals (black dash line) and the Cu/Pt overlayers (blue line).

After the formation of the Cu overlayer by copper UPD, the Cu containing solution was removed by exchanging the electrolyte to clean 0.1M $HClO_4$ under potential control at 0.32V vs RHE. Then the Cu overlayers were characterized by cyclic voltammetry between 0.05 and 0.32V where we can observe that the signal in the hydrogen UPD region is suppressed, as it has been reported previously.[83]

4.2 Catalytic test

4.2.1 Cyclic voltammetry studies

Cyclic voltammetry in 0.1 M $HClO_4$ was also used as an initial, qualitative evaluation of the catalytic performance of the four different surfaces under Ar, CO and CO_2. It is important to notice that under these conditions, most catalysts show a poor selectivity towards CO_2 reduction relative to hydrogen evolution. For this reason CO_2 reduction experiments are not usually carried out in acidic solution. This is mainly due to the hydrogen evolution reaction being orders of magnitude more active in acid than in neutral or basic electrolytes[84]. Nonetheless, the advantage of carrying out these measurements in perchloric acid is that the pH will not change significantly upon changing the purge gas, as it would in $KClO_4$. Bulk CO_2 electrolysis is usually carried out in $KHCO_3$, however when this electrolyte is saturated with a gas other than CO_2 the pH shifts due to the removal of CO_2 affecting the equilibrium between H_2CO_3 and HCO_3^-.

The CVs of the Pt surfaces under Ar show a reduction current due to hydrogen evolution reaction (HER). As expected the onset potential, defined as the potential needed to draw a current of at least $0.1 mA/cm^2$, is close to 0.0V vs RHE. In the presence of CO_2, however, the onset for the reduction current on Pt(211) is shifted to more negative potentials whereas it remains the same for Pt(111). Presumably, this shift is caused by reduction of CO_2 to adsorbed CO (*CO) that blocks some of the active sites for the HER[85].

According to Hori and co-workers[86] Pt flat surfaces such as (100) and (111) are inert towards CO_2, while stepped surfaces reduce CO_2 to *CO explaining why only on the Pt(211), the onset for the HER is moved to higher overpotentials

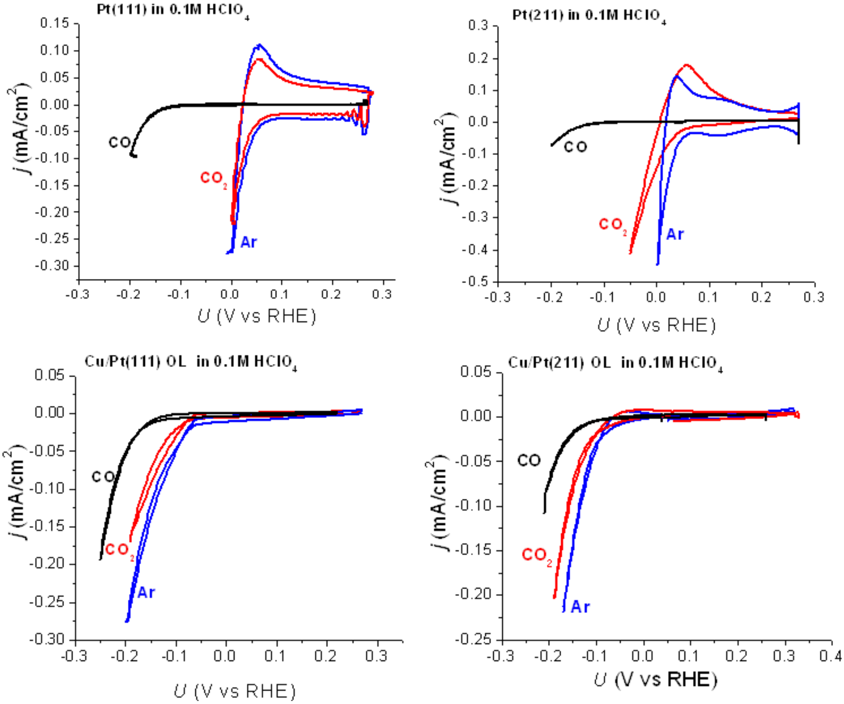

Figure 4.4: Cyclic voltammograms at 50mV/s of Pt(111), Pt(211), Cu/Pt(111) OL, Cu/Pt(211) OL in 0.1M $HClO_4$ saturated with argon (blue line), CO_2 (red line) CO (black line)

Furthermore, after cycling for 20 minutes between -0.05V and 0.3 V under CO_2, we exchanged the electrolyte to Ar saturated 0. 1M $HClO_4$ and changed the upper limit of the CVs to 1.1 V (Figure 4.5). The resulting CV for the Pt (211) presents a positive peak consistent with the oxidation of ½ monolayer of *CO corroborating that CO was formed during the previous cycling. The CV of Pt(111) presents a small shoulder at ~0.7V that can also be attributed to oxidation of *CO. This peak, however, corresponds to a small amount of CO that is likely formed at the defects of the Pt(111) crystal.

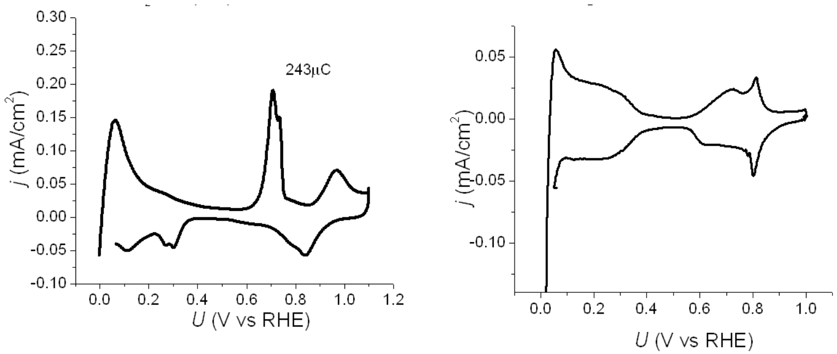

Figure 4.5: Cyclic voltammograms at 50mV/s of Pt(211), and Pt(111) under Ar after cycling towards negative potentials in the presence of CO_2

In figure 4.4 it can also be seen that in the presence of CO the onset potential for the reduction current on the Pt single crystals is shifted to approximately -0.2 V. It is well known that in the potential range these CVs were performed, CO is adsorbed onto Pt surfaces blocking ~70% the atoms[87]. As a result the HER is inhibited.

For the copper overlayers there is not a significant difference between the obtained voltammograms on the studied two crystals. The onset potential for HER in Ar saturated 0.1M $HClO_4$ shifts approximately 0.1V with respect to the Pt surfaces. This is intuitive, on the basis that Cu is much less active for the HER than Pt[88]. In the presence of CO_2, there is a small shift at more negative potentials, which might be due to the formation of adsorbed CO. When the electrolyte is saturated with CO there is a clear shift to higher overpotentials consistent with the adsorption of CO and the blockage of the active sites.

4.2.2 Bulk electrolysis studies

Potential dependence bulk electrolysis

On the basis of the voltammetric experiments described previously, the selectivity towards CO_2 reduction and hydrogen evolution of the surfaces under study, cannot be verified. For this purpose, potentiostatic bulk electrolysis experiments were performed. These were conducted in 0.1 M $KHCO_3$, at potentials ranging from -0.7 V to -1.2 V, RHE, with each experiment lasting 15 minutes. For each potential a fresh Cu overlayer was prepared to ensure that adsorbates from a previous reaction do not influence the catalytic result. The gas phase products were identified using gas chromatography (GC). These bulk electrolysis measurements were compared with the obtained results on polycrystalline Cu in the same set up.

It is important to notice that these experiments were conducted at much more negative potentials that the onset for the reduction current. Similar to polycrystalline copper, these surfaces start producing hydrocarbons at high overpotentials (roughly -0.7V vs RHE) [14, 15]. However, one should be careful to compare the catalytic results at these high overpotentials, since under these conditions the catalytic results are strongly affected by local pH effects and mass transport limitations.

When Pt(211) was used as a catalyst, hydrogen was the main product accompanied with traces of methane (Faradaic efficiencies below 0.2%). For the CO_2 reduction on the Cu/Pt(111) and Cu/Pt(211) hydrogen and methane were detected as the main products together with traces of ethylene (Faradaic efficiencies below 0.6%). CO was not detected; however, volumetric CO concentrations lower than 0.1% are below the GC detection limit. Therefore, it is not possible to determine Faradaic efficiencies lower than 15% for CO when working in a high volume electrochemical cell as the one used in these single crystal studies. The unbalanced Faradaic efficiency is attributed to the undetected CO and to $HCOO^-$ in the liquid phase.

Figure 4.6 shows the potential dependence of H_2 and CH_4 production in terms of Faradaic efficiencies and current densities. We believe that the high dispersion of the results from the overlayers is partially caused by wetting the edges of crystal. The bubbling during the reaction makes it challenging to keep the edges dry, so in some cases they contribute to the total current. Since the edges consist of Pt that efficiently produces hydrogen, we expect that wet edges produce a higher total current and a higher hydrogen partial current density. The edges, however, should have a negligible contribution to methane production and thus the methane partial current density should not be affected by wet edges.

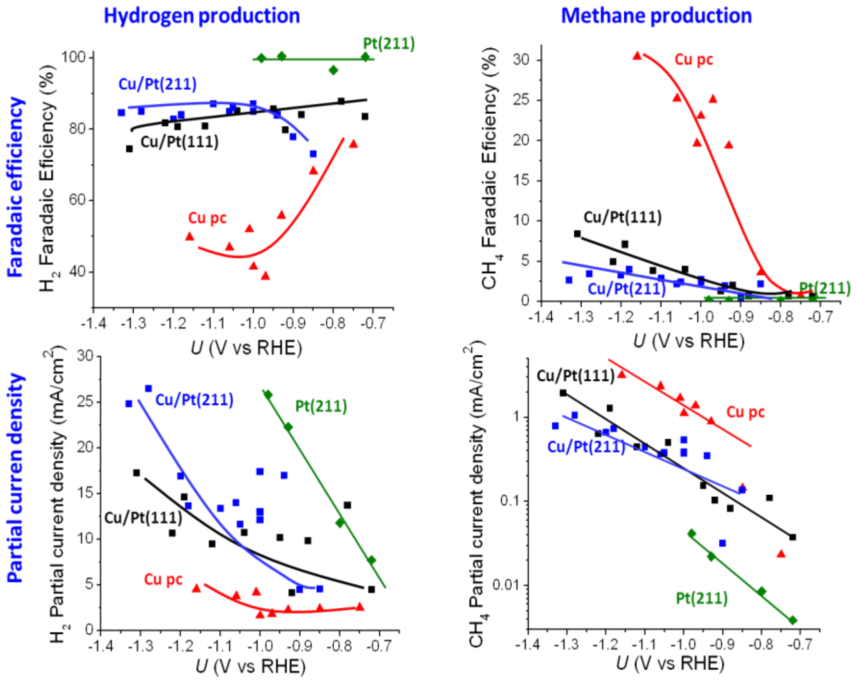

Figure 4.6: Faradaic efficiencies and partial current densities towards CH_4 and H_2 as function of potential on Pt(211) (green), Cu/Pt(211) (blue), Cu/Pt(111) (black) and polycrystalline Cu (red) after 15 minutes of bulk electrolysis in CO_2 saturated 0.1M $KHCO_3$. (Lines are there to guide the eyes).

Based on the partial current densities, it was possible corroborate that Pt(211) is the most active surface towards HER while polycrystalline copper is the least active one. The Faradaic efficiencies are used to determinate how selective each surface is towards a given product, so the almost 100% efficiency towards hydrogen on Pt(211) indicates that this surface is highly selective towards hydrogen production. Polycrystalline copper has the lowest selectivity towards H_2 and its selectivity clearly depends on the potential reaching a minimum value at -1.0 V. The H_2 selectivity of Cu/Pt (111) and Cu/Pt(211) Cu are around 80%, in between pure Cu and pure Pt, and does not show a clear trend with potential.

On the overlayers methane starts to form at around -0.7 V as on polycrystalline copper and its Faradaic efficiency and partial current densities increase when going to more negative potentials. At low overpotentials the partial current densities towards methane on the Cu overlayers are comparable with those obtained on polycrystalline copper. However, at high overpotentials polycrystalline copper is clearly more active towards methane production.

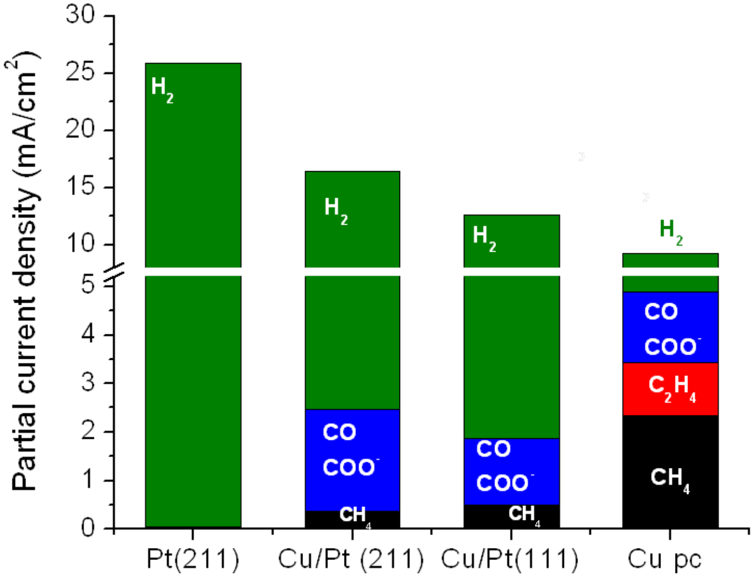

Figure 4.7: Partial current densities for the products of bulk CO_2 electrolysis at -1.0V vs. RHE on Pt(211), Cu/Pt(211), Cu/Pt(111) and polycrystalline Cu in CO_2-saturated 0.1 M $KHCO_3$

Figure 4.7 shows the partial current densities towards all the reaction products at -1.0 V. It is clear that the most active surface is Pt(211), however, it is extremely selective towards hydrogen evolution. The Cu/Pt(211) is slightly more active than the Cu/Pt (111) which is attributed to a higher activity of the step sites. According to the total current density the Cu overlayers are more active than the polycrystalline copper. This difference in activity is mostly due to a higher activity towards HER. The partial current density towards methane is comparable on both Cu overlayers but considerable lower than on polycrystalline copper. On polycrystalline copper methane's partial current density is ~2 mA/cm^2, while on the overlayers it is ~0.5mA/cm^2, indicating that polycrystalline copper is approximately 4 times more active towards methane production. It is also interesting to note that, while on polycrystalline copper ethylene is one of the major products, Cu/Pt (111) and Cu/Pt(211) only produce traces of it.

Overall, the bulk electrolysis results suggest that the copper overlayers do not have a better catalytic activity than pure copper. Furthermore, there is no significant difference between Cu/Pt(111) and Cu/Pt(211). Before concluding if there is an effect of having an expanded copper surface, it is important to corroborate if copper remains as a pseudomorphic overlayer during the reaction.

Time dependence of bulk electrolysis

With the aim of gathering more insight on the catalytic activity of Cu/Pt(111) towards CO_2 reduction, we studied the product distribution as a function of time. This experiment would provide information of whether the surface has a stable catalytic activity or if it changes with reaction time. The catalyst could be activated or deactivated during the reaction, which would indicate that the surface is being modified. In addition, we also studied the electro-reduction of CO as a function of time. As previously mentioned, CO is a well-known intermediate for the reduction of CO_2 to hydrocarbons. However it has also been observed that CO can induce surface segregation of the most reactive component, which in this case is Pt.[52, 89]

For these studies a constant potential of -1.0 V(RHE) was applied during one hour while the gaseous products were analyzed by gas chromatography after 5, 10, 15, 30 and 60 minutes of reaction. The reaction was performed in CO_2 saturated 0.1 M $KHCO_3$ and CO saturated 0.1 M $KHCO_3$. When CO_2 is bubbled through the electrolyte the pH remains stable at ~6.8, while CO shifts the pH value to ~8. The liquid products were analyzed by HPLC after one hour of reaction. Formate was the only detected liquid product from the electro-reduction of CO_2, with a Faradaic efficiency of only 1.4%, while for the electro-reduction of CO no liquid products were detected.

Figure 4.8 shows the Faradaic efficiencies and partial current densities towards methane, hydrogen and the products corresponding to the unbalance Faradaic efficiencies. In the case of the reduction of CO_2 the unbalanced current can be attributed to the production of CO, below the GC detection limit and $HCOO^-$ in the liquid phase. While for the reduction of CO these two are not feasible products, thus the unbalanced current is mainly due to an artifact of the measurements, and corresponds to less than 5% of Faradaic efficiency.

The time dependence for the production of methane is very different when we started from CO_2 than when we started from CO. This is a very interesting result since CO is known to be a key intermediate for the reduction of CO_2 into hydrocarbons. Catalytic results on Cu surfaces have shown that the same hydrocarbon distribution is obtained from the reduction of CO and $CO_{2.}$ This is clearly not the case for Cu/Pt(111), in which methane production is very different when reducing CO compared with the reduction of CO_2, especially at short reaction times. After half an hour of reaction, the production of methane on Cu/Pt(111) is comparable for the reduction of CO and the reduction of CO_2 suggesting a similar catalytic process.

The production of methane from CO_2 decreases drastically during the first 15 minutes of reaction while hydrogen formation is enhanced. This result suggests that the surface is being modified during the reaction affecting its catalytic activity. On the other hand, the catalytic activity of the Cu/Pt(111) towards the reduction of CO does not change that drastically during the reaction.

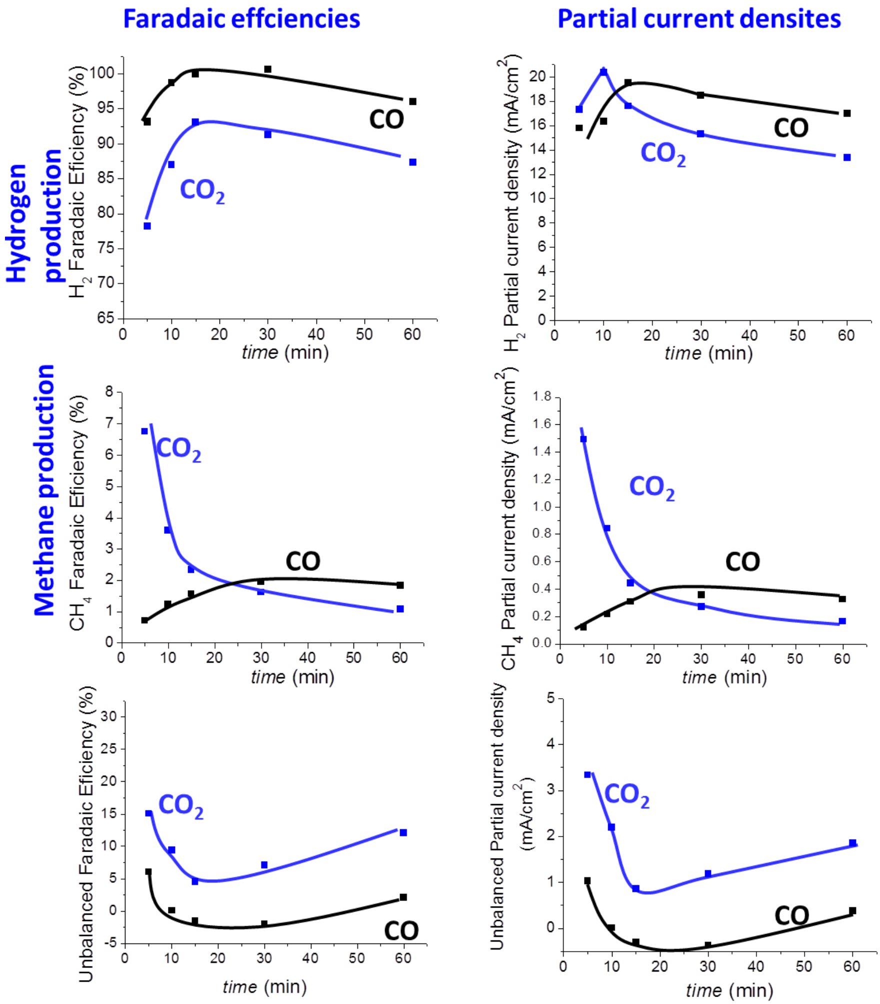

Figure 4.8: Faradaic efficiencies and partial current densities towards CH_4 and H_2 and unbalanced products as a function of time, for the reduction of CO_2 (blue) and CO (black) at -1.0V(RHE) in 0.1M $KHCO_3$ (lines to guide the eyes).

The high amount of unbalanced products during the first 5 minutes can be attributed to poor mixing in the reaction cell that causes underestimation of the formed products.[I] This artifact is also expected from the reduction of CO_2 which makes us believe that the production of methane at the beginning of the reaction is higher than the estimated. The increase in partial current density for the reduction of CO to methane during the first 15 minutes of reaction is partially explained by this underestimation of the reaction products.

These results are an indication that CO is inhibiting methane formation on Cu/Pt (111). We believe that the decay of methane production from the reduction of CO_2 is also caused by CO formed from the reduction of CO_2. At the beginning of the reaction the surface is a pseudomorphic copper overlayer on Pt(111), on this surface CO_2 is reduced to CO and then to methane. However, the presence of CO in the surfaces induces changes on the copper layer, modifying its catalytic activity and favoring hydrogen evolution.

4.2.3 Summary

In summary, the catalytic studies indicate that Cu/Pt(111) and Cu/Pt(211) have a different catalytic activity than pure Cu and pure Pt. The Pt surfaces are the most active, but they are also highly selective towards HER. According to the cyclic voltammetry, on

---

[I] The volume of the electrochemical cell and the gas lines connecting it to the GC is estimated to be 185mL, while the recirculation flow of the reaction gases is ~100mL/min. After 5 minutes the gas concentration close to the electrolyte is expected to be different from that close to the GC injector.

Pt(211) CO_2 is reduced to *CO, while Pt(111) is inert. However, bulk electrolysis showed that only traces of *CO are further reduced to methane and that Pt (211) is highly selective towards HER. The Cu overlayers present intermediate activities between Pt and Cu. Their selectivity towards hydrocarbons, however, is considerably lower than on pure Cu.

The activity of Cu/Pt(111) towards the electro-reduction of CO_2 decreases with reaction time, suggesting that the surface is being modified. This may be attributed to the presence of CO, which, as has been shown, inhibits the formation of methane on Cu/Pt(111). Studies on the stability of the overlayer in the presence of CO may help understanding the poor selectivity of the Cu overlayer towards hydrocarbon formation.

4.3 Surface characterization after bulk electrolysis

To ensure that the decay on methane production during the reduction of CO_2 is not due to surface contamination the Cu/Pt(111) surface was characterized after one hour of bulk electrolysi using angle resolved X-Ray photoelectron spectroscopy (XPS) . Figure 4.9 shows the depth profile obtained by Paolo Malacrida on Cu/Pt(111)

According to these results, the surface is clean and it consists of Pt and Cu covered by $KHCO_3$, indicating that the deactivation of Cu/Pt(111) is not caused by surface contamination. In addition, this result are more consistent with a surface made of Pt and Cu instead of a Cu overlaer. This XPS analysis, however, is not enough to conclude about the surface structure. For this reason, further studies were carried out on Cu/Pt(111) to understand the effect of CO on the overlayer structure.

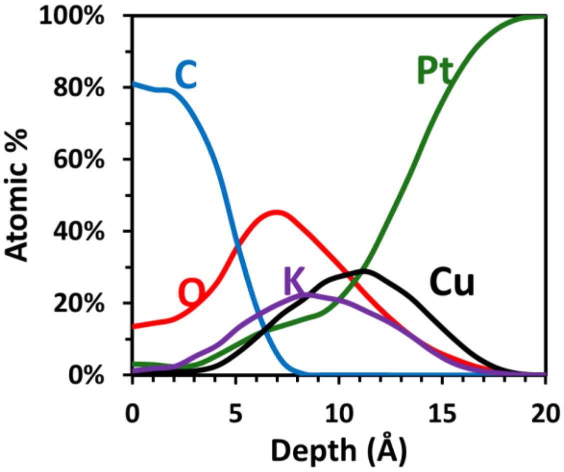

Figure 4.9: Angle resolved X-ray photoelectron spectroscopy for Cu/Pt(111) after 1 hour of bulk CO_2 electrolysis.

4.4 Stability studies in the presence of CO

Ross and co-workers[90, 91] studied the co-adsorption of CO and Cu on Pt (111) by means of rotating ring disc electrode and surface X-ray scattering (SXS). Their results suggest that, close to the Nernst potential for bulk Cu deposition, CO displaces Cu from the Pt surfaces.

4.4.1 CO displacement [92]

With the aim of clarifying if Cu is displaced by CO at lower potentials, we carried out CO displacement on the Cu/Pt(111) at four different potentials (0.0V, 0.1 V 0.22 V and 0.32 V vs. RHE) in 0.1M $HClO_4$. Working at lower potentials than those used in this study is challenging, since the current due to the hydrogen evolution reaction (HER) does not allow a correct determination of the CO displacement current.

The CO displacement experiments were conducted at least two times per selected potential following the procedure described by Clavilier and co-workers. [93] Once the Cu monolayer was the electrolyte was exchanged to N_2 saturated 0.1 M $HClO_4$ under potential control. Afterwards the potential was fixed at a given value while the current was recorded. CO was dosed to the cell trough a gas inlet situated 1 cm away from the meniscus, generating a current response. When the measured current reached a stable value, the CO flux was stopped. Subsequently, the cell was purged with Ar for 20 minutes and the electrolyte was exchanged for a N_2 saturated electrolyte under potential control. Finally, the potential was swept to positive values to electro-oxidize the adsorbed CO.

The current response during CO adsorption is due to the displacement of charged species in the interphase, such as O^{2-}, OH^-, H^+ and Cu^{2+}, either separately or in combination. The displacement of a positively charged species, such as H^+ or Cu^{2+} would give rise to a positive charge while the displacement of an anion like OH^- or O^{2-}

generates a negative charge. The CO displacement on a clean Pt(111) surface at 0.1 V was measured to determinate if the settings were appropriate for these experiments (Figure 4.10). On Pt(111) the CO displacement results in a sharp positive peak with a charge of 92 $\mu C/cm^2$ due to the displacement of *H, in agreement with previous work[93]. On the other hand, when measuring on the Cu/Pt(111) overlayer, broad peaks are observed during the displacement (Figure 4.11).

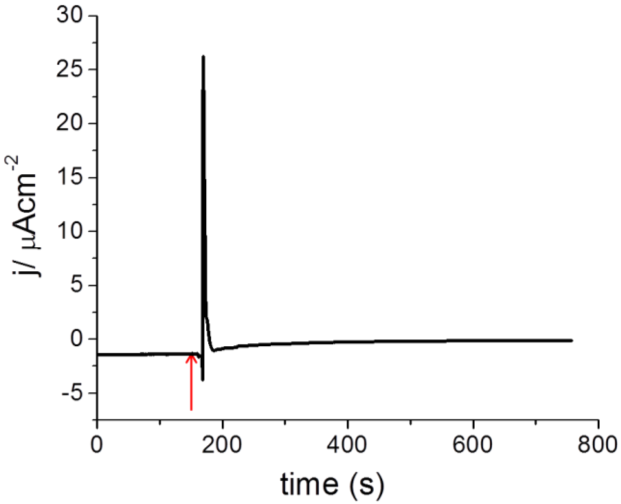

Figure 4.10: Measured current during the CO adsorption on Pt(111) at 0.1 V(RHE) in 0.1M $HClO_4$. The red arrow indicates the time at which CO was dosed into the cell.

The peak shape provides information about the kinetics of the displacement process. The difference in peak shape suggests that, while the displacement of *H by CO on Pt(111) is a fast process, it is not the case for the CO displacement on the Cu/Pt(111). Figure 4.11

shows the current response during the CO displacement on Cu/Pt(111) at different potentials, while Figure 4.12 shows the obtained charge as a function of potential.

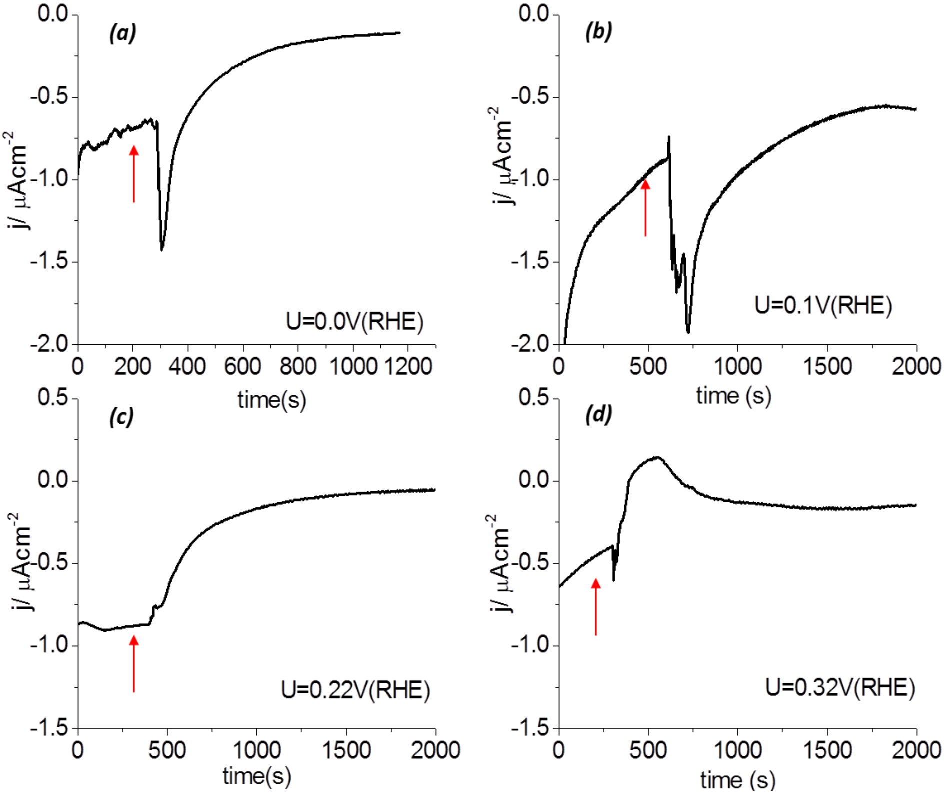

Figure 4.11: Measured current during the CO adsorption on Cu/Pt(111) OL at a fixed potential (*U*=0.0 V (*a*), *U*=0.1 V (*b*) , *U*=0.22 V (*c*) and *U*=0.32V (RHE) (*d*)) In 0.1 M $HClO_{4.}$The red arrow indicates the time at which CO was dosed into the cell.

According to these results the displacement charge is extremely sensitive to the potential at which CO is dosed into the cell, indicating that different species are displaced at different potentials. CO adsorption results in a positive charge when it is adsorbed at sufficiently positive potentials, in this case 0.32 V(RHE). This result is consistent with the displacement of positively charged species, presumably Cu^{2+}. In agreement with Ross and coworkers, this result is a strong indication that at this potential at least part of the copper is displaced by CO[91].

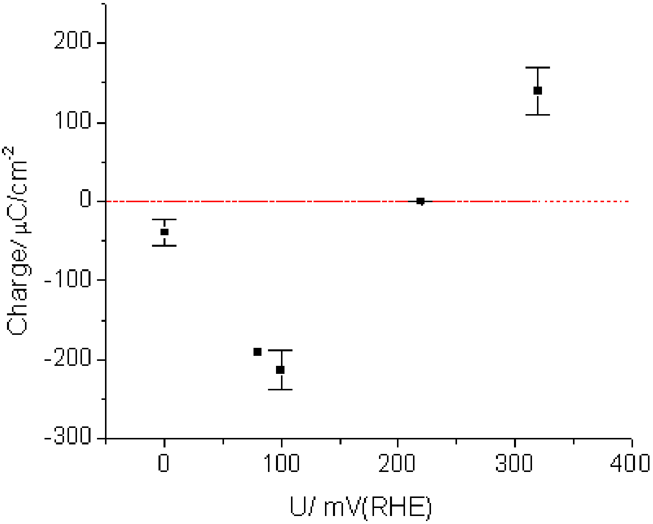

Figure 4.12: Charge generated during the CO displacement on Cu/Pt(111) as a function of the adsorption potential.

The displacement of the copper overlayer by CO was corroborated by sweeping the potential after CO displacement at 0.32 V. The resulting cyclic voltammogram resembles that for the *CO electro-oxidation on Pt(111). Furthermore second cycle is consistent with a Pt(111) and no Cu redeposition is observed. This results indicate that when the CO is adsorbed at 0.32 V, Cu is displaced completely from the surface resulting in a Pt(111) surface covered by CO (Figure 4.12).

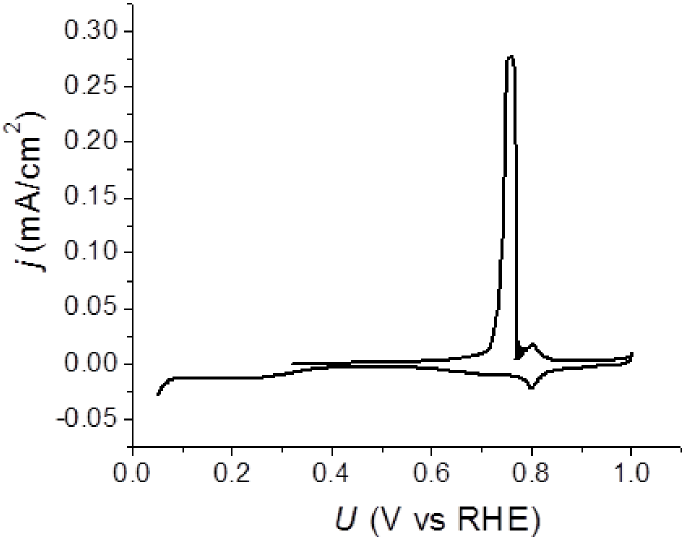

Figure 4.13: *CO stripping voltammogram (dU/dt=20mV/s.) for Cu/Pt(111) after CO displacement at 0.32V(RHE) in Ar saturated 0.1M $HClO_{4.}$

The charge observed during the CO displacement at 0.32Vof 140μC/cm^2, is smaller than 420μC/cm^2 expected for the oxidation of a full Cu monolayer since that charge is not only due to copper displacement. This process is accompanied by *OH and *O displacement that produce a negative charge. The observed charge is the sum of all the displaced species.

In contrast, when the potential is held at 0.1 V and at 0 V (RHE) a negative charge is observed, suggesting the dissolution of negatively charged species, such as OH^- or O^{2-}. The negative charge of 213μC/cm^2 observed during the CO displacement at 0.1 V would correspond to close to one monolayer of *OH or a monolayer of *O, while the coverage predicted by DFT are only 0.3 monolayers for *OH and nearly zero for *O.[54] This discrepancy suggests that the measured charge may not only be attributable to chemisorption but also to dipole rearrangements at the interphase.[94] It is also worth noticing that the charge obtained at 0V is considerable different from that obtained at 0.1V, this could be attributed to the adsorption of *H close to 0V.

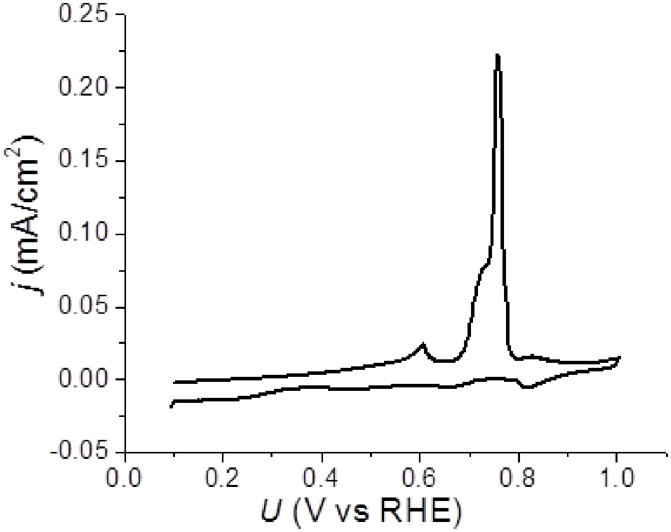

Figure 4.14: *CO stripping voltammogram (dU/dt=20mV/s.) for Cu/Pt(111) after CO displacement at 0.1V in Ar saturated 0.1M $HClO_4$.

The voltammogram for CO electro-oxidation, after CO displacement at 0.1 V was not reproducible, but it was not consistent with either a Cu stripping on Pt(111) or *CO oxidation on Pt (111). In all cases a main oxidation peak was observed at ~0.75V. This peak however was not and it usually had a shoulder ~0.70 as shown in Figure 4.14, or a double peak. The voltammogram on Figure 4.14 also exhibits a small oxidation peak starting at 0.5 V, which was not present in all the strippings.

The features observed on the voltammogram in Figure 4.14 can be studied by Electrochemical Scanning Tunnel Microscopy (EC-STM). Figure 4.15 shows the EC-STM images obtained by Christian Schlaup of Cu/Pt(111) in CO saturated 0.1 M $HClO_4$ while scanning the potential at a scan rate of 20mV/s. It is important to bear in mind that the CV recorded during for the STM image is recoded under CO while the CV recoded after the CO displacement is recorded under Ar.

At low potentials the EC-STM image shows Cu on top of Pt. At around ~600mV there is a transition consistent with the oxidation peak observed at ~550mV in the CVs shown in Figure 4.16*a*. At higher potentials there is no copper on the surfaces, so the small oxidation peak is attributed to Cu dissolution, at a lower potential than the expected for the Cu overlayer. This result is another indication that the Cu is destabilized in the presence of CO. The oxidation feature in Figure 4.16*b*, starting at 800mV, is consistent with oxidation of CO on Pt rather than a Cu related process. Based on these EC-STM results, we attribute the small oxidation peak in Figure 4.13 at ~0.6 V to Cu dissolution. The main oxidation peak stating at ~0.7 V is likely to occur on a Cu free surface and consequently is attributed to CO oxidation.

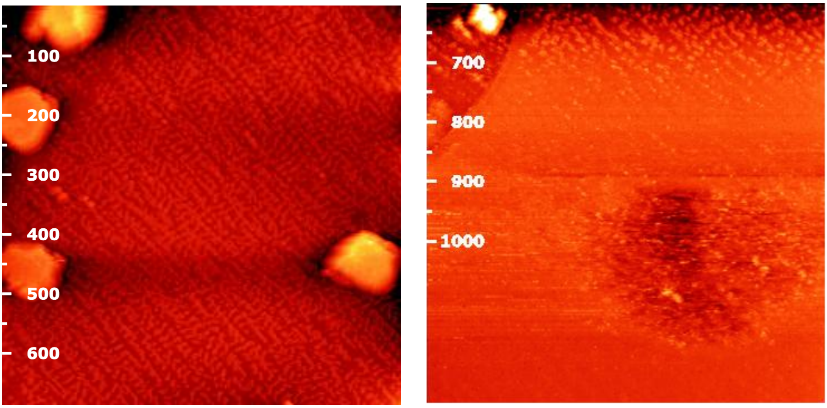

Figure 4.15: EC-STM images of Cu/Pt(111) in CO saturated 0.1M $HClO_4$ (349.20 x349.20 nm) E = -UB = 100 mV, IT = 3 nA., dt/dU= 20mV/s.

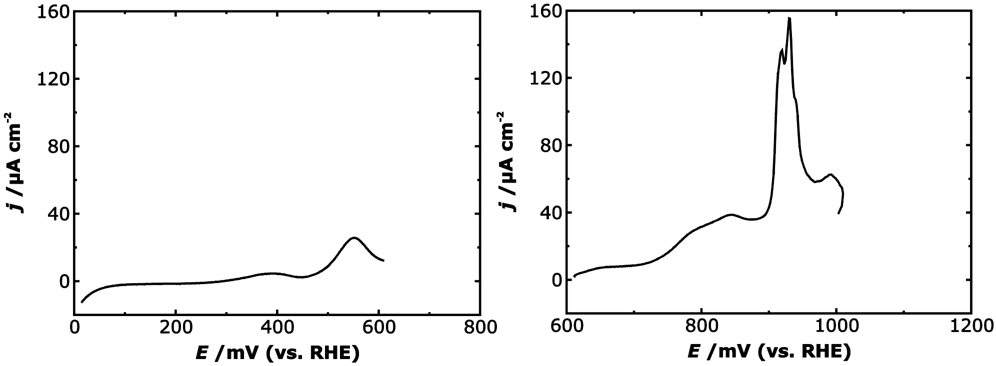

Figure 4.16: Cyclic voltammetry of Cu/Pt(111) in CO saturated 0.1M $HClO_4$, dt/dU= 20mV/s while recording EC-STM images. *a*) from 10mV to 600mV. *b*) from 600 to 1000mV.

When the CO was adsorbed at 0.22 V there is no measurable charge. This indicates that at this potential, CO displaces both positive and negative species, resulting in a net displacement charge of zero. Presumably oxygenated species are displaced together with copper.

In summary, the CO displacement experiments confirmed that at 0.32V the Cu overlayer on Pt(111) is displaced by CO, while copper remains on the surfaces at potential below 0.1 V. These results indicate that copper remains on the surface at the potentials at which the CO_2 electro-reduction takes place. The structure of the overlayer, however, can be affected by the presence of CO which was also investigated by EC STM.

4.4.2 STM studies

EC-STM was also used to study the effect of CO on the structure of the Cu overlayer on Pt(111). Figure 4.17 shows the STM image of Cu/Pt(111) in Ar saturated 0.1M $HClO_4$ at ~260mV vs. RHE. It is important to note that this potential is far away from the potentials at which CO_2 reduction takes place. Recording the images at such negative potentials is challenging due to HER occurring on the studied surface and on the tip. The surface, however, might suffer structural changes during HER. Therefore, the STM images were recorded after cycling the potential to ~-0.4 V. The obtained image shows a smooth surface which is expected to be a pseudomorphic Cu overlayer on Pt(111).

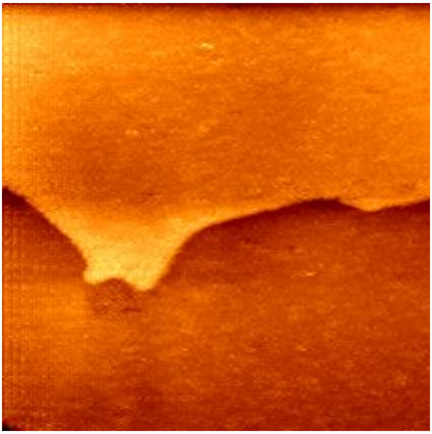

Figure 4.17: EC-STM image of Cu/Pt(111) in Ar saturated 0.1M $HClO_4$ (337.32 nm * 337.32nm UB = 249 mV, IT = 1 nA, E = 203 mV vs. SHE (~260mV vs RHE).

Figure 4.18 shows two STM images of Cu/Pt(111) in CO saturated 0.1M $HClO_4$. In both images it is clear that under these conditions the Cu surfaces changes to a granular structure.

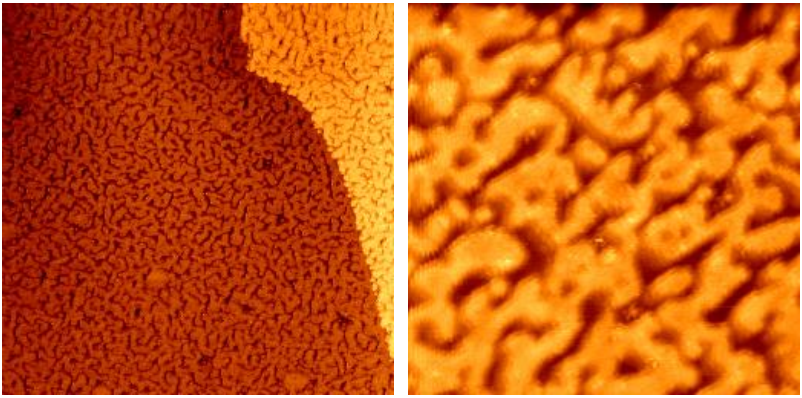

Figure 5.18: EC-STM image of Cu/Pt(111) in CO saturated 0.1M $HClO_4$ *a)* (346.82 nm x346.82 nm) E = 251 mV vs. SHE, UB = 9 mV, IT = 3 nA *b*) (111.49 nm X 111.4nm) E = -39 mV vs. SHE, UB = 102 mV, IT = 1 nA

The high binding energy of Pt-CO favors a reconstruction of the Cu overlayer. In the presence of CO the Cu atoms are pushed together to expose the Pt surface to CO. This is consistent with observations on Pt based nanoparticles in which the presence of CO induces Pt surface segregation. The high binding energy between Pt and CO is the driving force for the transformation of bimetallic particles to core-shell nanoparticles consistent of a Pt outer shell.[52, 89]

From these EC-STM images we can conclude that on Cu/Pt(111) copper remains on the surface when it is exposed to CO at the working potentials. The structure of the overlayer, however, is no longer a pseudomorphic layer on Pt(111) but rather a disordered layer with an interatomic distance between that of pure Cu and pure Pt. The compression of Cu with respect to the Pt lattice constant results in exposure of Pt atoms. Furthermore, in some cases the Cu islands have a height of 2 or 3 atoms, resulting in a higher exposure of the Pt surface.

It is important to bear in mind that these EC-STM were recorded in CO saturated 0.1M $HClO_4$ while the bulk electrolysis experiments were performed in 0.1M $KHCO_3$. Further EC-STM studies will be carried out under $KHCO_3$. The aim of these studies to corroborate that at the CO has the observed reconstruction effect under reaction conditions, and that there is no effect of the electrolyte on the surface structure in the presence of CO.

4.5 Analysis of catalytic results

The structural changes of the Cu/Pt(111) in the presence of CO should be taken in to consideration for the analysis of the catalytic activity of the Cu overlayers on Pt. It is expected that on Cu/Pt (211) CO also induces a reconstruction of the Cu overlayer to expose the Pt surface to CO. Therefore, instead of considering expanded copper overlayers, we need to consider Pt surfaces partially covered by polycrystalline copper.

The high activity towards hydrogen evolution on the Cu/Pt surfaces is due to the exposed Pt atoms that selectively produced hydrogen instead of electro-reducing CO_2. On the other hand, the Cu islands evolve hydrogen and reduce CO_2 to methane, formate and CO. Surprisingly, the ratio between these products is very different than the observed on polycrystalline Cu, suggesting that having Cu on top of Pt is affecting its catalytic activity. As mentioned earlier, it is noteworthy that ethylene is not produced on the Cu overlayers while on polycrystalline coppers it is one of the main products. This could be attributed to having an expanded copper surface in which the protonation of *CO is favored over the C-C coupling. Nevertheless, as previously mention, the discussion of the difference in selectivity of different surfaces is highly speculative since there is no clear mechanism for ethylene formation. Furthermore we also need to have a better understanding of copper islands structure to analyze its reactivity. It is important to now the height of this copper island, the distance between copper atoms and the amount of defects.

Another interesting result is that there is no significant difference in the catalytic activity of Cu/Pt (111) and Cu/Pt(211). This is an indication that the resulting copper islands have a similar structure on Cu/Pt(111) and Cu/Pt(211). It is likely that in both cases they are polycrystalline copper surfaces.

This is a clear example of the importance of *in situ* characterization techniques. Having a good knowledge of the catalyst surface structure under reaction conditions can be crucial for the understanding of the catalyst reactivity, especially when working with bimetallic systems in which surface segregation may occur.

4.6 Conclusions

i. Cu/Pt(111) and Cu/Pt(211) surfaces present catalytic activities in between those of Pt and Cu. The higher catalytic activity of the Cu/Pt structures with respect to pure copper is attributed to a higher activity towards the HER. On the other hand, the activity and selectivity towards methane of these surfaces is considerably lower than on copper.

ii. The presence of CO destabilizes the Cu/Pt(111). At potentials above the Nernst potential, Cu is displaced by CO, while at lower potentials the Cu atoms remain at the surface. The structure of the Cu overlayer, however, changes to a granular structure in the presence of CO, exposing a part of the Pt surface.

iii. The structural changes induced by CO are crucial in understanding the catalytic activity of the Cu/Pt surfaces.

The exposure of the Pt surface accounts for the high activity of these structures towards HER and their poor selectivity towards the reduction of CO_2.

iv. These results illustrate the importance of *in situ* surface characterization to gain an insight into the catalyst surface structure under reaction conditions. As illustrated here, this knowledge can be essential for the understanding of catalyst reactivity.

Chapter 5

5. Preparation of Cu/Pt(111) overlayer, surface alloy and near surface alloy and their electro-catalytic properties.

The electro-catalytic activity of Pt(111) has been tailored by incorporation of monolayer amounts of copper into the first two atomic layers, forming an overlaye (OL), a near-surface alloy (NSA) and a surface alloys (SA) of Cu/Pt. Electrochemical measurements and density functional theory calculations (DFT) agree that the location of the Cu atoms controls the interaction between the surface and different adsorbates. Placing Cu in the first layer strengthens the Pt binding energy towards *H, *OH and *CO, while having subsurface Cu has the opposite effect. This knowledge can be used to tailor the catalytic activity towards a wide range of electro-catalytic reaction as demonstrated here for the CO electro-oxidation. [92]

5.1 Studied surfaces

This chapter focuses on the electrochemical studies on Pt(111) and following modified surfaces of Pt(111)

- A monolayer of copper on of top Pt(111) (**Cu/Pt (111) OL**), where the copper sits on top of the Pt atoms maintaining the lattice parameter of Pt(111) as described in previous chapters.

- Cu/Pt near surface alloy (**Cu/Pt(111)NSA**), on which the copper and platinum are alloyed at subsurface level, however, the outer layer consists only of platinum atoms. This surface, unlike common platinum alloys, retains the lattice constant of platinum; hence the different reactivity between this system and pure platinum is purely an electronic effect, i.e. there is no strain effect.

- Cu/Pt surface alloy (**Cu/Pt(111) SA**) where both Pt and Cu are alloyed at the surface preserving the lattice constant of platinum. As for the Cu/Pt(NSA) the lattice constant of Pt is maintained and thus the reactivity of the Pt surface atoms is only affected by the ligand effect and not by any strain effect. Furthermore, since this surface contains atoms of different nature, it is an interesting system to be study as catalyst for reactions where bifunctionality is needed.

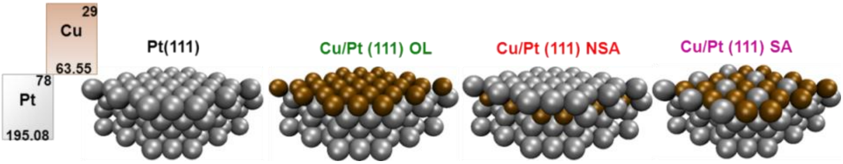

Figure 5.1: Schematic representation of the four studied surfaces

5.1.1 Previous studies

These systems have been well studied under ultra-high vacuum (UHV) [95-98]conditions demonstrating that their properties are clearly different from pure Cu and pure Pt. The presence of copper in the subsurface layers decreases the binding energies between Pt and CO, making the Cu/Pt(111) NSA a promising catalyst for the water/gas shift reaction ($CO + H_2O \rightarrow H_2 + CO_2$) since it prevents CO poisoning[96].

Studies by Andersson *et al[95]* have shown that Cu/Pt(111) NSA is unstable at temperatures above 300°C in the presence of CO forming the Cu/Pt(111) SA. Contraintuitively, CO induces surface segregation of copper, the less reactive component. The previous phenomenon has been explained by a great increase in the strength of the Pt-CO interaction when copper is at the surface in comparison with pure Pt(111). Furthermore, Anderson and co-workers have concluded that the Cu/Pt(111) SA contains 1/3 of a monolayer of Pt and 2/3 of a monolayer of Cu. This structure is consistent with the experimentally observed CO saturation coverage of 1/3 and with the high Pt-CO binding energy calculated when the surface consists of 2/3 of monolayers of Cu.

More recently the Cu/Pt NSA and Cu/Pt SA have been studied under electrochemical conditions by Stephens and co-workers.[83] They have demonstrated that these systems can be prepared at 1 bar and tested in an electrochemical environment. They characterized all the surfaces by cyclic voltammetry between 0.05V and 1.0V (Figure 6.2). On the Cu/Pt(111) SA the Cu dissolution peak is shifted to more anodic potential (~0.85 V) with respect to the Cu/Pt (111) overlayer. The higher potential required to strip the Cu atoms from the surface alloy suggests that copper is stabilized by the Pt atoms.[99] On the Cu/Pt(111) NSA there is no indication of Cu oxidation which indicates that this surface is stable in this potential range. The Pt skin protects the copper atoms from being oxidized.

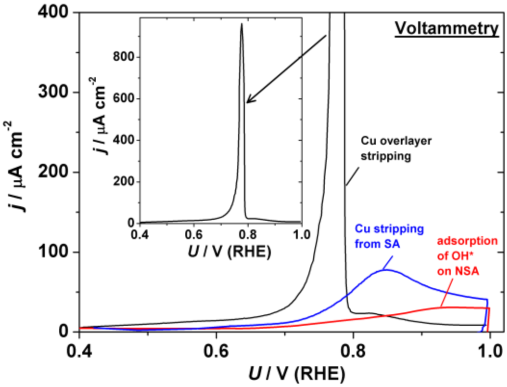

Figure 5.2 Cyclic voltammetry of Cu/Pt(111) OL, Cu/Pt(111) NSA and Cu/Pt(111)SA in Ar saturated 0.1M $HClO_4$ (Figure from [83])

In addition, Stephens and co-workers showed that the binding energy between Pt and OH decreases by having copper in the subsurface layers which has been used to improve the catalytic activity of Pt towards the oxygen reduction reaction (ORR).

5.1.2 Surface preparation

These surfaces were prepared using a Pt(111) single crystal, with a diameter of 5mm oriented to < 0.1° and polished to a surface roughness of 30nm (Mateck, Julich, Germany).The electrochemical cell described in chapter 2 allowed us to anneal the crystal under different atmospheres and prepare the sample, mimicking what has previously been done under high vacuum conditions:

Pt(111): Before experiments, the Pt(111) crystal was annealed at 850±20°C in a H_2(5%)+Ar atmosphere for 5 min, followed by annealing in a CO(1%)+Ar atmosphere for 2 min at 850±20°C. This thermal treatment allows removing impurities from the surfaces as well as reordering of a perturbed surface.

Cu/Pt(111) OL: The Cu/Pt(111) monolayer was prepared by Cu underpotential deposition (UPD) on Pt(111) as described in chapter 4

Cu/Pt(111) NSA: The Cu/Pt(111) NSA was obtained by annealing the Cu/Pt(111) OL during 2 minutes at 400°C in Ar/H_2 atmosphere (5% of H_2 in Ar). Exposing the Cu/Pt(111) OL to H_2 causes the surface segregation of Pt since it is the most reactive component and will form the strongest chemical bond with hydrogen.

Cu/Pt(111) SA: The SA was subsequently obtained by annealing the Cu/Pt(111) NSA for 2 minutes at 400°C in Ar/CO atmosphere (1% of CO in Ar). Analogous to the observations under UHV conditions, exposing the sample to CO causes surface segregation of the less reactive component, copper, forming a surface alloy of Cu and Pt.

After the experiments, the Cu/Pt(111) NSA and the Cu/Pt(111) SA were cycled in 0.1M $HClO_4$ between 0.05V and 1.45V(RHE) for a couple of hours at the scan rate of 50 mV/s. This procedure allows the removal of surface and subsurface Cu, but it also introduces defects to the Pt surface. To restore the Pt (111) surface, the crystals were annealed at 850±20°C in Ar/H_2 and Ar/CO atmosphere. Cyclic voltammetry, X-ray photoelectron spectroscopy (XPS), and low-energy electron diffraction (LEED) and ion scattering spectroscopy (ISS) were used to ensure that the Pt(111) surface was restored and no Cu was present close to the surface.

5.1.3 XPS characterization

The surfaces were characterized using angle resolved XPS[83]. Figure 6.3 shows the surface composition as a function of depth. These results are consistent with the expected structures. On the Cu/Pt(111) OL the surface only contains Cu ,whereas the Pt content increases from 0% at 7Å to 100% when the depth is 20Å.

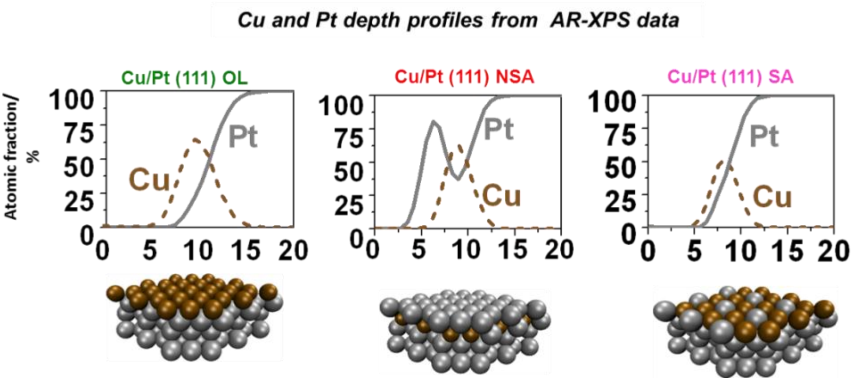

Figure 5.3: Cu and Pt depth profile from angle resolved XPS of Cu/Pt(111) OL, Cu/Pt(111) NSA and Cu/Pt(111)SA.

According to the XPS depth profile, the Cu/Pt(111) NSA clearly has Pt at the surface, furthermore, the copper concentration is zero in the surface and in the bulk, but it has a maximum at around 9Å where the Pt concentration is only 35%. Finally the results for Cu/Pt SA indicate that both Pt and Cu are present in the outer layer.

5.2 Electrochemical characterization

All surfaces were characterized electrochemically by cyclic voltammetry in Ar saturated 0.1M $HClO_4$ (Figure 6.4). Each surface has a very distinct voltammogram suggesting that all of them interact differently with the adsorbates present in solution: *H and *OH.

The CV for Pt (111) from 0.05V to 1.0V shows the characteristic shape of such a surface. The region between 0.05 and 0.4 V corresponds to the adsorption/desorption of *H. The reversible peak due to the adsorption/desorption of *OH is observed at 0.8V with a height of roughly 80µA/cm^2, which is a reasonable value for a clean Pt(111) surfaces.

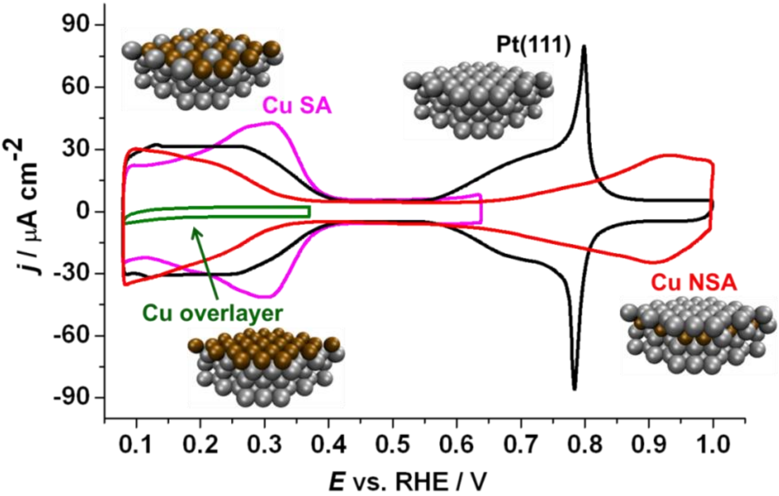

Figure 5.4 Cyclic voltammetry of Pt(111) Cu/Pt(111) OL, Cu/Pt(111) NSA and Cu/Pt(111)SA in Ar saturated 0.1M $HClO_4$

When copper is deposited on the surface the hydrogen region appears featureless. According to the binding energies calculated by Mohammedreza Karamad using DFT DFT, *H is destabilized on the Cu/Pt(111) OL with respect to Pt (111) (Figure 5.5). On the other hand *OH is expected to bind much stronger to Cu/Pt(111) OL than to Pt(111). In fact, based on DFT calculations, we expect that at these potentials the surface is covered with *OH rather than *H. This prediction is corroborated by the CO displacement experiments described in chapter 4.

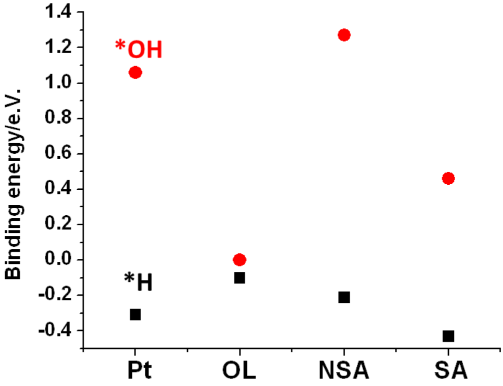

Figure 5.5: Binding energies of *OH, *H on Pt(111), Cu/Pt(111) OL, Cu/Pt(111) NSA and Cu/Pt(111) SA referenced to $H_2O(l)$, $H_2(g)$ respectively.

The CV for the Cu/Pt(111) NSA exhibits the features for both adsorption/desorption of *H and *OH, however, the potentials at which these processes occur differ from those on Pt(111). The hydrogen signal is shifted to less positive potentials suggesting a weaker interaction between *H and the surface. The *OH signal appears ~0.2V more positive than on Pt(111) which is indicative of the destabilization of *OH. These observations are consistent with the binding energies calculated by DFT which predict that *H and *OH bind weaker on Cu/Pt(111) NSA than on Pt(111) (Figure 5.5). According to the DFT calculations on the Cu/Pt (111)NSA, *OH is destabilized by 0.21 e.V. and *H by 0.11e.V. with respect with Pt(111). Marching very well the shifts observed for the Cu/Pt(111) NSA CV with respect to Pt(111).

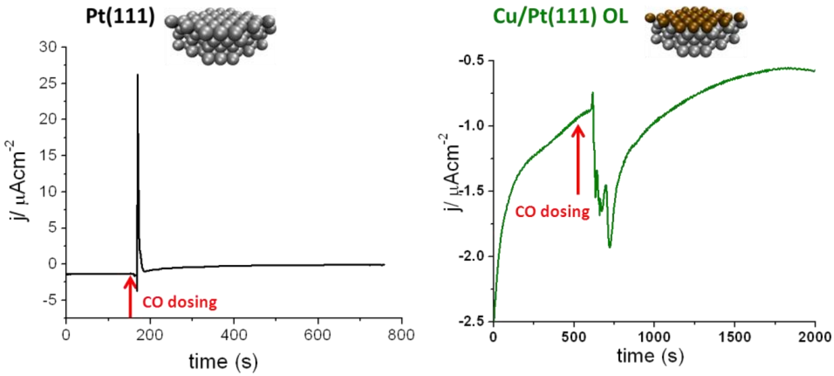

Figure 5.6: CO displacement on Pt(111) and Cu/Pt(111) OL at 0.1mV vs(RHE) 0.1M $HClO_4$

The voltammogram of Cu/Pt(111) SA was recorded from 0.05V to 0.7V to avoid copper dissolution at higher potentials. In this CV we can only appreciate one reversible feature between 0.05 and 0.4V with a maximum at 0.3V. The DFT calculations suggest that this is due to the adsorption/desorption of *OH on the Cu sites and *H on the Pt sites. DFT predicts that *OH binds the SA 0.6 e.V. stronger than Pt(111), in good agreement with the ~0.5 V shift between the peak on the SA and that of OH adsorption on Pt(111) and that *H will bind to Pt 0.1 e.V. stronger than on Pt(111).

5.3 CO electro-oxidation

The electrochemical measurements confirm that the trends observed previously for the gas-phase adsorption of *CO also persist for the electrochemical adsorption of *H and *OH. Furthermore, these observations are consistent with similar investigations by others[100, 101], there is a linear correlation between the binding energies of *CO and *H.

These experimental results are consistent with DFT calculations that indicate that placing Cu in the first layer strengthens the Pt binding energy towards *H, *OH, and *CO, while having subsurface Cu weakens the interaction.

As stated in the Sabatier principle[30, 33], the binding energy between a surface and the key intermediate of a reaction is what determines how good a catalyst works. Since,*H, *OH, and *CO are common intermediates in electrochemistry, it is possible to tailor the catalytic activity of the Cu/Pt(111) towards different electrochemical reactions by controlling the location of the copper atoms.

Herein, the CO adlayer electro-oxidation is used as test reaction[85] to demonstrate how the catalytic activity the of Cu/Pt(111) is modified by changing its atomic structure. This is a fairly simple reaction,[102, 103] involving two charge transfer steps and two adsorbates on the surface, according to the following mechanism.

$$CO(g) + * \rightarrow CO^{*}$$

$$H_2O(l) + {}^{*} \rightarrow OH^{**} + H^{+}(aq) + e^{-}$$

$$OH^{**} + CO^{*} \rightarrow CO_2 + H^{+}(aq) + e^{-} + * + **$$

Assuming the above mechanism, the electrochemical oxidation of CO involves the formation of *CO and *OH. Therefore, the optimal catalyst for the reaction must have an intermediate binding energy towards both *CO and *OH. Unfurtunately, finding the right catalyst is not strait forward since there is no direct scaling relation between these two adsorbates. This means that the surface with an optimal reactivity towards CO does not necessary has to have an apropiate reactivity towards OH. A good way to circumvent this challenge is by using bifuctional[104, 105] catalysts in which the presence of two different active sites facilitates having an optimal reactivity towards the two key adsorbates. Since Pt is reactive towards carbon and Cu is reactive towards oxygen the Cu/Pt(111) SA represents an interesting candidate as catalyst for the electrochemical oxidation of CO.

5.3.1 Electrochemical measurements

We tested the different surfaces as catalyst for *CO adlayer oxidation, also known as CO stripping. The CO was pre-adsorbed on to the surface by holding the potential at 0.05V during 15 minutes in CO saturated 0.1M $HClO_4$. Afterwards the electrolyte was exchange to Ar purged 0.1M $HClO_4$ and the potential was increased to 1.0V at scan rate of 20mV/s.

Figure 6.7 shows the obtained curves for the CO stripping of the Pt(111), the Cu/Pt(111) SA and Cu/Pt(111) NSA. On these voltammograms there is no current observed below 0.4V since the adsorbed CO blocking the Pt surface atoms. The oxidation peak appearing after 0.4V is attributed to the oxidation of *CO to CO_2, however, this process may also be accompanied by OH adsorption.

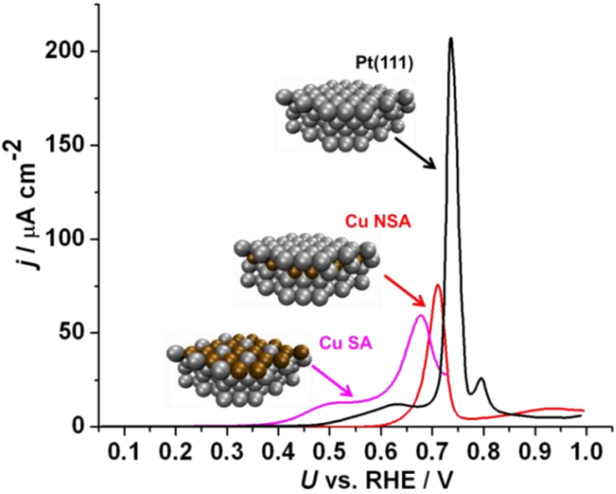

Figure 6.7: *CO stripping voltammograms for Pt(111), Cu/Pt(111) SA, and Cu/Pt(111) NSA, in $HClO_4$, dU/dt = 20 mV/s. The CO was adsorbed at 0.05 V, whereas the voltammogram was carried out in CO-free solution.

The observed areas of the CO electro-oxidation peaks, are proportional to the charge used to oxidize *CO. It can be used to estimate the CO coverage of each surface assuming that the CO oxidation is a two electron process, and that the number of Pt surface atoms on Pt(111) is 1.5 × 10^{15} atoms/cm^2. (Equation5.1)

$$coverage = \frac{Q}{(2e)(1.5\times10^{15})} \quad Eq.\ 5.1$$

For Pt(111) the charge of 328 μCcm^{-2} corresponds to a coverage of 0.68 monolayers (ML) in agreement with values known in literature. In contrast, the charge of 164μCcm^{-2} on the NSA corresponds to a coverage of 0.34 ML. On the surface alloy the *CO oxidation is accompanied by *OH adsorption and Cu dissolution (which starts above 0.7 V). This makes the determination of the *CO equilibrium coverage challenging since the charge cannot only be attributed to CO oxidation. Nevertheless it is possible to estimate it by DFT based on the integral and differential free energies of adsorption.[106] The integral energy is the total adsorption energy of all adsorbed CO molecules on the surface (relative to CO in the gas phase) per surface metal atom. It can also be calculated as the product between the average free energy and the CO coverage. The differential free energy of adsorption is calculated by differentiating the integral free energy with respect to CO coverage. (Equation5.2)

$$G_{diff}\ \theta \ = \frac{dG_{int}}{d(\theta)} = \frac{dG_{avg\theta}}{d(\theta)} \ Eq\ 5.2$$

Figure 5.8 shows the average and differential free energy of adsorption a for the Cu/Pt(111) SA, Cu/Pt(111) NSA and Pt(111) as a function of CO coverage.

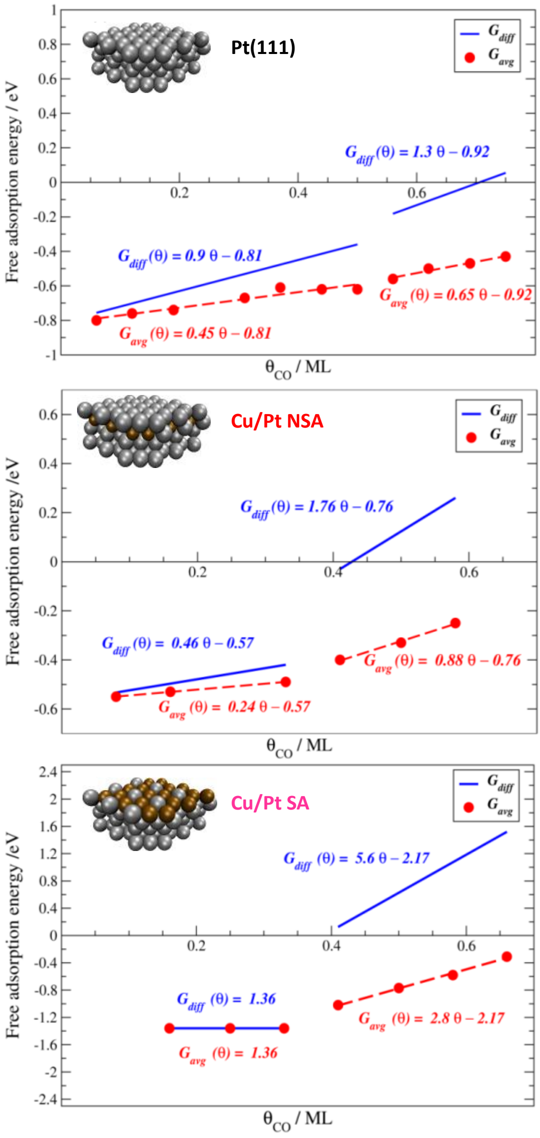

Figura 6.8: Free energy of adsorption of CO on Pt(111), Cu/Pt(111) NSA and Cu/Pt (111) SA The red points are the calculated average adsorption energy at different coverages of CO and the red dashed lines are the fit to them at different coverage regimes. The blue lines represent the differential free energy

At low CO coverages on Cu/Pt(111) SA the value of -1.4 eV for the free energy of adsorption indicates that the adsorption of an extra molecule of CO is energetically favoured. Nevertheless when the coverage reaches 0.33ML there is sharp change in CO differential free energy of adsorption, suggesting that for higher coverages the adsorption of CO is suppressed, thus the equilibrium CO coverage should be 0.33ML

The free energy of adsorption for the Cu/Pt(111) NSA presents a similar behaviour as for the Cu/Pt(111) SA. At coverage of 0.33ML there is also a sharp change in CO differential free energy of adsorption suggesting that the CO coverage is also 1/3 of a ML.

The lower *CO equilibrium coverage on the Cu/Pt(111) SA with respect to Pt(111) responds to a different surface composition.A coverage of 1/3 of a ML on the SA is consistent with a CO molecule covering each platinum surface atom as it was observed in UHV conditions. A higher coverage would imply that some of the CO molecules sit on top of Cu which is not energetically favoured. On the other hand, the difference in *CO coverage between the NSA and the Pt(111) can only be attributed to modified electronic properties of the Pt surface atoms, since both consist of pure Pt in the outer layer.

It is interesting to compare the Cu/Pt(111) NSA with $Pt_3Ni(111)$ and $Pt_3Co(111)$, both of which also have first layers of pure Pt.[107] On these bulk alloys, the coverage of *CO approximates to that of

Pt(111). This is clearly not the case for the NSA, suggesting that the CO electro-oxidation charge may not always provide a one-to-one correlation with the surface area of nanocatalysts with a Pt overlayer.

While the area of the oxidation peak provides information about the *CO equilibrium coverage, the position of the peak is related to the overpotential needed for the CO electro-oxidation.[107] The less positive the potential for the *CO oxidation the better is the surface as catalyst. According to the position of the main oxidation peak, observed in Figure 5.7, the potential required to oxidize CO increases in the following order: SA < NSA < Pt(111).

We focus on the position on the main peak and not in the onset for the oxidation current, since for Pt(111) it has been established that this peak corresponds to the reaction of terrace bound *CO and *OH[87, 108]. On the other hand, the pre-peak starting at ~0.5V is due to CO oxidation facilitated by the surface defects. The effect of the defects on the position of the main peak would be related to the decrease in total coverage of *CO, relative to the saturation coverage, that occurs during the pre-peak. If we were to assume that the CO is immobile, and that *OH nucleates and grows from the step, the local coverage of *CO would be high at the sites where the reaction takes place. On the other hand, if we were to assume that the CO is highly mobile,[109] then the local coverage of *CO would be slightly lower than the saturation coverage, due to the amount oxidized in the pre-peak.

We do not know what exact form the defects would take on the studied alloy surfaces. Nonetheless we anticipate that analogous to Pt(111) the pre-peak observed on the Cu/Pt SA (111) starting at ~0.4 V is also due to defects. In the case of the NSA, there is only a single stripping peak starting ~0.6 V and reaching a maximum at ~0.7 V. This absence of a pre-peak is consistent with the notion that the oxidation only occurs at one site, presumably the terrace, and that the role of defects may be less important.

5.3.2 Volcano plot for CO-adlayer electro-oxidation

Based on the Sabatier principle and on the CO electro-oxidation mechanism discuss previously, we know that the optimal catalyst must have an intermediate binding energy towards both *CO and *OH. On one hand, it has to bind CO(g) and activate water and form *OH and in the other hand it has to bind CO and OH weakly enough to form CO_2 and let it desorbed from the surface.

Therefore, the activity of a surface towards the CO electro-oxidation can be described as a function of the free energies for adsorption of *CO and *OH as shown in Figure 6.9. On this volcano the activity towards the *CO oxidation is given in terms of over potential, the most active catalyst will be that one where the overpotential is closest to cero. The theoretical over potential corresponds to the potential at which all the reaction steps are downhill in free energy. It is calculated without taking into account the kinetic barriers and assuming that the activation barrier for each electron-proton transfer step is proportional to the corresponding free energy change. Therefore the predicted overpotential should not be interpreted as an absolute value but as relative value that can be used to predict activity trends.

The volcano in figure 6.9 has two different regions divided by a red dashed line that indicates the chemical potential of CO in the gas phase, above this value (region in yellow) CO does not bind to the surface. Therefore, all surfaces in this region cannot be used as catalyst for the CO electrochemical oxidation. For example, on the volcano we observe a blue dot that corresponds to Cu(111), the overpotential of CO electrochemical oxidation is predicted to be low on this surface, unfortunately, CO will not bind to copper and the reaction cannot take place.

The rate limiting step for the CO electrochemical oxidation depends on free energies of adsorption of *CO and *OH. As it can be seen in figure 6.8 if the CO binds weakly to the surface the rate limiting step is the adsorption of CO onto the surface (CO(g) + * → *CO). If OH binds weakly then the rate limiting step is the activation of water to form *OH (H_2O(l) + ** →**OH + H^+(aq) + e^-). Finally, if the surface binds strongly to both *OH and *CO then the reaction is limited by the desoption of CO_2 (OH^{**} + CO^{*} → *CO_2 + H^+(aq) + e^- + * + **) In all cases the rate limiting step is the activation of water.

Figure 5.9 shows the predicted overpotential for the studied surfaces according to the free energies of adsorption of *OH and *CO at the equilibrium coverages.

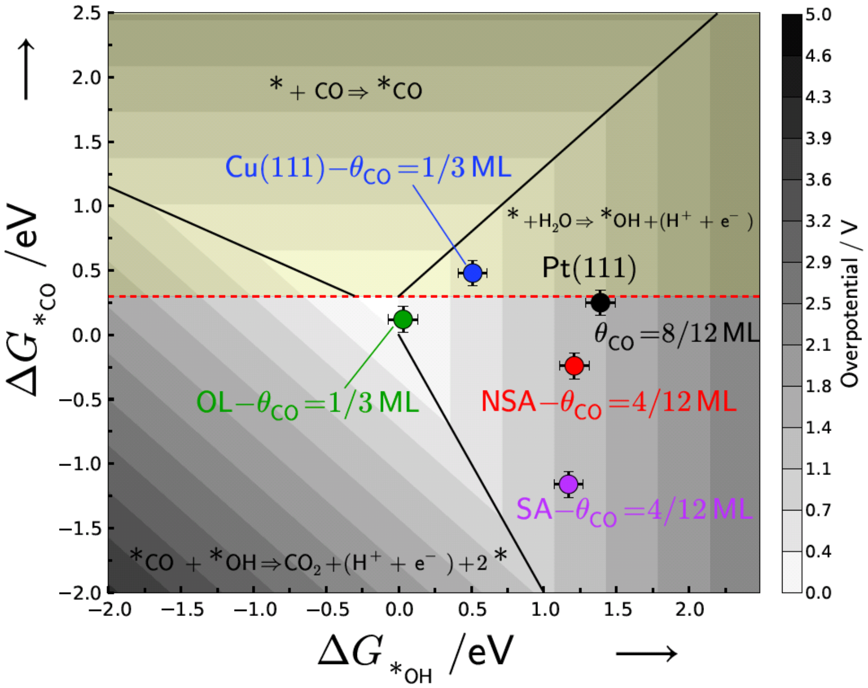

Figure 5.9: Volcano plot for CO electro-oxidation against the free energies of adsorption of CO and OH on Pt(111), Cu(111), Cu/Pt(111) NSA, Cu/Pt(111) SA and Cu/Pt(111) OL. The coverage of CO is depicted for each surface. The potential determining step for each region is also defined. The dashed horizontal line denotes the chemical potential of CO in the gas phase.

In agreement with our experiments, the overpotential required to oxidize CO increases in the following order: SA<NSA<Pt(111). The SA exhibits a lower overpotential for CO oxidation by virtue of its bifunctional nature: *OH binds to Cu sites and *CO binds to Pt.

The volcano also suggests that the Cu/Pt(111) OL should exhibit optimal activity for *CO electro-oxidation. However, this theoretical prediction could not be realized. As it has been discussed in chapter 5 the Cu/Pt(111) OL is not stable in the presence of CO. Based on the CO displacement experiments (Figure 5.2) we concluded that at potentials above 0.1V copper overlayer is at least partially dissolved in the presence of CO due to a strong Pt-CO binding. Furthermore, if CO is adsorbed at sufficiently positive potentials (0.32V vs. RHE) all copper is displaced and further CO oxidation takes place on a clean Pt(111). This illustrates that optimal binding to the intermediates is a necessary but insufficient criterion for an effective catalyst: It must also be stable.

To model the effect of the change in coverage during the course of the voltammogram and to understand the role of defects on the position of the main oxidation peak, we have also included on the volcano plot the predicted overpotential when the *CO coverage is 1/12 of a monolayer lower than the equilibrium coverage (Figure 6.10). The same trends persist at both coverages, i.e. the overpotential for the reaction increases in the following order: Cu/Pt(111) SA < Cu/Pt(111) NSA < Pt(111).

For all structures, the activity towards *CO electro-oxidation is slightly improved when the *CO coverage is lower, meaning that when *CO starts to be oxidized the reaction becomes more favourable. Furthermore, Figure 6.10 shows that that by lowering the *CO coverage on the Cu/Pt(111) SA, the limiting step changes from the *OH adsorption to CO_2 desorption, since at a lower *CO coverages there are more available sites where *OH binds more strongly facilitating the activation of water.

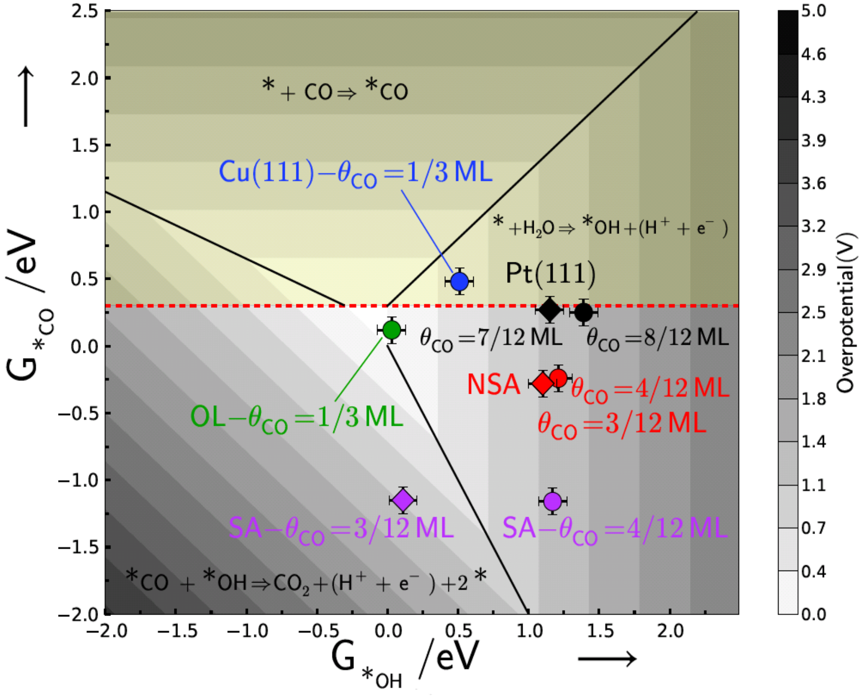

Figure 5.10: Volcano plot for CO electro-oxidation against the free energies of adsorption of CO and OH on Pt(111), Cu(111), Cu/Pt(111) NSA, Cu/Pt(111) SA and Cu/Pt(111) OL . Inlcudes the theoretical overpotential at *CO equilibrium coverages and at *CO coverage 1/12 of a monolayer lower than the most stable coverage.

As discussed previously the effect of the defects would be to decrease the total *CO coverage on these surfaces at the onset of the main peak, where terrace bound *CO and *OH react. However the previous volcano illustrates that the catalytic activity is only slightly sensitive to the *CO coverage for the surfaces under study. At both saturation coverages and slightly lower coverages of *CO, the theoretical model is able to describe the experimental data, where the overpotential increases in the following order: SA < NSA < Pt(111).

5.4 Conclusion

i. By controlling the surface composition atom-by-atom, we have achieved unprecedented degree of agreement between electrochemical experiments and first-principles calculations. This shows that DFT calculations are a useful tool for the understanding of electrochemical reactions.
ii. The Cu location in Pt(111) controls its interaction between the surface and different adsorbates. Placing Cu in the first layer like in Cu/Pt SA (111) strengthens the Pt binding energy towards *H, *OH, and *CO. Having subsurface Cu, as in Cu/Pt (111) NSA has the opposite effect, i.e. it weakens the interaction between Pt at *H, *OH and *CO.
iii. The relationship between the position of Cu and the reactivity of the surface can be used to tailor the electrocatalytc activity of Cu/Pt (111), as demonstrated here for the CO adlayer oxidation. Electrochemical measurements and DFT calculations agree that potential required to oxidize CO increases in the following order: SA < NSA < Pt(111).
iv. In addition, DFT predicts that Cu/Pt (111) OL has the optimal biding energies for CO electro-oxidation. This theoretical prediction, however, was not verified since this surface is not

stable under reaction conditions. This illustrates that the optimal binding energy is not the only requirement for the ideal catalyst. It must also be stable.

v. The approached described for this research can be used to design an optimal catalyst towards many electrochemical reactions, since *H, *OH, and *CO are key intermediates of a variety of processes.

Chapter 6

6. Summary

- The studies on polycrystalline copper showed that the efficiency and selectivity towards CO_2 electro-reduction are sensitive to copper's surface morphology. Rough surfaces are more active and selective towards CO_2 reduction over hydrogen evolution. In particular, rough surfaces have a high selectivity for ethylene production.
- The different catalytic activity between rough and smooth surfaces is partially explained by a higher local pH on rough surfaces, that suppresses hydrogen and methane formation. In addition, surface morphology effects can also be attributed to the different facets present in each system. Smooth surfaces contain predominately low index facets such as (111) and (100), while roughened surfaces have a greater number of steps and kinks. DFT calculations have suggested that uncoordinated sites, simulated using a (211) surface, are more active towards HER and CO_2 reduction. However, more modeling is required to determine the effect different surface sites have on the activity and to understand how to control the selectivity between ethylene and methane.
- The research on Cu/Pt(111) and Cu/Pt(211) indicates that these structures have different catalytic activities than pure Cu

and pure Pt. Cu overlayers present intermediate activities between Pt and Cu. Their selectivity towards hydrocarbons, however, is considerably lower than that on pure Cu. This low hydrocarbon selectivity is attributed to a reconstruction of the copper overlayers in the presence of CO, which is an intermediate for the reduction of CO_2 to hydrocarbons. EC-STM images showed that in a CO-saturated electrolyte the Cu overlayer changes to a granular structure. The high CO binding energy on CO causes the Cu atoms to be pushed together exposing the Pt surface. The exposure of the Pt surface accounts for the high activity of these structures towards HER and their low selectivity towards hydrocarbon production.

- Finally, the work on Cu/Pt(111), overlayer (OL), surface alloy (SA) and near surface alloy (NSA) showed that the location of the Cu atoms determinates the reactivity of the Pt. When Cu is located in the subsurface layers like in Cu/Pt(111) NSA, Pt becomes less reactive towards *OH, *H and *CO. On the other hand, Cu located on the surface increases the reactivity of Pt. This knowledge can be used for tailoring the catalytic activity of Pt, as demonstrated here for CO electro-reduction. Electrochemical measurements and DFT calculations agree that the potential required to oxidize CO increases in the following order: SA < NSA < Pt(111).

Chapter 7

7. Outlook

The results on the Cu overlayers on Pt suggest that bimetallic systems containing Pt are not good candidates as catalysts for CO_2 electro-reduction. The high Pt-CO binding energy would likely cause Pt segregation. Furthermore, the presence of Pt on the surfaces would favor the HER over the CO_2 reduction.

For this reason, future experiments in CO_2 reduction will focus on materials with low binding energy towards CO. For example gold or silver alloys and metallic overlayers on gold. Gold and silver have a low binding energy towards CO suggesting that CO is not likely to induce surface reconstruction. Additionally, both metals are less active than Pt towards HER, therefore it is expected that gold and silver are not highly selective towards HER.

Electrochemical measurements accompanied of a chromatographic analysis of the reaction products will provide information of the catalytic activity of these materials. This studies should be accompanied of surface characterization, in this case EC-STM, to determinate the stability of the system under reaction conditions.

8. References

1. BP, *Statistical Review of World Energy June 2012*. 2012.
2. European commission, Energy 2020, 2011 (http://ec.europa.eu/energy/strategies)
3. Danish Ministry of Climate Energy and Building, Energy Policy Report 2012
4. Armaroli, N. and V. Balzani, *Towards an electricity-powered world.* Energy & Environmental Science, 2011. **4**(9): p. 3193-3222.
5. Eberle, D.U. and D.R. von Helmolt, *Sustainable transportation based on electric vehicle concepts: a brief overview.* Energy & Environmental Science, 2010. **3**(6): p. 689-699.
6. Gattrell, M., N. Gupta, and A. Co, *Electrochemical reduction of CO2 to hydrocarbons to store renewable electrical energy and upgrade biogas.* Energy Conversion and Management, 2007. **48**(4): p. 1255-1265.
7. Turner, J.W.G., et al., *Extending the role of alcohols as transport fuels using iso-stoichiometric ternary blends of gasoline, ethanol and methanol.* Applied Energy, 2013. **102**(0): p. 72-86.
8. Wilicox, J., *The Role of CO2 Reduction Catalysis in Carbon CaptureProf. Jennifer Wilcox*, in *Carbon capture*, Springer, Editor. 2012. p. 245-256.

9. Hori, Y., *Electrochemical CO2 Reduction on Metal Electrodes*, in *Modern Aspects of Electrochemistry*, C. Vayenas, R. White, and M. Gamboa-Aldeco, Editors. 2008, Springer New York. p. 89-189.
10. Benson, E.E., et al., *Electrocatalytic and homogeneous approaches to conversion of CO2 to liquid fuels.* Chemical Society Reviews, 2009. **38**(1): p. 89-99.
11. Gattrell, M., N. Gupta, and A. Co, *A review of the aqueous electrochemical reduction of CO2 to hydrocarbons at copper.* Journal of Electroanalytical Chemistry, 2006. **594**(1): p. 1-19.
12. Hori, Y., K. Kikuchi, and S. Suzuki, *PRODUCTION OF CO AND* CH_4 *IN ELECTROCHEMICAL REDUCTION OF* CO_2 *AT METAL ELECTRODES IN AQUEOUS HYDROGENCARBONATE SOLUTION.* Chemistry Letters, 1985. **14**(11): p. 1695-1698.
13. Hori, Y., et al., *Selective Formation of C2 Compounds from Electrochemical Reduction of CO2 at a Series of Copper Single

Crystal Electrodes. The Journal of Physical Chemistry B, 2001. **106**(1): p. 15-17.

14. Hori, Y., A. Murata, and R. Takahashi, *Formation of hydrocarbons in the electrochemical reduction of carbon dioxide at a copper electrode in aqueous solution.* Journal of the Chemical Society, Faraday Transactions 1: Physical Chemistry in Condensed Phases, 1989. **85**(8): p. 2309-2326.
15. Kuhl, K.P., et al., *New insights into the electrochemical reduction of carbon dioxide on metallic copper surfaces.* Energy & Environmental Science, 2012. **5**(5): p. 7050-7059.
16. Schouten, K.J.P., et al., *A new mechanism for the selectivity to C1 and C2 species in the electrochemical reduction of carbon dioxide on copper electrodes.* Chemical Science, 2011. **2**(10): p. 1902-1909.
17. Terunuma, Y., A. Saitoh, and Y. Momose, *Relationship between hydrocarbon production in the electrochemical reduction of CO2 and the characteristics of the Cu electrode.* Journal of Electroanalytical Chemistry, 1997. **434**(1–2): p. 69-75.
18. Hori, Y., et al., *Electroreduction of carbon monoxide to methane and ethylene at a copper electrode in aqueous solutions at ambient temperature and pressure.* Journal of the American Chemical Society, 1987. **109**(16): p. 5022-5023.
19. Gonçalves, M.R., et al., *Selective electrochemical conversion of CO2 to C2 hydrocarbons.* Energy Conversion and Management, 2010. **51**(1): p. 30-32.
20. Wasmus, S., E. Cattaneo, and W. Vielstich, *Reduction of carbon dioxide to methane and ethene—an on-line MS study with rotating electrodes.* Electrochimica Acta, 1990. **35**(4): p. 771-775.
21. Schouten, K.J.P., et al., *Two Pathways for the Formation of Ethylene in CO Reduction on Single-Crystal Copper Electrodes.* Journal of the American Chemical Society, 2012. **134**(24): p. 9864-9867.
22. Li, C.W. and M.W. Kanan, *CO2 Reduction at Low Overpotential on Cu Electrodes Resulting from the Reduction of Thick Cu2O Films.* Journal of the American Chemical Society, 2012. **134**(17): p. 7231-7234.
23. Peterson, A.A., et al., *How copper catalyzes the electroreduction of carbon dioxide into hydrocarbon fuels.* Energy & Environmental Science, 2010. **3**(9): p. 1311-1315.
24. Hori, Y., et al., *Electrochemical Reduction of CO at a Copper Electrode.* The Journal of Physical Chemistry B, 1997. **101**(36): p. 7075-7081.

25. Stephens, I.E.L., et al., *Understanding the electrocatalysis of oxygen reduction on platinum and its alloys.* Energy & Environmental Science, 2012. **5**(5): p. 6744-6762.
26. Nørskov, J.K., et al., *Origin of the Overpotential for Oxygen Reduction at a Fuel-Cell Cathode.* The Journal of Physical Chemistry B, 2004. **108**(46): p. 17886-17892.
27. Nie, X., et al., *Selectivity of CO2 Reduction on Copper Electrodes: The Role of the Kinetics of Elementary Steps.* Angewandte Chemie International Edition, 2013. **52**(9): p. 2459-2462.
28. Montoya, J.H., A.A. Peterson, and J.K. Nørskov, *Insights into C□C Coupling in CO2 Electroreduction on Copper Electrodes.* ChemCatChem, 2013. **5**(3): p. 737-742.
29. Chorkendorff, I. and N. J.W., *Concepts of Modern Catalysis and Kinetic*. 2003: WIley-VCH.
30. Bligaard, T., et al., *The Brønsted–Evans–Polanyi relation and the volcano curve in heterogeneous catalysis.* Journal of Catalysis, 2004. **224**(1): p. 206-217.
31. Ferrin, P., et al., *Reactivity descriptors for direct methanol fuel cell anode catalysts.* Surface Science, 2008. **602**(21): p. 3424-3431.
32. Falsig, H., et al., *Trends in the Catalytic CO Oxidation Activity of Nanoparticles.* Angewandte Chemie, 2008. **120**(26): p. 4913-4917.
33. Norskov, J.K., et al., *Towards the computational design of solid catalysts.* Nature Chemistry, 2009. **1**(1): p. 37-46.
34. Laursen, A.B., et al., *Electrochemical Hydrogen Evolution: Sabatier's Principle and the Volcano Plot.* Journal of Chemical Education, 2012. **89**(12): p. 1595-1599.
35. Bligaard, T. and J.K. Nørskov, *Ligand effects in heterogeneous catalysis and electrochemistry.* Electrochimica Acta, 2007. **52**(18): p. 5512-5516.
36. Hammer, B. and J.K. Nørskov, *Electronic factors determining the reactivity of metal surfaces.* Surface Science, 1995. **343**(3): p. 211-220.
37. Mavrikakis, M., B. Hammer, and J.K. Nørskov, *Effect of Strain on the Reactivity of Metal Surfaces.* Physical Review Letters, 1998. **81**(13): p. 2819-2822.
38. Chen, J.G., C.A. Menning, and M.B. Zellner, *Monolayer bimetallic surfaces: Experimental and theoretical studies of trends in electronic and chemical properties.* Surface Science Reports, 2008. **63**(5): p. 201-254.

39. Hoster, H.E., O.B. Alves, and M.T.M. Koper, *Tuning Adsorption via Strain and Vertical Ligand Effects.* ChemPhysChem, 2010. **11**(7): p. 1518-1524.
40. Greeley, J., et al., *Hydrogen Evolution Over Bimetallic Systems: Understanding the Trends.* ChemPhysChem, 2006. **7**(5): p. 1032-1035.
41. Esposito, D.V., et al., *Low-Cost Hydrogen-Evolution Catalysts Based on Monolayer Platinum on Tungsten Monocarbide Substrates.* Angewandte Chemie International Edition, 2010. **49**(51): p. 9859-9862.
42. Strasser, P., et al., *Lattice-strain control of the activity in dealloyed core-shell fuel cell catalysts.* Nature Chemistry, 2010. **2**(6): p. 454-460.
43. Wang, J.X., et al., *Oxygen Reduction on Well-Defined Core−Shell Nanocatalysts: Particle Size, Facet, and Pt Shell Thickness Effects.* Journal of the American Chemical Society, 2009. **131**(47): p. 17298-17302.
44. Kleiman-Shwarsctein, A., et al., *A general route for RuO2 deposition on metal oxides from RuO4.* Chemical Communications, 2012. **48**(7): p. 967-969.
45. Sasaki, K., et al., *Carbon-Supported IrNi Core–Shell Nanoparticles: Synthesis, Characterization, and Catalytic Activity.* The Journal of Physical Chemistry C, 2011. **115**(20): p. 9894-9902.
46. Heggen, M., et al., *Formation and Analysis of Core–Shell Fine Structures in Pt Bimetallic Nanoparticle Fuel Cell Electrocatalysts.* The Journal of Physical Chemistry C, 2012. **116**(36): p. 19073-19083.
47. Price, S.W.T., et al., *Exploring the First Steps in Core–Shell Electrocatalyst Preparation: In Situ Characterization of the Underpotential Deposition of Cu on Supported Au Nanoparticles.* Journal of the American Chemical Society, 2011. **133**(48): p. 19448-19458.
48. Huang, M., et al., *In depth analysis of complex interfacial processes: in situ electrochemical characterization of deposition of atomic layers of Cu, Pb and Te on Pd electrodes.* RSC Advances, 2012. **2**(29): p. 10994-11006.
49. Schlaup, C. and S. Horch, *In-situ STM study of phosphate adsorption on Cu(111), Au(111) and Cu/Au(111) electrodes.* Surface Science, 2013. **608**(0): p. 44-54.
50. Friebel, D., et al., *Balance of Nanostructure and Bimetallic Interactions in Pt Model Fuel Cell Catalysts: In Situ XAS and DFT*

Study. Journal of the American Chemical Society, 2012. **134**(23): p. 9664-9671.

51. Abrams, B.L., et al., *Dynamics of Surface Exchange Reactions Between Au and Pt for HER and HOR.* Journal of The Electrochemical Society, 2009. **156**(2): p. B273-B282.
52. Mayrhofer, K.J.J., et al., *Adsorbate-Induced Surface Segregation for Core–Shell Nanocatalysts.* Angewandte Chemie International Edition, 2009. **48**(19): p. 3529-3531.
53. Kobayashi, H., et al., *Atomic-Level Pd−Pt Alloying and Largely Enhanced Hydrogen-Storage Capacity in Bimetallic Nanoparticles Reconstructed from Core/Shell Structure by a Process of Hydrogen Absorption/Desorption.* Journal of the American Chemical Society, 2010. **132**(16): p. 5576-5577.
54. Bondarenko, A.S., I.E.L. Stephens, and I. Chorkendorff, *A cell for the controllable thermal treatment and electrochemical characterisation of single crystal alloy electrodes.* Electrochemistry Communications, 2012. **23**(0): p. 33-36.
55. Clavilier, J., et al., *Preparation of monocrystalline Pt microelectrodes and electrochemical study of the plane surfaces cut in the direction of the {111} and {110} planes.* Journal of Electroanalytical Chemistry and Interfacial Electrochemistry, 1979. **107**(1): p. 205-209.
56. Pavia, D.L., et al., *Introduction to Organic Laboratory Techniques*. Proc. - Electrochem. Soc., ed. Thomson Brooks/Cole. 2006.
57. Agilent 1200 Series Refractive Index Detector, Service Manual
58. Woodruff, D.P. and T.A. Delchar, *Modern Techniques of Surface Science*. 1994: Cambridge University Press.
59. Chusuei, C.C. and D.W. Goodman, *X-Ray Photoelectron Spectroscopy*, in *Encyclopedia of Physical Science and Technology (Third Edition)*, A.M. Editor-in-Chief: Robert, Editor. 2003, Academic Press: New York. p. 921-938.
60. http://www.thermo.com/eThermo/CMA/PDFs/Product/productPDF_56731.PDF
61. http://www.thermo.com/eThermo/CMA/PDFs/Product/productPDF_56731.PDF
62. Binnig, G., et al., *Surface Studies by Scanning Tunneling Microscopy*. Physical Review Letters, 1982. **49**(1): p. 57-61.

63. M. Escudero Escribano, Electrocatalysis and surface nanostructuring: atomic ensemble effects and non-covalent interactions, Ph.D. Thesis, Madrid 2011
64. Tang, W., et al., *The importance of surface morphology in controlling the selectivity of polycrystalline copper for CO2 electroreduction.* Physical Chemistry Chemical Physics, 2012. **14**(1): p. 76-81.
65. Magnussen, O.M., *Ordered Anion Adlayers on Metal Electrode Surfaces.* Chemical Reviews, 2002. **102**(3): p. 679-726.
66. Huemann, S., et al., *X-ray Diffraction and STM Study of Reactive Surfaces under Electrochemical Control: Cl and I on Cu(100).* The Journal of Physical Chemistry B, 2006. **110**(49): p. 24955-24963.
67. Andryushchenko, T.N., A.E. Miller, and P.B. Fischer, *Long Wavelength Roughness Optimization during Thin Cu Film Electropolish.* Electrochemical and Solid-State Letters, 2006. **9**(11): p. C181-C184.
68. Pourbaix, M., *Atlas of Electrochemical Equilibria in Aqueous Solutions*. 1974: National Association of Corrosion Engineers.
69. Finšgar, M., et al., *Determination of the Cu2O Thickness on BTAH-Inhibited Copper by Reconstruction of Auger Electron Spectra.* Journal of The Electrochemical Society, 2010. **157**(10): p. C295-C301.
70. Maurice, V., H.H. Strehblow, and P. Marcus, *In situ STM study of the initial stages of oxidation of Cu(111) in aqueous solution.* Surface Science, 2000. **458**(1–3): p. 185-194.
71. Le, M., et al., *Electrochemical Reduction of CO2 to CH3OH at Copper Oxide Surfaces.* Journal of The Electrochemical Society, 2011. **158**(5): p. E45-E49.
72. Gupta, N., M. Gattrell, and B. MacDougall, *Calculation for the cathode surface concentrations in the electrochemical reduction of CO2 in KHCO3 solutions.* Journal of Applied Electrochemistry, 2006. **36**(2): p. 161-172.
73. Hori, Y., et al., *Electrochemical reduction of carbon dioxide at various series of copper single crystal electrodes.* Journal of Molecular Catalysis A: Chemical, 2003. **199**(1–2): p. 39-47.
74. Durand, W.J., et al., *Structure effects on the energetics of the electrochemical reduction of CO2 by copper surfaces.* Surface Science, 2011. **605**(15–16): p. 1354-1359.
75. Berná, A., V. Climent, and J.M. Feliu, *New understanding of the nature of OH adsorption on Pt(1 1 1) electrodes.* Electrochemistry Communications, 2007. **9**(12): p. 2789-2794.

76. Hitotsuyanagi, A., M. Nakamura, and N. Hoshi, *Structural effects on the activity for the oxygen reduction reaction on n(1 1 1)–(1 0 0) series of Pt: correlation with the oxide film formation.* Electrochimica Acta, 2012. **82**(0): p. 512-516.
77. Vega, J.A. and W.E. Mustain, *Effect of CO2, HCO3− and CO3−2 on oxygen reduction in anion exchange membrane fuel cells.* Electrochimica Acta, 2010. **55**(5): p. 1638-1644.
78. Morallo´n, E., et al., *Electrochemical behaviour of Pt(100), Pt(111) and Pt polycrystalline surfaces in hydrogencarbonate solution.* Journal of Electroanalytical Chemistry, 1995. **380**(1–2): p. 47-53.
79. Herrero, E., L.J. Buller, and H.D. Abruña, *Underpotential Deposition at Single Crystal Surfaces of Au, Pt, Ag and Other Materials.* Chemical Reviews, 2001. **101**(7): p. 1897-1930.
80. Markovic, N. and P.N. Ross, *Effect of anions on the underpotential deposition of copper on platinum(111) and platinum(100) surfaces.* Langmuir, 1993. **9**(2): p. 580-590.
81. Greeley, J., *Structural effects on trends in the deposition and dissolution of metal-supported metal adstructures.* Electrochimica Acta, 2010. **55**(20): p. 5545-5550.
82. Strasser, P., S. Koh, and J. Greeley, *Voltammetric surface dealloying of Pt bimetallic nanoparticles: an experimental and DFT computational analysis.* Physical Chemistry Chemical Physics, 2008. **10**(25): p. 3670-3683.
83. Stephens, I.E.L., et al., *Tuning the Activity of Pt(111) for Oxygen Electroreduction by Subsurface Alloying.* Journal of the American Chemical Society, 2011. **133**(14): p. 5485-5491.
84. Sheng, W., H.A. Gasteiger, and Y. Shao-Horn, *Hydrogen Oxidation and Evolution Reaction Kinetics on Platinum: Acid vs Alkaline Electrolytes.* Journal of The Electrochemical Society, 2010. **157**(11): p. B1529-B1536.
85. Beden, B., et al., *The electrooxidation of CO: a test reaction in electrocatalysis.* Electrochimica Acta, 1990. **35**(4): p. 691-704.
86. Hoshi, N. and Y. Hori, *Electrochemical reduction of carbon dioxide at a series of platinum single crystal electrodes.* Electrochimica Acta, 2000. **45**(25–26): p. 4263-4270.
87. López-Cudero, A., A. Cuesta, and C. Gutiérrez, *Potential dependence of the saturation CO coverage of Pt electrodes: The origin of the pre-peak in CO-stripping voltammograms. Part 1:*

Pt(1 1 1). Journal of Electroanalytical Chemistry, 2005. **579**(1): p. 1-12.

88. Trasatti, S., *Work function, electronegativity, and electrochemical behaviour of metals: III. Electrolytic hydrogen evolution in acid solutions.* Journal of Electroanalytical Chemistry and Interfacial Electrochemistry, 1972. **39**(1): p. 163-184.
89. Liu, Z., G.S. Jackson, and B.W. Eichhorn, *PtSn Intermetallic, Core–Shell, and Alloy Nanoparticles as CO-Tolerant Electrocatalysts for H2 Oxidation.* Angewandte Chemie International Edition, 2010. **49**(18): p. 3173-3176.
90. Lucas, C.A., et al., *Structural effects during CO adsorption on Pt–bimetallic surfaces: I. The Pt(100) electrode.* Surface Science, 2000. **448**(2–3): p. 65-76.
91. Lucas, C.A., N.M. Marković, and P.N. Ross, *Structural effects during CO adsorption on Pt-bimetallic surfaces. II. The Pt(111) electrode.* Surface Science, 2000. **448**(2–3): p. 77-86.
92. Bandarenka, A.S., et al., *Design of an Active Site towards Optimal Electrocatalysis: Overlayers, Surface Alloys and Near-Surface Alloys of Cu/Pt(111).* Angewandte Chemie International Edition, 2012. **51**(47): p. 11845-11848.
93. Clavilier, J., et al., *STUDY OF THE CHARGE DISPLACEMENT AT CONSTANT POTENTIAL DURING CO ADSORPTION ON PT(110) AND PT(111) ELECTRODES IN CONTACT WITH A PERCHLORIC-ACID SOLUTION.* Journal of Electroanalytical Chemistry, 1992. **330**(1-2): p. 489-497.
94. Guidelli, R. and W. Schmickler, *Electrified Interfaces in Physics, Chemistry and Biology*. Modern Aspects of Electrochemistry,. Vol. 38. 2005, New York: Kluwer AcademicPlenum Publishers. 303-371.
95. Andersson, K.J., et al., *Adsorption-Driven Surface Segregation of the Less Reactive Alloy Component.* Journal of the American Chemical Society, 2009. **131**(6): p. 2404-2407.
96. Knudsen, J., et al., *A Cu/Pt Near-Surface Alloy for Water−Gas Shift Catalysis.* Journal of the American Chemical Society, 2007. **129**(20): p. 6485-6490.
97. Leung, L.W.H., T.W. Gregg, and D.W. Goodman, *Electrochemical and ultrahigh vacuum characterization of ultrathin copper films on platinum(111).* Langmuir, 1991. **7**(12): p. 3205-3210.
98. Andersson, K.J. and I. Chorkendorff, *On the stability of the CO adsorption-induced and self-organized CuPt surface alloy.* Surface Science, 2010. **604**(19–20): p. 1733-1736.

99. Greeley, J. and J.K. Nørskov, *Electrochemical dissolution of surface alloys in acids: Thermodynamic trends from first-principles calculations.* Electrochimica Acta, 2007. **52**(19): p. 5829-5836.
100. Greeley, J. and M. Mavrikakis, *Near-surface alloys for hydrogen fuel cell applications.* Catalysis Today, 2006. **111**(1–2): p. 52-58.
101. Humbert, M.P. and J.G. Chen, *Correlating hydrogenation activity with binding energies of hydrogen and cyclohexene on M/Pt(111) (M = Fe, Co, Ni, Cu) bimetallic surfaces.* Journal of Catalysis, 2008. **257**(2): p. 297-306.
102. Mayrhofer, K.J.J., et al., *CO surface electrochemistry on Pt-nanoparticles: A selective review.* Electrochimica Acta, 2005. **50**(25–26): p. 5144-5154.
103. Lai, S.C.S., et al., *Mechanisms of Carbon Monoxide and Methanol Oxidation at Single-crystal Electrodes.* Topics in Catalysis, 2007. **46**(3-4): p. 320-333.
104. Rossmeisl, J., et al., *Bifunctional anode catalysts for direct methanol fuel cells.* Energy & Environmental Science, 2012. **5**(8): p. 8335-8342.
105. Koper, M.T.M., T.E. Shubina, and R.A. van Santen, *Periodic Density Functional Study of CO and OH Adsorption on Pt−Ru Alloy Surfaces: Implications for CO Tolerant Fuel Cell Catalysts.* The Journal of Physical Chemistry B, 2001. **106**(3): p. 686-692.
106. Skúlason, E., et al., *Modeling the Electrochemical Hydrogen Oxidation and Evolution Reactions on the Basis of Density Functional Theory Calculations.* The Journal of Physical Chemistry C, 2010. **114**(50): p. 22374-22374.
107. van der Vliet, D.F., et al., *Unique Electrochemical Adsorption Properties of Pt-Skin Surfaces.* Angewandte Chemie, 2012. **124**(13): p. 3193-3196.
108. López-Cudero, A., Á. Cuesta, and C. Gutiérrez, *Potential dependence of the saturation CO coverage of Pt electrodes: The origin of the pre-peak in CO-stripping voltammograms. Part 2: Pt(1 0 0).* Journal of Electroanalytical Chemistry, 2006. **586**(2): p. 204-216.
109. Lebedeva, N.P., et al., *Role of Crystalline Defects in Electrocatalysis: Mechanism and Kinetics of CO Adlayer Oxidation on Stepped Platinum Electrodes.* The Journal of Physical Chemistry B, 2002. **106**(50): p. 12938-12947.

Included papers

PCCP

Cite this: *Phys. Chem. Chem. Phys.*, 2012, **14**, 76–81

www.rsc.org/pccp

COMMUNICATION

The importance of surface morphology in controlling the selectivity of polycrystalline copper for CO_2 electroreduction†

Wei Tang,[a] Andrew A. Peterson,[b] Ana Sofia Varela,[a] Zarko P. Jovanov,[a] Lone Bech,[a] William J. Durand,[b] Søren Dahl,[a] Jens K. Nørskov[b] and Ib Chorkendorff*[a]

Received 23rd August 2011, Accepted 20th October 2011
DOI: 10.1039/c1cp22700a

This communication examines the effect of the surface morphology of polycrystalline copper on electroreduction of CO_2. We find that a copper nanoparticle covered electrode shows better selectivity towards hydrocarbons compared with the two other studied surfaces, an electropolished copper electrode and an argon sputtered copper electrode. Density functional theory calculations provide insight into the surface morphology effect.

The electrochemical conversion of CO_2 into hydrocarbons is of growing interest, since it could offer a way to continue the convenient use of carbon based fuels in a CO_2 neutral manner. The challenge is to convert CO_2 under ambient conditions, such that the reaction can run at affordable cost and be adopted on a wide scale in decentralized units positioned where surplus electrical energy is available. The electrical energy would be provided by sustainable energy options (such as wind, solar and hydro) where the electricity production displays strong temporal variations and therefore must be averaged on different time scales. Electrochemical fixation of CO_2 is potentially a pathway for long term chemical storage of sustainable energy,[1] providing the products which could transport fuel.

In the past few decades, many metals were investigated as catalysts for the electroreduction of CO_2 with a view to improving the yield of desirable molecules and control the product selectivity.[2] Among the possible products, hydrocarbons such as methane and ethylene are the most desired, due to their high energy densities and widespread use in the current infrastructure. Among the studied metals, copper is the only metal that produces hydrocarbons with high Faradaic efficiency, instead of producing less valuable products such as formic acid or CO.[3,4] To produce useful hydrocarbons, such as CH_4 ($CO_2 + 2H_2O \rightarrow CH_4 + 2O_2$), a total potential of about 2.5 V is required, including the thermodynamic reaction potential of 1.1 V, an overpotential of ~1 V[4] on the copper electrode for the hydrogenation reaction and an overpotential of ~0.4 V[5,6] for the oxygen evolution reaction. This results in a total energy efficiency of ~40%. With its unique electrocatalytic properties and high abundance, polycrystalline copper is a promising candidate for the electrochemical conversion of CO_2 at an industrial scale. Therefore, it is essential to understand how to prepare a polycrystalline copper electrode in order to optimize its catalytic activity. In the past, it has been reported that the Faradaic efficiencies for this reaction are strongly affected by pretreatment of the copper electrode.[7,8] However, the underlying reasons for the influence of the pretreatment are still not clearly established. In this work, different pretreatments were used to prepare copper electrodes for CO_2 reduction. Three copper electrodes (Samples A, B and C) were investigated:

Sample A: a copper electrode (25 mm × 12.5 mm, thickness 1 mm, 99.999%, Goodfellow) and a connecting copper wire (diameter 0.5 mm, 99.999%, Goodfellow) were cleaned by electropolishing. The electropolishing was performed by applying a potential of +2 V between the copper electrode and a platinum cathode in phosphoric acid (1 mol L^{-1}) for 20 min and rinsing the copper electrode with deionized water (18 MΩ). As electropolishing occurs at anodic potential, a certain amount of electrode material is stripped from the surface along with surface impurities.[9,10] During the stripping, the protruding parts in the surface profile are preferentially dissolved and thereby results in smooth, ordered terraces,[9–11] as shown by scanning tunneling microscopy (STM).[9,12,13] The surface morphology resulting from electropolishing is heavily influenced by electrolyte ion adsorption.[12,13] Strong binding of adsorbates enhances surface diffusion of metal atoms.[12] The terraces are stabilized by the formation of ordered adsorbate layers.[13] Consequently, the terraces are harder to dissolve than steps. Electropolishing in phosphoric acid is a routine procedure for the preparation of planar copper single crystal surfaces. The sample shows a smooth surface in scanning electron microscopy (SEM) as shown in Fig. 1a. Hence, based on our SEM images and earlier STM studies,[9,14] the electropolished surface will probably be dominated by low indexed terraces such as (100) and (111), but will also contain a significant number of low coordinated surface sites such as steps.

Sample B: a copper electrode as in Sample A covered with nanoparticles. The copper nanoparticles were formed in two steps. In the first step, the potential at the electropolished copper electrode was scanned between −0.6 and +1.15 V *vs.* RHE (see Fig. 2a) at 20 mV s^{-1} in N_2 saturated $KClO_4$ (0.1 M, Aldrich, 99.99%).

---

[a] *Center for Individual Nanoparticle Functionality, Department of Physics, Building 312, Technical University of Denmark, DK-2800 Lyngby, Denmark. E-mail: ibchork@fysik.dtu.dk*
[b] *SUNCAT Center for Interface Science and Catalysis, Department of Chemical Engineering, Stanford University, Stanford, CA, USA*

† Electronic supplementary information (ESI) available. See DOI: 10.1039/c1cp22700a

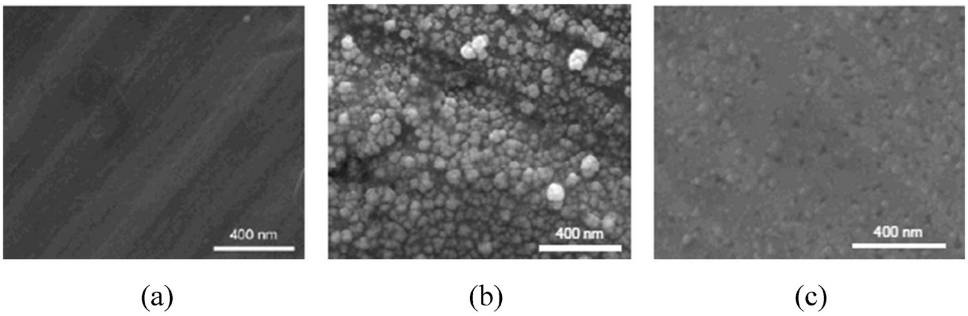

Fig. 1 Scanning Electron Microscopy for three surfaces: (a) Sample A (electropolished surface), (b) Sample B (copper nanoparticle covered surface) and (c) Sample C (sputtered surface).

The pH value of the electrolyte during the cyclic voltammetry was influenced by hydrogen evolution during the most scan potentials and it increased from an initially neutral value of ~7 up to the finally measured value of 10.5 after 20 cycles. After cyclic voltammetry, the electrolyte turned slightly yellow-brownish due to eventually dissolved species, as well as to formation of suspended brownish particles. According to the Pourbaix diagram for copper,[15] the species present in alkaline solution are not expected to be the Cu^{2+} ions, but rather CuO_xH_y species. In the second step, along with reduction of the copper containing species formed at the first step, the copper was redeposited on the electrode surface. The redeposition was performed in CO_2 saturated $KClO_4$ (pH = 6.0, 0.1 M) with a constant bias of −1.3 V *vs.* RHE for 20 minutes. The redeposition of copper is observed to be dependent on the pH value of the electrolyte, as reported previously.[16] Purging with CO_2 was used to adjust the pH of the electrolyte to a value of ~6. After redeposition of copper, the electrode surface turned dark as shown in Fig. S1 (ESI†). SEM was used to characterize the dark electrode. As seen in Fig. 1b a few layers of copper nanoparticles with size of 50–100 nm cover the copper surface. Estimated from the SEM image, the surface area of Sample B is greater than the geometric surface area of the electrode by a factor of 2–3.

Sample C: a copper electrode as in Sample A sputtered with argon ions. The sputtering was conducted in an XPS system (Theta Probe, Thermo Scientific) with 3 keV Ar^+ ions and 4 μA emission current for 10 min. At each cycle of Ar^+ sputtering, an area of 10 mm × 10 mm was bombarded with Ar^+ ions, removing approximately 30 monolayers (~10 nm) from the surface. Six different areas on both sides were sputtered to treat the whole electrode (25 mm × 12.5 mm). On a microscopic scale, Sample C shows a roughened surface topography, due to pit formation after Ar^+ bombardment and island growth by metal atoms redeposition, as observed before in the STM studies[17] (Fig. 1c).

There is some controversy in the literature as to whether the active phase for CO_2 electroreduction is metallic Cu[2–4,18–22] or Cu_2O.[8,23] Consequently, the three samples were characterized using X-ray Photoelectron Spectroscopy (XPS). The XPS spectrum of the sputtered copper surface (Sample C), as prepared, represents that of a clean metallic surface. The other two samples contain some surface oxygen due to the transfer under ambient conditions. However, there is no chemical shift observed due to copper (II) oxide. All three surfaces exhibit the following signals for copper: Cu 2p3/2 at 932.4 eV and Cu 2p1/2 at 952.2 eV, that correspond to metallic copper or copper (I), see Fig. S2a (ESI†).

To differentiate between metallic Cu and Cu_2O, the Cu Auger spectrum was measured.[24] Fig. S2b (ESI†) shows the copper Auger lines for the three surfaces, as prepared. The sputtered sample naturally only shows the fingerprint of metallic copper since no oxygen was present here at all. The electropolished sample also appears to be metallic, *i.e.*, the small amount of oxygen adsorbed during the transfer is not significantly influencing the Auger signal. This could be explained by the preparation procedure, which involves applying a positive potential in a phosphoric acid solution (pH 1.5) where, according to the copper Pourbaix diagram, the stable species should be Cu^{2+} and no oxide species are expected.[15] The nanoparticle covered surface (Sample B) shows an Auger peak that corresponds to Cu_2O. This sample was prepared in 0.1 M $KClO_4$ solution within the pH range where Cu_2O can be formed. It was unclear whether the nanoparticles were oxidized when they formed, during the redeposition step, or simply by the exposure to the electrolyte. With the aim of clarifying this issue, we studied the Auger signals on the sputtered sample in following cases: under UHV conditions, air exposed (30 min) and after being dipped into the electrolyte. Based upon Fig. S2c (ESI†), exposure to the air leads to a slightly oxidized surface, while dipping the sample into the electrolyte forms a fully oxidized surface, as observed on the nanoparticle covered sample. Therefore, the XPS measurements are insufficient to identify the active phase of copper for electrocatalytic CO_2 reduction. Only *in situ* measurements would be able to identify the real surface state during the electrocatalytic process.

Even though we do not have any measurements of the oxidation state of copper during the catalytic reaction, we take the view that it is highly unlikely that the active phase is a form of copper oxide, rather than metallic Cu. There is a significant driving force for the reduction of copper oxide under reaction conditions, *i.e.* ~−1.5 V overpotential relative to the Nernst potential of the reduction of Cu_2O to metallic Cu at pH ~6 and −1.1 V *vs.* RHE.[15] Notably, *in situ* STM studies have shown that at the most ~−1 V overpotential is required to completely reduce Cu oxide to form ordered Cu(111) terraces in 0.1 M NaOH.[25] Moreover, Le *et al.*[26] found that their Cu oxide catalyst reduced to metallic Cu at an overpotential of −1.3 V, relative to the Cu/Cu_2O reversible potential in CO_2 saturated 0.5 M $KHCO_3$.

As electrochemical characterization of the surfaces, cyclic voltammetries in N_2 saturated and CO_2 saturated atmospheres were performed on the three samples. A non-buffered solution

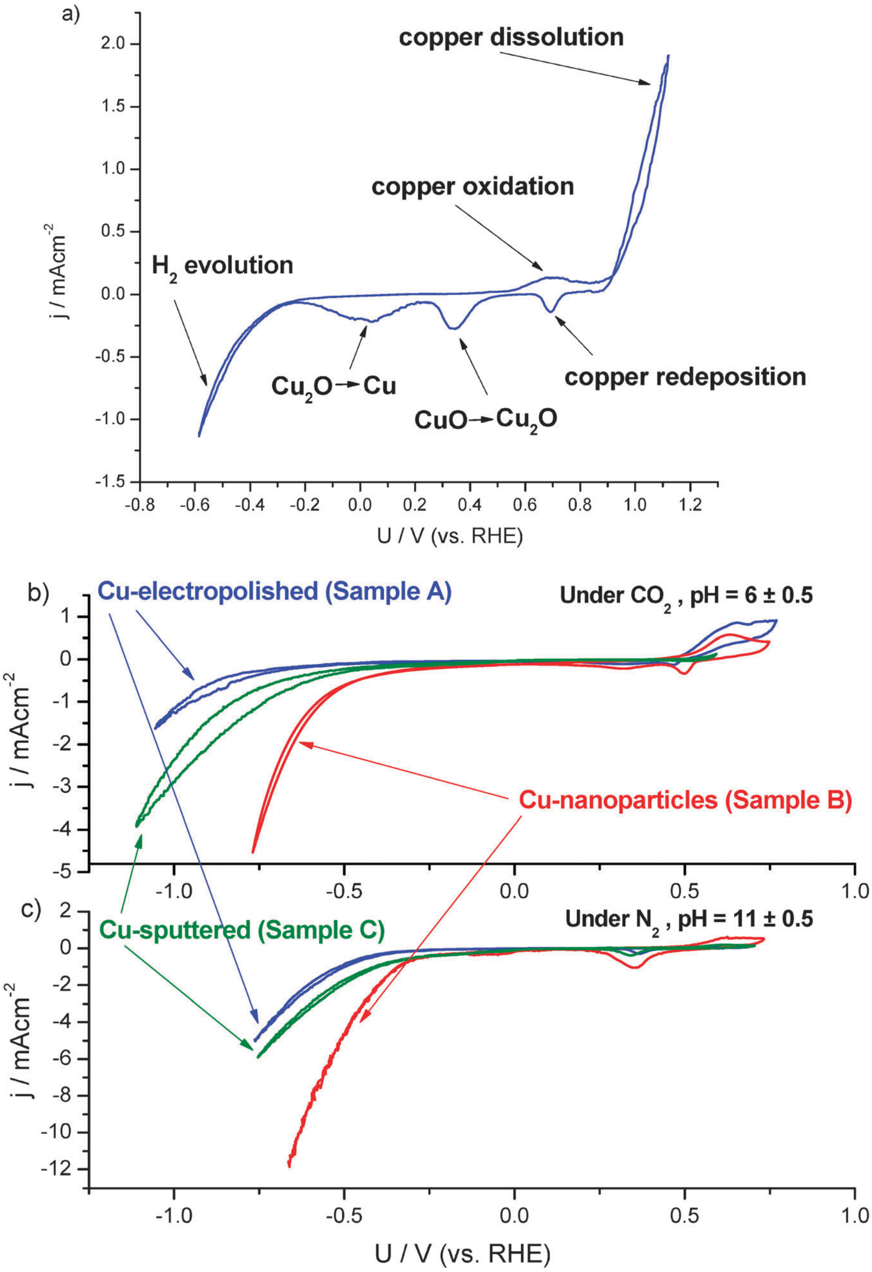

Fig. 2 Cyclic voltammogram of the formation of copper nanoparticles in 0.1 M $KClO_4$ purged with N_2 at pH 10.5 (a); cyclic voltammogram of the electropolished copper surface, copper nanoparticle covered surface and sputtered copper surface in 0.1 M $KClO_4$ purged with CO_2 (b) and N_2 (c). The current density is normalized by the geometric area of the electrode surface. The overpotentials are corrected for ohmic resistance between the working and reference electrode.

$KClO_4$ (0.1 M) was used as electrolyte, with the pH value monitored throughout all the steps of the electrochemical process. The as-made electrolyte has pH of 7 ± 0.5. Pre-electrolysis was performed in order to remove possible traces of impurities, which shifts the pH to values of *ca.* 8. Cycling to very negative potentials also increases pH. CVs in N_2 were recorded at alkaline pH 11 ± 0.5. However, CO_2 bubbling lowers the pH down to 6 ± 0.5. In Fig. 2(b and c), the cyclic voltammograms (CV) in saturated 0.1 M $KClO_4$ under CO_2 and N_2, respectively, are shown against the reversible hydrogen electrode (RHE), with the potential scales corrected for pH and confirmed through the alignment of the Cu(I)-oxide formation peak. As expected according to the copper Pourbaix diagram,[15] these peaks appear at the same potential against RHE when CVs are performed in the same potential range. Plotting the CVs against RHE enabled the comparison of the onset potentials for the reduction process, such as the hydrogen evolution reaction (HER) in the N_2 saturated environment and the two simultaneous processes HER and CO_2 reduction in the CO_2 saturated environment. Firstly in the N_2 saturated environment, the formation of the cuprous oxide is observed at potentials of *ca.* 0.65 V *vs.* RHE, followed by its reduction during cathodic scan at ~0.3 V *vs.* RHE, which is consistent with the thermodynamical potential of Cu to Cu_2O at 0.47 V *vs.* RHE.[15] The electropolished polycrystalline copper surface (Sample A) exhibits an exponential increase of cathodic current at −0.45 V, indicative of hydrogen evolution. The nanoparticle covered surface (Sample B) and the sputtered surface (Sample C) have the onset potential for hydrogen evolution earlier than Sample A. Moreover, at the most negative potentials, the cathodic current density is greater on roughened surfaces than on the electropolished surface. This could partially be attributed to the increased surface area of the nanoparticle covered surface. However, we can consider that the electropolished sample and the argon sputtered sample have the same surface area. Therefore, the difference in onset potential and current values, between these two electrodes, can only be attributed to surface morphology. On the other hand, the difference between the current values for the electropolished electrode and the nanoparticles covered electrode is greater than the expected from the difference in surface area. For instance, at −0.6 V the current is 4.5 times higher on the nanoparticle covered surface than on the smooth one. The surface area increase contributes only with the previously estimated factor of 2–3.

In addition, higher surface area does not explain the improved onset potential of the roughened surface, which is more indicative of a better electrocatalytic activity for hydrogen evolution on the surface dominated by low coordinated surface atoms.

Cyclic voltammetry in CO_2 (pH 6.0 ± 0.5) shows similar trends as in nitrogen where the higher current densities were observed on roughened surfaces (Samples B and C). For instance, at −0.75 V *vs.* RHE, the current density of the nanoparticle covered surface (Sample B) is 10 times higher compared to the electropolished surface (Sample A), which again is a proof that the surface morphology contributes more to the current densities than just the effect of surface area increase.

The onset potentials, when the current density exceeds 1 mA cm^{-2}, appear at −1.0 V for the electropolished surface, at −0.8 V for the sputtered surface and around −0.6 V for the nanoparticle covered surface, which are more negative than that observed in N_2. The more negative onset potentials indicate the presence of adsorbed species during CO_2 reduction. According to Hori[2], the CO_2 reduction reaction proceeds with the formation of adsorbed CO as an intermediate product. The Faradaic current is being contributed from two competing reactions:

$$*CO_2 + 2H^+ + 2e^- \rightarrow *CO + H_2O$$

(The "*" indicates that it adsorbs to the surface)

$$2*H^+ + 2e^- \rightarrow H_2$$

To confirm a better catalytic performance of Sample B the reaction products were determined, after applying a constant potential of −1.1 V *vs.* RHE on a CO_2 saturated electrolyte for 15 minutes. Results from the electrocatalytic reactions on the three samples are shown in Fig. 3. Faradaic efficiencies of the major gas-phase products are expressed by monitoring the product distribution using gas chromatography and relating those to the charge consumed during the reaction. After 15 minutes of reaction, the concentration of the liquid product was below the detection limit. To identify the liquid products the reaction was run for 24 hours using the electropolished sample. According to the HPLC analysis the only product present in the liquid phase is formic acid (faradaic efficiency of ~7.5%). During the 24 hour reaction the copper electrode turned black, therefore it was characterized by SEM (see Fig. S3, ESI†). The SEM images showed a nanoparticles covered surface which indicates that during the reaction some copper is dissolved and redeposited on the electrode, generating a roughened surface. Since the surface structure is modified during the reaction the faradaic efficiency obtained during the 24 hour experiment cannot be attributed only to a smooth surface. In Fig. 3 it is clear that a higher total efficiency towards CO_2 reduction gas products (methane, ethylene and CO) is obtained using the roughened surface (Sample B), while the smooth surface (Sample A) has a lower faradaic efficiency towards the products related to CO_2 reduction. On the other hand, the selectivity towards hydrogen is higher on the smooth surface (Sample A) than on the roughened surfaces (Samples B and C). These two facts imply the importance of the roughening of the copper surface for the better selectivity towards CO_2 reduction. The formation ratio between CH_4 and C_2H_4 is also noteworthy. Sample A produces C_2H_4 with the faradaic efficiency of 14% and CH_4 with 5%. Sample B preferentially converts CO_2 to C_2H_4 with the faradaic efficiency of 36%, but only 1% to CH_4. Sample C has a slightly lower faradaic efficiency of 26% towards C_2H_4, but only 8% towards CH_4. These results indicate that production of C_2 is favored on a roughened surface.

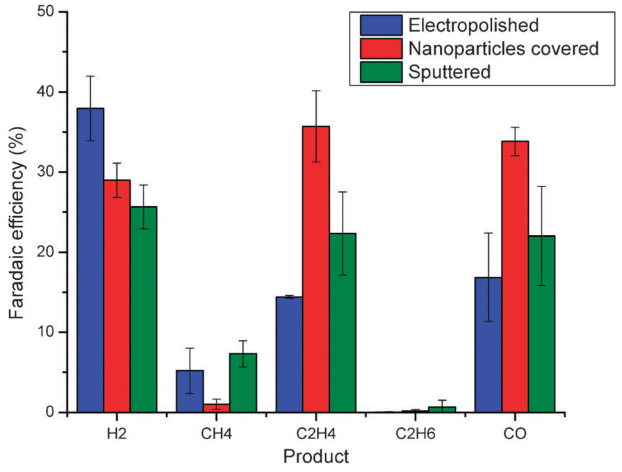

Fig. 3 Faradaic efficiency for the products of electroreduction of CO_2 on three surfaces in CO_2-saturated 0.1 M $KClO_4$ upon −1.1 V *vs.* RHE, including Sample A (electropolished surface), Sample B (copper nanoparticle-covered surface) and Sample C (sputtered surface).

Better catalytic performance of the roughened surface is obtained due to two different effects: achieved higher current densities and improved faradaic selectivity to hydrocarbons. Increase in current densities is easily explained taking into account the higher surface area of the roughened sample, providing more active sites for both CO_2 conversion and hydrogen evolution. Improvement in the selectivity towards hydrocarbons suggests that the morphology of the surface plays a significant role in the process. As established earlier, the smooth surface consists mostly of low index crystal facets, such as Cu(100) and Cu(111). However, the roughened surfaces contain significantly more low-coordination sites, such as steps, edges and defects that seem to be more active towards CO_2 reduction.

Our observations on different surfaces are in agreement with Hori*'s* investigations[2] of CO_2 electroreduction on single crystal Cu surfaces in 0.1 M $KHCO_3$ aqueous solution. These investigations include terrace facets, Cu(111) and Cu(100), that can be compared with the smooth surface of Sample A in our case. Stepped surfaces like Cu(311), Cu(511) and Cu (711) can be related to roughened surfaces on Samples B and C.[19–20,22] Hori *et al.* observed that the stepped copper surfaces exhibit different selectivities and that the reactions occur at lower potentials for a specific current density compared to the terrace facets. They also concluded that the selectivity ratio between CH_4 and C_2H_4 depends strongly on the crystal orientation.[19–20,22] They reported that Cu(111) produced CH_4 with a faradaic efficiency of 50.5% and C_2H_4 with an efficiency of 8.8%. On the other hand, the stepped surface, Cu(711), was more selective towards C_2H_4, with a Faradaic efficiency of 3.8% towards CH_4 and 51.6% towards C_2H_4. Given that CO_2 reduction is strongly influenced by the electrolyte, working potentials, and pH,[4] it is difficult to make a direct, quantitative comparison of Hori *et al.*'s results to our own. Nevertheless, our observations, whereby the selectivity towards C_2H_4 or CH_4 depends on the surface morphology, seem to be consistent with those of Hori *et al.* A recent paper by Koper and co-workers[27] sheds light on the correlation between the formation of CO and ethylene. They propose two different pathways: one for methane and another one for ethylene formation. Our results indicate that on different surfaces CO and ethylene formation follow the same trends. Higher CO production seems to favor the formation of ethylene, as previously suggested.[21,27] It is also worth mentioning that the highest selectivity for ethylene on nanoparticle covered surface seems to be a reason for suppressed methane production. However, based on our results, we are not able to make strong conclusions on intermediates required neither for methane nor for ethylene formation.

In order to understand the apparent effect of surface pretreatment on the catalytic performance of Cu towards CO_2 electroreduction, density functional theory (DFT) calculations were performed on the fcc(111), fcc(100) and fcc(211) facets of Cu. As discussed earlier, the roughened surfaces would contain a larger number of defects such as steps, the effect of which can be modeled by the (211) facet. On the other hand, the electropolished surface should be dominated by the terrace facets, such as (111) and (100).

Free energetics of the hydrogen evolution reaction was calculated with DFT and is shown in Fig. S4 (ESI†); the stepped sites (211) are predicted to have higher activity than the terrace (111) and (100) sites since the free energy of the adsorbed hydrogen intermediate (H*) is closer in free energy to the initial and final states of the reaction. This may translate into a higher activity for hydrogen evolution on these stepped sites. However, this may have less of an effect on the onset potential than the free energy diagram would suggest: the steps on the Cu surface are inaccessible to adsorbed H at low bias (less negative potentials), since they can be blocked by hydroxyl (OH) groups. This is shown in Fig. S5 (ESI†), in which DFT calculations show that OH adsorption from water proceeds spontaneously at 0 V *vs.* RHE on the (211) and (100) copper surfaces causing the surface blocking.

Density functional theory calculations were also employed to have a better understanding on the improved hydrocarbon selectivity of the roughened surfaces. The conversion of electronic energies to free energies, the effect of solvation, and the effect of electric fields were handled in a manner identical to that in a previous study that examined CO_2 reduction at copper electrodes.[21,28] In the previous study, the elementary proton–electron transfer steps have been proposed for the process of reducing CO_2 to hydrocarbons. The potential requirements in CO_2 reduction to methane on Cu fcc(211) surfaces have been proposed, where the protonation of adsorbed CO to produce adsorbed CHO is identified as the limiting step.[21] While many factors control the reactivity of the different facets of copper during the CO_2 electrochemical reduction and a complete understanding will require a more detailed model, we based on this previous study to determine the effect of surface roughness on the energetics of this transformation. Therefore we calculated the free energies of the transformation of CO* to both CHO* and COH* (where an asterisk, *, indicates an adsorbed species) on three different copper crystal facets, which were taken to be indicative of the range of smooth and roughened surfaces encountered in polycrystalline copper.

These three facets are the (111) surface, which is a smooth facet containing the highest surface density of metal atoms and 3-fold binding sites, the (100) surface, which is a smooth facet containing a lower surface density of metal atoms and 4-fold binding sites, and the (211) surface, which contains a step. Fig. 4 compares the energetics of CO* protonation on the (111), (100), and (211) surfaces at 0 V *vs.* RHE. It can be seen that on all surfaces, the route to CHO* is favored over the

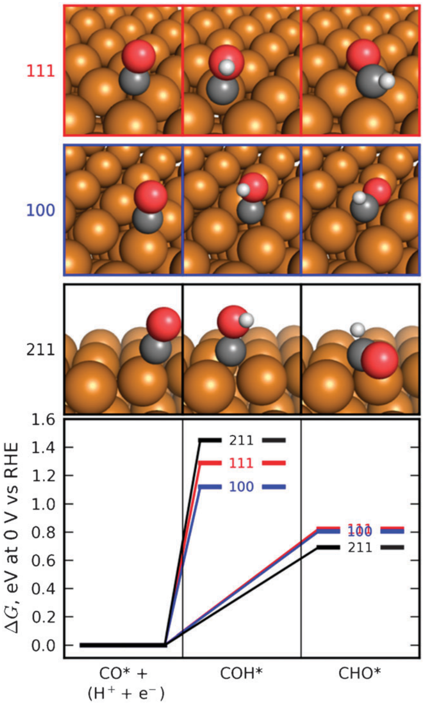

Fig. 4 Calculated free energies, at 0 V *vs.* reversible hydrogen electrode (RHE), of the protonation of adsorbed CO to form adsorbed COH or CHO on the (111), (100), and (211) facets of the face-centered cubic copper crystal. The protonation proceeds most favorably on the (211) facet to the CHO adsorbate. See also Durand *et al.*[28]

route to COH*, and the (211) surface stabilizes this transformation relative to the (111) and (100) surfaces. This may partially explain the higher current and higher selectivity to hydrocarbons experimentally observed on the roughened surfaces. It has been suggested that the ethylene is formed from a non-electrochemical surface reaction between adsorbed species, for example the coupling of CHO* to *OCHCHO*.[21] The high selectivity of C_2H_4 and low selectivity of CH_4 on Sample B are possibly due to high coverage of CHO* or other adsorbed species along step edges. Therefore the formation rate of C_2H_4 is influenced by the surface crystal orientation.

Among the three copper surfaces with different pretreatments and thus morphologies, the roughened copper surfaces (the copper nanoparticle covered surface and the sputtered surface) show higher selectivities towards hydrocarbons. In particular, our *in situ* activation method to prepare the copper nanoparticle surface is simple and effective. The morphology effect is explained by the greater abundance of undercoordinated sites on the roughened surfaces. DFT calculations indicate that these sites are more likely to be the active sites for CO_2 reduction. On the basis of our results, we propose that the activity of Cu could be enhanced further by preparing smaller nanoparticles of Cu, as these would have a greater density of undercoordinated sites.

Acknowledgements

This work was supported by the "Catalysis for Sustainable Energy" (CASE) research initiative, which is funded by the Danish Ministry of Science, Technology and Innovation. Center for Individual Nanoparticle Functionality is funded by The Danish National Research Foundation. The Center for Atomic-scale Materials Design is funded by the Lundbeck Foundation. This material is based in part upon work supported by the Air Force Office of Scientific Research through the MURI program under AFOSR Award No. FA9550-10-1-0572. The HPLC analysis of the liquid face was carried out at Haldor Topsøe by Christian Mårup Osmusdsen. The authors sincerely thank Dr Ifan Stephens and Dr Francisco Pérez Alonso for discussion and suggestion.

References

1 F. Schuth, *Eur. Phys. J. Spec. Top.*, 2009, **176**, 155–166.
2 Y. Hori, in *Modern Aspects of Electrochemistry*, ed. C. G. Vayenas, Springer, 2008, pp. 89–189.
3 M. Gattrell, N. Gupta and A. Co, *J. Electroanal. Chem.*, 2006, **594**, 1–19.
4 Y. Hori, A. Murata and R. Takahashi, *J. Chem. Soc., Faraday Trans. 1*, 1989, **85**, 2309–2326.
5 Y. Gorlin and T. F. Jaramillo, *J. Am. Chem. Soc.*, 2010, **132**, 13612–13614.
6 S. Trasatti, *Electrochim. Acta*, 1984, **29**, 1503–1512.
7 M. R. Goncalves, A. Gomes, J. Condeco, R. Fernandes, T. Pardal, C. A. C. Sequeira and J. B. Branco, *Energy Convers. Manage.*, 2010, **51**, 30–32.
8 Y. Terunuma, A. Saitoh and Y. Momose, *J. Electroanal. Chem.*, 1997, **434**, 69–75.
9 S. Huemann, N. T. M. Hai, P. Broekmann, K. Wandelt, H. Zajonz, H. Dosch and F. Renner, *J. Phys. Chem. B*, 2006, **110**, 24955–24963.
10 J. K. Zhang, G. N. Okeke and C. H. B. Mee, *J. Phys. E: Sci. Instrum.*, 1986, **19**, 314–314.
11 T. N. Andryushchenko, A. E. Miller and P. B. Fischer, *Electrochem. Solid-State Lett.*, 2006, **9**, C181–C184.
12 S. Horch, H. T. Lorensen, S. Helveg, E. Laegsgaard, I. Stensgaard, K. W. Jacobsen, J. K. Norskov and F. Besenbacher, *Nature*, 1999, **398**, 134–136.
13 O. M. Magnussen, *Chem. Rev.*, 2002, **102**, 679–725.
14 H. I. Rasool, E. B. Song, M. J. Allen, J. K. Wassei, R. B. Kaner, K. L. Wang, B. H. Weiller and J. K. Gimzewski, *Nano Lett.*, 2011, **11**, 251–256.
15 E. Protopopoff and P. Marcus, *Electrochim. Acta*, 2005, **51**, 408–417.
16 N. T. M. Hai, K. Wandelt and P. Broekmann, *J. Phys. Chem. C*, 2008, **112**, 10176–10186.
17 T. Michely and G. Comsa, *Surf. Sci.*, 1991, **256**, 217–226.
18 Y. Hori, H. Konishi, T. Futamura, A. Murata, O. Koga, H. Sakurai and K. Oguma, *Electrochim. Acta*, 2005, **50**, 5354–5369.
19 Y. Hori, I. Takahashi, O. Koga and N. Hoshi, *J. Phys. Chem. B*, 2002, **106**, 15–17.
20 Y. Hori, I. Takahashi, O. Koga and N. Hoshi, *J. Mol. Catal. A: Chem.*, 2003, **199**, 39–47.
21 A. A. Peterson, F. Abild-Pedersen, F. Studt, J. Rossmeisl and J. K. Norskov, *Energy Environ. Sci.*, 2010, **3**, 1311–1315.
22 I. Takahashi, O. Koga, N. Hoshi and Y. Hori, *J. Electroanal. Chem.*, 2002, **533**, 135–143.
23 P. Dubé and G. M. Brisard, *J. Electroanal. Chem.*, 2005, **582**, 230–240.
24 F. Matjaz, P. Sebastijan, K. Anton, C. J. Kova and M. Ingrid, *J. Electrochem. Soc.*, 2010, **157**, C295–C301.
25 V. Maurice, H.-H. Strehblow and P. Marcus, *Surf. Sci.*, 2000, **458**, 185–194.
26 M. Le, M. Ren, Z. Zhang, P. T. Sprunger, R. L. Kurtz and J. C. Flake, *J. Electrochem. Soc.*, 2011, **158**(5), E45–E49.
27 K. J. P. Schouten, Y. Kwon, C. J. M. van der Ham, Z. Qin and M. T. M. Koper, *Chem. Sci.*, 2011, **2**, 1902–1909.
28 W. J. Durand, A. A. Peterson, F. Studt, F. Abild-Pedersen and J. K. Nørskov, *Surf. Sci.*, 2011, **605**(15–16), 1354–1359.

DOI: 10.1002/anie.201205314

Electrocatalysis

Design of an Active Site towards Optimal Electrocatalysis: Overlayers, Surface Alloys and Near-Surface Alloys of Cu/Pt(111)**

*Aliaksandr S. Bandarenka, Ana Sofia Varela, Mohammedreza Karamad, Federico Calle-Vallejo, Lone Bech, Francisco J. Perez-Alonso, Jan Rossmeisl, Ifan E. L. Stephens, and Ib Chorkendorff**

Electrochemical devices hold promise as a sustainable route for energy conversion to meet the requirements of future generations. Their development is contingent upon improvements to the functionality of their electrodes.[1] The catalytic performance of these materials is controlled by the atomic and electronic structure of their active sites.[1b,2] Therefore, the design of the appropriate active site is crucial to obtain high catalytic activity, especially where multi-functionality is needed. However, the control of a given surface on an atom-by-atom basis is particularly challenging.

The electrochemical oxidation of CO is the prototypical bifunctional reaction.[3] The active site needs to be reactive towards both oxygen and carbon atoms. Because Pt is reactive towards carbon atoms and Cu is reactive towards oxygen atoms,[4] these are two obvious candidates for the construction of a bifunctional catalyst for electrochemical CO oxidation.

Fundamental studies have shown that overlayers (OLs), near-surface alloys (NSAs), and surface alloys (SAs) of Cu/Pt show markedly different characteristics from pure Cu or Pt surfaces.[5] Herein, we present a study of how to control the reactivity of the Cu/Pt(111) system by modifying the atomic structure in an electrochemical environment. We employ electrochemical measurements, angle-resolved X-ray photoelectron spectroscopy (AR-XPS), and density functional theory (DFT) calculations. This has allowed us to make a detailed comparison between experimental results and theoretical simulations on identical systems.

The Cu/Pt(111) OL, SA, and NSA were prepared according to the general method shown in Figure 1. The resulting AR-XPS depth profiles in Figure 1 confirm that the desired structures were formed.[5c]

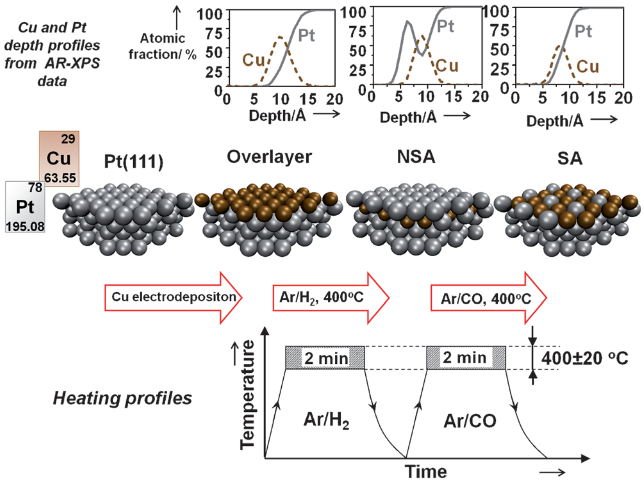

Figure 1. General scheme used to prepare Cu/Pt(111) OL, NSA, and SA. The corresponding depth profiles, obtained using AR-XPS, are shown at the top.

There are considerable differences between the voltammograms of the surfaces in 0.1 M $HClO_4$, as shown in Figure 2. On Pt(111), from 0.05 V to 0.4 V there is a reversible peak arising from the adsorption/desorption of *H (herein * denotes a free site and *X an adsorbed species, X); from 0.6 V to 0.9 V there is a reversible peak arising from the adsorption of *OH.[6] On the NSA, the *H peak is shifted negatively and the *OH peak is shifted positively, suggesting that both *H and *OH are destabilized,[5c] consistent with our DFT calculations, described in the Supporting Information. On the other hand, the Cu/Pt(111) overlayer exhibits a featureless voltammogram between 0.05 V and 0.38 V (the potential was limited to this range because above 0.38 V there was a small oxidation current, prior to the main peak at 0.7 V, as shown in the inset in Figure S5a of the Supporting Information; this could be attributed to Cu dissolution). According to our *CO-displacement measurements (see

---

[*] Dr. A. S. Bandarenka, A. S. Varela, Dr. L. Bech, Dr. F. J. Perez-Alonso, Dr. I. E. L. Stephens, Prof. I. Chorkendorff
Center for Individual Nanoparticle Functionality
Technical University of Denmark, Building 312
DK-2800 Lyngby (Denmark)
E-mail: ibchork@fysik.dtu.dk
Homepage: http://www.cinf.dtu.dk

M. Karamad, Dr. F. Calle-Vallejo, Dr. J. Rossmeisl
Center for Atomic-Scale Material Design
Technical University of Denmark, Building 307
DK-2800 Lyngby (Denmark)

Dr. A. S. Bandarenka
Center for Electrochemical Sciences, Ruhr Universität Bochum
Universitätsstrasse 150 NC 4/73, 44801 Bochum (Germany)

[**] Funding by the Danish Strategic Research Council's (DSRC) HyCycle program and SERC project (grant no. 2104-06-0011), the Spanish Government's, "Programa Nacional de Movilidad de Recursos Humanos del PN de I-D+I 2008-2011", the PSO-financed ForskEL/ELgrant (HighPerformanceMEA's, project 010076) from energinet.dk and Catalysis for Sustainable Energy research initiative, funded by the Danish Ministry of Science Technology and Innovation is acknowledged. A.S.B. acknowledges additional financial support from the European Union and the MWIFT-NRW (Hightech.NRW competition). The Center for Atomic-scale Materials Design is supported by the Lundbeck Foundation. The Center for Individual Nanoparticle Functionality is supported by the Danish National Research Foundation.

Supporting information (experimental details) for this article is available on the WWW under http://dx.doi.org/10.1002/anie.201205314.

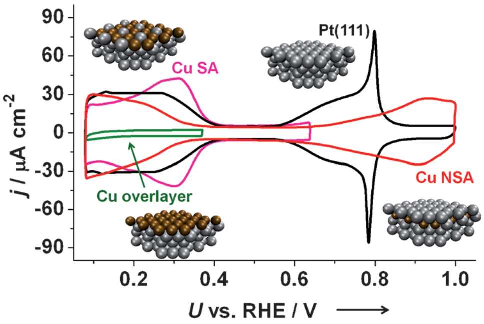

Figure 2. Cyclic voltammograms in 0.1 M $HClO_4$ of: Pt(111), Cu OL on Pt(111), Cu/Pt(111) NSA, and Cu/Pt(111) SA. $dU/dt = 50\ mV\,s^{-1}$.

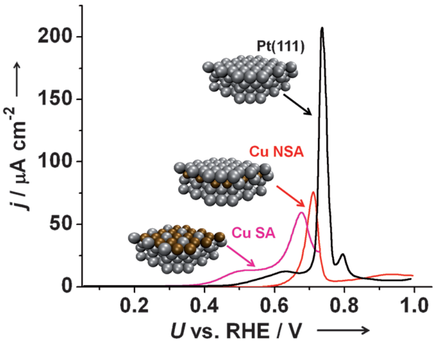

Figure 3. *CO stripping voltammograms for Pt(111), Cu/Pt(111) SA, and Cu/Pt(111) NSA, in $HClO_4$, $dU/dt = 20\ mV\,s^{-1}$. The CO was adsorbed at 0.05 V, whereas the voltammogram was carried out in a CO-free solution.

Supporting Information), the surface is covered with anionic species in this potential range, which our DFT calculations suggest should be *OH. Within the short time required for a voltammogram, no further anion adsorption takes place, explaining the absence of any peaks. On the other hand, the Cu/Pt(111) SA voltammogram has a reversible peak centered at 0.3 V. The DFT calculations would suggest that this is due to the adsorption of *OH on the Cu sites: *OH binds the SA 0.6 eV stronger than Pt(111), in good agreement with the approximate shift of 0.5 V between the peak on the SA and that of *OH adsorption on Pt(111).

Our results confirm that the trends observed previously for the gas-phase adsorption of *CO[5a,b] also persist for the electrochemical adsorption of *H and *OH (consistent with similar investigations by others,[7] there is a linear correlation between the binding energies of *CO and *H, as shown in Figure S4). Placing Cu in the first atomic layer, as in the SA, results in stronger interactions with *H and *OH, whereas placing Cu in the second layer, as in the NSA, weakens the interaction with the same adsorbates. Having established the relationship between the position of Cu and the reactivity of the surface, we will now use this relationship to control the activity for an electrocatalytic reaction: CO adlayer oxidation.

The *CO electro-oxidation voltammogram for Pt(111), Cu/Pt(111) SA, and NSA is shown in Figure 3. The observed area of the CO electro-oxidation peaks can be used to estimate the CO coverage of each surface. For Pt(111), the charge of $328\ \mu C\,cm^{-2}$ corresponds to a coverage of 0.68 monolayers (ML), consistent with 0.7 ML obtained by DFT calculations (Supporting Information) and with previous results.[8] In contrast, the charge of $164\ \mu C\,cm^{-2}$ on the NSA corresponds to a coverage of 0.34 ML, which is in good agreement with the sharp change in CO differential free energy of adsorption at a coverage of 0.33 ML predicted by DFT (Figure S1b). Because both consist of pure Pt atoms in the outer layer, the difference in *CO coverage can only be attributed to the modified electronic properties of the Pt surface atoms. It is interesting to compare the Cu/Pt(111) NSA with $Pt_3Ni(111)$ and $Pt_3Co(111)$, both of which also have first layers of pure Pt atoms.[9] On these bulk alloys, the coverage of *CO approximates that of Pt(111). This is clearly not the case for the NSA, suggesting that the CO electro-oxidation charge may not always provide a one-to-one correlation with the surface area of nanocatalysts with a Pt overlayer.

For the SA, there is also an abrupt change in the calculated CO differential free energy of adsorption when the coverage reaches 1/3 ML, suggesting that this is the equilibrium coverage (Figure S1a). This is consistent with a CO molecule covering each platinum surface atom. However, the rigorous experimental determination of the *CO coverage is challenging; the charge owing to CO electro-oxidation is convoluted with the charge arising from *OH adsorption and Cu dissolution (which starts above 0.7 V).

We compare the catalytic activity of the different surfaces towards CO electro-oxidation by taking into account the position of the main peak, corresponding to terrace-bound *CO.[8] The potential required to oxidize CO increases in the following order: SA < NSA < Pt(111).

To understand this reaction, we consider the following mechanism [Eq. (1)–(3)]:

$$CO(g) + {}^{*} \rightarrow {}^{*}CO \qquad (1)$$

$$H_2O(l) + {}^{*} \rightarrow {}^{*}OH + H^{+}(aq) + e \qquad (2)$$

$$^{*}OH + {}^{*}CO \rightarrow CO_2 + H^{+}(aq) + e^{-} + 2^{*} \qquad (3)$$

Applying a Sabatier analysis,[10] the optimal catalyst for the electrochemcial oxidation of CO must have an intermediate binding energy towards both *CO and *OH.[9]

Figure 4 shows the 3D volcano plot for CO electro-oxidation as a function of the free energies of adsorption of *CO and *OH. In agreement with our experiments, the overpotential required to oxidize CO increases in the following order: SA < NSA < Pt(111). The SA exhibits a lower overpotential for CO oxidation by virtue of its bifunctional nature: *OH binds to Cu sites and *CO binds to Pt.

Strikingly, the volcano plot suggests that the Cu/Pt(111) OL should exhibit optimal activity for *CO electro-oxidation. However, this theoretical prediction could not be realized, since the Cu overlayer is destabilized by the presence of CO.[11] This caused the oxidation of *CO to be accompanied by the dissolution of the Cu (see Supporting Information).

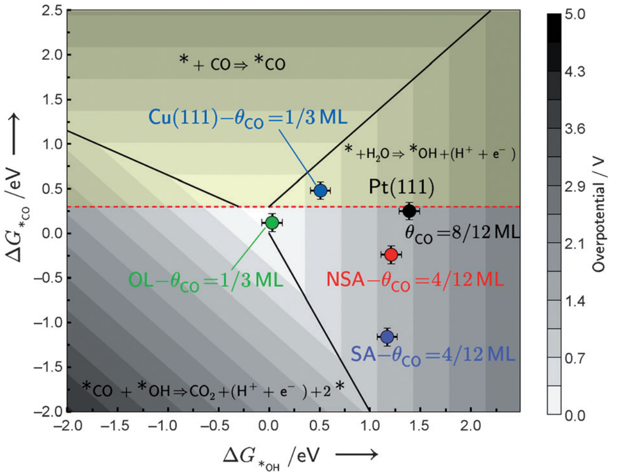

Figure 4. Volcano plot for CO electro-oxidation as a function of the differential free energies of adsorption of CO and OH on different surfaces: Pt(111), Cu(111), Cu/Pt(111) NSA, Cu/Pt(111) SA, and Cu/Pt(111) OL. ΔG_{*CO} is the differential free energy of adsorption of CO when the surfaces are pre-adsorbed with CO, near the corresponding saturation coverage. ΔG_{*OH} is the differential free energy of adsorption of OH co-adsorbed with *CO. The coverage of CO is depicted for each surface. The potential determining step for each region is also defined. The dashed horizontal line denotes the chemical potential of CO in the gas phase, above which CO does not bind to the surface (yellow region).

This illustrates that optimal binding to the intermediates is a necessary but insufficient criterion for an effective catalyst: it must also be stable.[12]

In the NSA, subsurface Cu is kinetically stable below 1.15 V. However, both the SA and the OL are unstable at potentials more positive than 0.7 V, as shown in Figure S5; this observation is consistent with the DFT-calculated dissolution potentials, which are roughly equal for the SA and the OL, as documented in Table S1. Thus the position of the solute metal determines its stability. Less noble metals, which are often alloyed with Pt, such as Ni, Co, Fe, La, or Y, have much lower dissolution potentials than Cu.[13] On the basis of our results, we would not expect these reactive metals to be stable at high potentials in the first surface layer, in contrast to some reports in the literature.[14] The kinetic stability of the solute metal is contingent upon a protective Pt overlayer.

In conclusion, our results demonstrate an unprecedented degree of agreement between electrochemical experiments and first-principle calculations. The location of Cu atoms in Pt(111) controls its interaction with *H, *OH, and *CO. Weakening the binding of CO, by forming a subsurface alloy, can decrease the saturation coverage of CO; thus the CO oxidation charge may not always be a reliable method for the determination of the surface area of nanocatalysts with Pt overlayers. In contrast, Cu atoms in the first layer strengthen the Pt binding energy towards *H, *OH, and *CO. Using this knowledge, we tailored the configuration of Cu atoms in Pt(111) for the electro-oxidation of CO. A large number of electrochemical processes for sustainable fuel production and utilization are controlled by the binding to these adsorbates.[5c,10b,15] Our general approach, outlined here, could enable further progress to be made to the catalysis of these all-important reactions.

Received: July 5, 2012

Keywords: Cu/Pt alloy · cyclic voltammetry · density functional calculations · electrocatalysis · electrochemistry

---

[1] a) H. A. Gasteiger, J. Garche in *Handbook of Heterogeneous Catalysis*, 2nd ed. (Eds.: G. Ertl, H. Knoezinger, F. Schueth, J. Weitkamp), Wiley-VCH, Chichester, **2008**, pp. 3081–3120; b) D. V. Esposito, S. T. Hunt, A. L. Stottlemyer, K. D. Dobson, B. E. McCandless, R. W. Birkmire, J. G. G. Chen, *Angew. Chem.* **2010**, *122*, 10055–10058; *Angew. Chem. Int. Ed.* **2010**, *49*, 9859–9862; c) Y. C. Lu, H. A. Gasteiger, Y. Shao-Horn, *J. Am. Chem. Soc.* **2011**, *133*, 19048–19051; d) I. E. L. Stephens, A. S. Bondarenko, U. Grønbjerg, J. Rossmeisl, I. Chorkendorff, *Energy Environ. Sci.* **2012**, *5*, 6744–6762.

[2] a) H. E. Hoster, M. J. Janik, M. Neurock, R. J. Behm, *Phys. Chem. Chem. Phys.* **2010**, *12*, 10388–10397; b) L. A. Kibler, A. M. El-Aziz, R. Hoyer, D. M. Kolb, *Angew. Chem.* **2005**, *117*, 2116–2120; *Angew. Chem. Int. Ed.* **2005**, *44*, 2080–2084; c) D. S. Strmcnik, D. V. Tripkovic, D. van der Vliet, K. C. Chang, V. Komanicky, H. You, G. Karapetrov, J. Greeley, V. R. Stamenkovic, N. M. Markovic, *J. Am. Chem. Soc.* **2008**, *130*, 15332–15339; d) J. L. Zhang, M. B. Vukmirovic, Y. Xu, M. Mavrikakis, R. R. Adzic, *Angew. Chem.* **2005**, *117*, 2170–2173; *Angew. Chem. Int. Ed.* **2005**, *44*, 2132–2135; e) F. J. Perez-Alonso, D. McCarthy, A. Nierhoff, P. Hernandez-Fernandez, C. Strebel, I. E. L. Stephens, J. H. Nielsen, I. Chorkendorff, *Angew. Chem.* **2012**, *124*, 4719–4721; *Angew. Chem. Int. Ed.* **2012**, *51*, 4641–4643; f) T. F. Jaramillo, K. P. Jorgensen, J. Bonde, J. H. Nielsen, S. Horch, I. Chorkendorff, *Science* **2007**, *317*, 100–102; g) P. Strasser, S. Koh, T. Anniyev, J. Greeley, K. More, C. F. Yu, Z. C. Liu, S. Kaya, D. Nordlund, H. Ogasawara, M. F. Toney, A. Nilsson, *Nat. Chem.* **2010**, *2*, 454–460.

[3] a) S. C. S. Lai, N. P. Lebedeva, T. H. M. Housmans, M. T. M. Koper, *Top. Catal.* **2007**, *46*, 320–333; b) K. J. J. Mayrhofer, M. Arenz, B. B. Blizanac, V. Stamenkovic, P. N. Ross, N. M. Markovic, *Electrochim. Acta* **2005**, *50*, 5144–5154; c) I. Kanezashi, S. Nohara, J. Omura, M. Watanabe, H. Uchida, *J. Electroanal. Chem.* **2011**, *662*, 123–129.

[4] J. Rossmeisl, P. Ferrin, G. A. Tritsaris, A. U. Nilekar, S. Koh, S. Brankovic, P. Strasser, M. Mavrikakis, *Energy Environ. Sci.* **2012**, DOI: 10.1039/C2EE21455E.

[5] a) J. Knudsen, A. U. Nilekar, R. T. Vang, J. Schnadt, E. L. Kunkes, J. A. Dumesic, M. Mavrikakis, F. Besenbacher, *J. Am. Chem. Soc.* **2007**, *129*, 6485–6490; b) K. J. Andersson, F. Calle-Vallejo, J. Rossmeisl, I. Chorkendorff, *J. Am. Chem. Soc.* **2009**, *131*, 2404–2407; c) I. E. L. Stephens, A. S. Bondarenko, F. J. Pérez-Alonso, F. Calle-Vallejo, L. Bech, T. P. Johansson, A. K. Jepsen, R. Frydendal, B. P. Knudsen, J. Rossmeisl, I. Chorkendorff, *J. Am. Chem. Soc.* **2011**, *133*, 5485–5491.

[6] a) A. S. Bondarenko, I. E. L. Stephens, H. A. Hansen, F. J. Pérez-Alonso, V. Tripkovic, T. P. Johansson, J. Rossmeisl, J. K. Nørskov, I. Chorkendorff, *Langmuir* **2011**, *27*, 2058–2066; b) A. Berna, V. Climent, J. M. Feliu, *Electrochem. Commun.* **2007**, *9*, 2789–2794.

[7] a) J. Greeley, M. Mavrikakis, *Catal. Today* **2006**, *111*, 52–58; b) M. P. Humbert, J. G. G. Chen, *J. Catal.* **2008**, *257*, 297–306.

[8] A. Lopez-Cudero, A. Cuesta, C. Gutierrez, *J. Electroanal. Chem.* **2005**, *579*, 1–12.

[9] D. F. van der Vliet, C. Wang, D. G. Li, A. P. Paulikas, J. Greeley, R. B. Rankin, D. Strmcnik, D. Tripkovic, N. M. Markovic, V. R. Stamenkovic, *Angew. Chem.* **2012**, *124*, 3193–3196; *Angew. Chem. Int. Ed.* **2012**, *51*, 3139–3142.

[10] a) H. Falsig, B. Hvolbaek, I. S. Kristensen, T. Jiang, T. Bligaard, C. H. Christensen, J. K. Nørskov, *Angew. Chem.* **2008**, *120*, 4913–4917; *Angew. Chem. Int. Ed.* **2008**, *47*, 4835–4839; b) P. Ferrin, A. U. Nilekar, J. Greeley, M. Mavrikakis, J. Rossmeisl, *Surf. Sci.* **2008**, *602*, 3424–3431.

[11] C. A. Lucas, N. M. Markovic, P. N. Ross, *Surf. Sci.* **2000**, *448*, 77–86.

[12] a) J. Greeley, J. K. Nørskov, *J. Phys. Chem. C* **2009**, *113*, 4932–4939; b) K. J. J. Mayrhofer, K. Hartl, V. Juhart, M. Arenz, *J. Am. Chem. Soc.* **2009**, *131*, 16348–16349; c) S. Chen, H. A. Gasteiger, K. Hayakawa, T. Tada, Y. Shao-Horn, *J. Electrochem. Soc.* **2010**, *157*, A82–A97; d) F. J. Perez-Alonso, C. F. Elkjær, S. S. Shim, B. L. Abrams, I. E. L. Stephens, I. Chorkendorff, *J. Power Sources* **2011**, *196*, 6085–6091.

[13] M. Pourbaix, *Atlas of Electrochemical Equilibria in Aqueous Solutions*, 2nd ed., National Association of Corrosion Engineers, Houston, TX, **1974**.

[14] a) S. J. Yoo, S. J. Hwang, J. G. Lee, S. C. Lee, T. H. Lim, Y. E. Sung, A. Wieckowski, S. K. Kim, *Energy Environ. Sci.* **2012**, *5*, 7521–7525; b) S. J. Yoo, S.-K. Kim, T.-Y. Jeon, S. J. Hwang, J.-G. Lee, S.-C. Lee, K.-S. Lee, Y.-H. Cho, Y.-E. Sung, T.-H. Lim, *Chem. Commun.* **2011**, *47*, 11414–11416; c) X. F. Yang, J. Hu, J. Fu, R. Q. Wu, B. E. Koel, *Angew. Chem.* **2011**, *123*, 10364–10367; *Angew. Chem. Int. Ed.* **2011**, *50*, 10182–10185.

[15] a) A. A. Peterson, F. Abild-Pedersen, F. Studt, J. Rossmeisl, J. K. Nørskov, *Energy Environ. Sci.* **2010**, *3*, 1311–1315; b) J. K. Nørskov, J. Rossmeisl, A. Logadottir, L. Lindqvist, J. R. Kitchin, T. Bligaard, H. Jonsson, *J. Phys. Chem. B* **2004**, *108*, 17886–17892; c) J. K. Nørskov, T. Bligaard, A. Logadottir, J. R. Kitchin, J. G. Chen, S. Pandelov, U. Stimming, *J. Electrochem. Soc.* **2005**, *152*, J23–J26; d) I. C. Man, H.-Y. Su, F. Calle-Vallejo, H. A. Hansen, J. I. Martínez, N. G. Inoglu, J. Kitchin, T. F. Jaramillo, J. K. Nørskov, J. Rossmeisl, *ChemCatChem* **2011**, *3*, 1159–1165.

Angewandte Chemie
Eine Zeitschrift der Gesellschaft Deutscher Chemiker

Supporting Information

69451 Weinheim, Germany

Design of an Active Site towards Optimal Electrocatalysis: Overlayers, Surface Alloys and Near-Surface Alloys of Cu/Pt(111)**

*Aliaksandr S. Bandarenka, Ana Sofia Varela, Mohammedreza Karamad, Federico Calle-Vallejo, Lone Bech, Francisco J. Perez-Alonso, Jan Rossmeisl, Ifan E. L. Stephens, and Ib Chorkendorff**

anie_201205314_sm_miscellaneous_information.pdf

DFT calculations

The total energies of the different adsorbates on each surface were calculated with density functional theory (DFT) using the DACAPO code in the ASE simulation environment with the RPBE exchange-correlation functional. [1] Ion-electron interactions were described by ultrasoft pseudopotentials. The Kohn-Sham one-electron states were expanded in series of plane waves with a converged energy cutoff of 450 eV and a density cut off of 500 eV. The electron density was determined by iterative diagonalization of the Kohn–Sham Hamiltonian using Pulay mixing of electronic densities at an electronic temperature of 0.1 eV and all total energies were extrapolated to $K_BT = 0$ eV. The (111) facet of the face-centered cubic (fcc) metals was considered for all calculations: near surface alloy (NSA), surface alloy (SA), Cu-overlayer (OL), Pt(111) and Cu(111).

For the NSA, we assumed a subsurface concentration of 2/3 ML Cu. This is on the basis of our earlier experiments that show that when 1 ML is deposited initially, 0.6 ML reside in the subsurface, following the annealing.[2] For the SA, a surface concentration of 2/3 ML Cu was assumed, also on the basis of our earlier investigations.[3] For the OL. a complete pseudomorphic monolayer was assumed.

The surfaces were modeled using four-layer $\left(2\sqrt{3} \times 2\sqrt{3}\right)R30^{\circ}$ and $\left(\sqrt{3} \times \sqrt{3}\right)R30^{\circ}$ slabs repeated in a super cell geometry with 14 Å of vacuum between successive slabs. Moreover, adsorption was allowed only on one of the exposed surfaces and dipole corrections were used. All *OH and *H adsorption calculations were performed at a coverage of 1/3 ML, whereas the coverage of 1/3ML was assumed for *CO on all surfaces except for Pt(111) where 2/3ML of *CO was considered.

In all calculations, the bottom two layers were fixed in their bulk structure while the top two layers and adsorbates on them were allowed to relax in all directions until the maximum force on any atom was below 0.05 eV $Å^{-1}$. Monkhorst-Pack grids with dimensions $3 \times 3 \times 1$ and $6 \times 6 \times 1$ were used for sampling the Brillouin zones of the surface $\left(2\sqrt{3} \times 2\sqrt{3}\right)R30^{\circ}$ and $\left(\sqrt{3} \times \sqrt{3}\right)R30^{\circ}$ structures respectively. All adsorption sites (atop, bridge and hollow) were considered and only the most stable ones are used here. Lattice constants of 4.02 and 3.71 Å were used for Pt and Cu respectively, and the lattice constants of the alloys and OL were assumed to be the same as that of the substrate metal. All free energies are calculated relative to H_2O(l), CO_2(g) and H_2(g). Zero-point energies and entropies were included in energetic calculations.[4] We considered solvation effects on all surfaces by assuming that *OH and *CO exposed to liquid water are stabilized by approximately 0.5 and 0.1 eV respectively, as suggested by Peterson el al.[4a] We would like to emphasize that the stabilization of *OH by water in the bilayer depends on the coverage of *CO. When Pt(111) is at its saturation coverage of 2/3 ML of *CO, we do not anticipate any stabilization of the *OH by the water in the bilayer.[5] However, when the surface is pre-dosed with *CO, *CO electrooxidation initiates at the step sites, where *OH adsorption is more favorable than on terrace sites.[6] When the first few CO molecules are oxidized, they leave behind free sites where water can be adsorbed and hence stabilize adsorbed *OH. Thus, the reaction of terrace-bound *CO and *OH is unlikely until the potential where a significant amount of *OH is able at the terraces in the absence of *CO, ~0.7V (see Figure 2 of the main text), which corresponds to the onset of the main peak for *CO oxidation. We note that this is not the case for NSA and SA. On these alloys, due to the lower coverage of *CO, there are already free sites between adsorbed *CO molecules where water can be adsorbed before *CO oxidation takes place._The free energy of gas-phase CO_2 was also corrected by 0.45 eV, accounting for the inaccurate description of gas-phase CO_2 within the RPBE formalism.[4b] We have used the computational hydrogen electrode approach introduced by Nørskov et al.[4, 7] In this model, the electrode potential, U (versus the reversible hydrogen electrode), is taken into account by shifting the electron energy by $-eU$ when an electron is transferred. The overpotential is defined as the maximum positive free energy difference ~~among~~ between each two successive reaction steps.

Equilibrium coverage calculations

The equilibrium CO coverages for the Cu/Pt(111) SA and NSA were calculated using the integral and differential free energies of adsorption. The integral energy is the total adsorption energy of all adsorbed CO molecules on the surface (relative to CO in the gas phase) per surface metal atom. It can also be calculated as the product between the average free energy and the CO coverage. The differential free energy of adsorption is calculated by differentiating the integral free energy with respect to CO coverage.[8] It defines the most stable CO coverage (assuming negligible co-adsorption of other species, the CO coverage should be potential independent, as CO adsorption is not an electrochemical step). Eq(1) shows the relation between average and differential free adsorption energy of CO :

$$G_{diff}(\theta)=d(G_{int})/d(\theta)=d(G_{avg}\theta)/d(\theta) \qquad (1)$$

Where θ, G_{diff}, G_{int} and $G_{avg}$are the coverage, differential, integral and average free energies of adsorption of CO, respectively.

Figure S1 shows the differential free energy of adsorption on Cu/Pt(111) SA, NSA and Pt(111). For the SA and NSA, there is a an abrupt discontinuity at $\theta = 0.33$ ML . In the case of the SA, this is due to a change in the adsorption site. For CO coverages below 0.33 ML, CO molecules adsorb on atop sites of Pt atoms on the SA. However, when the coverage exceeds 0.33 ML, additional CO starts occupying atop sites of Cu atoms, explaining the discontinuity observed at this coverage for the Cu/Pt(111) SA (figure S1.*a*). On the contrary, for the NSAs, the adsorption sites do not change upon increasing the coverage of CO above 0.33 ML. Consequently, the abrupt change in the differential free energy on the NSAs could be explained as a change in adsorbate-adsorbate interactions. Below 0.33 ML, there would be negligible interaction between neighboring CO molecules, whereas above 0.33 ML there would be repulsive interactions. For Pt(111), starting at very low coverage of CO, both the adsorption sites and the number of CO molecules occupying specific adsorption sites change upon continuously increasing the coverage of CO. For example, while at $\theta = 0.12$ ML both atop and fcc hollow sites are occupied, upon increasing the coverage to 0.19 ML just fcc hollow sites are occupied and at $\theta = 0.5$ ML there is an equal mix of atop and bridge sites. At $\theta = 0.5$ ML, the lateral interactions increase significantly, causing an abrupt discontinuity, but the adsorption of CO is still energetically favorable up to $\theta = 0.7$ ML.

The equilibrium coverage of CO should be set at the point where $G_{diff} = 0$. According to the plots in Figure S1, this takes place at $\theta = 0.33$ ML for the SA and $\theta = 0.44$ ML for the NSA and $\theta = 0.7$ML for Pt(111). In the case of the NSA, this value is comparable, albeit slightly higher than the experimental value. However, given the uncertainty in the DFT calculations of ~ 0.3 eV , it is quite plausible that the coverage at which $G_{diff}=0$ would actually correspond to the discontinuity, i.e. at 0.33 ML, explaining the experimentally determined CO coverage.[9] A similar analysis would also be applicable for the SA, where it was not possible to accurately determine the experimental value of θ.

The equilibrium coverage of *O and *OH on the Cu/Pt(111)OL were also calculated following the same scheme used for *CO, except that we assumed 0.5 eV stabilization for *OH due to solvation effect. On the OL, the *O coverage is not influenced by the presence of co-adsorbed water. While the coverage of *OH is 0.3 ML, the coverage of *O is very low at U=0 V.

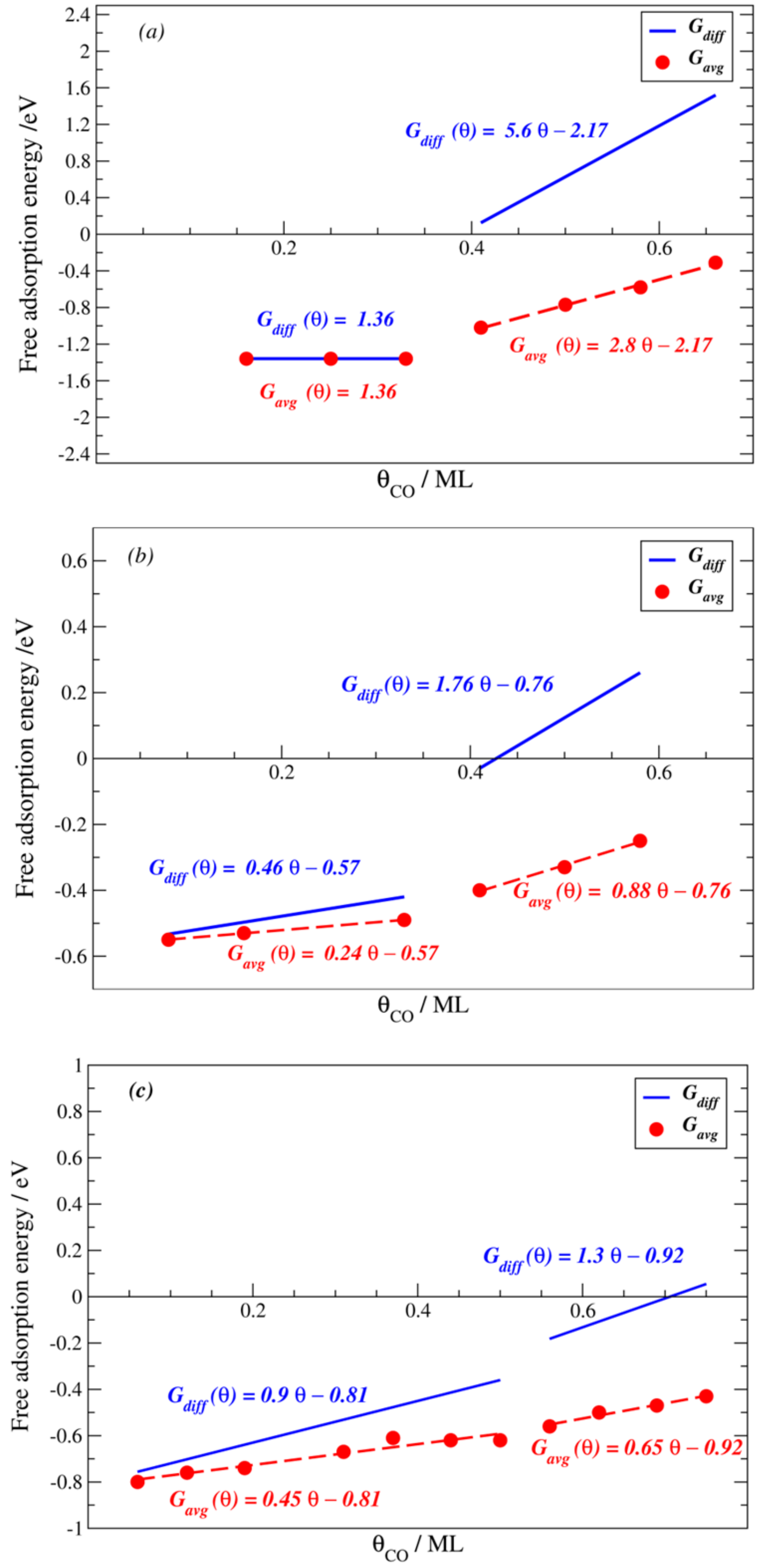

Figure S1. Differential free energy of adsorption of CO on (*a*) surface alloy, (*b*) near surface alloy, and (*c*) Pt(111). The red points are the calculated average adsorption energy at different coverages of CO and the red dashed lines are the fit to them at different coverage regimes.

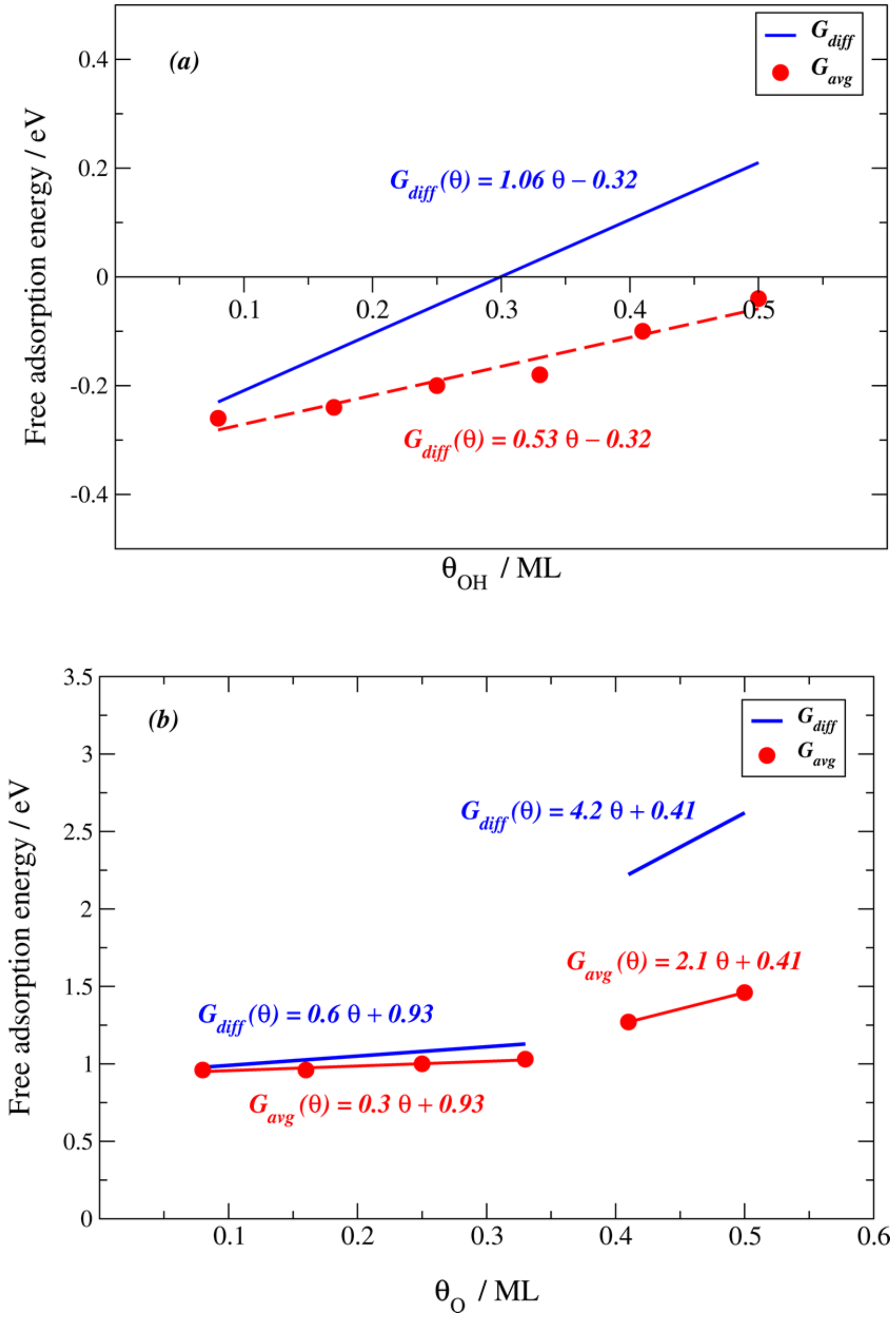

Figure S2. Differential free energy of adsorption of OH (a) and O (b) on the Cu-overlayer at U = 0 V. For OH, the solvation effects have been taken into account.

Binding energy calculations

The calculated binding energies of *H, *OH and *CO on different surfaces are shown in Figure S3. Consistent with experimental results, the binding energies of the different adsorbates are strongly dependent on the location of the Cu atoms. On the NSA, OL and Cu(111), the binding energies of *OH and *H and *CO are weaker than on Pt(111), when compared at a given coverage. However, on the Cu/Pt(111) SA, the binding energies for the same adsorbates are stronger than on Pt(111). Somewhat counterintuitively, for Pt(111), at the experimentally determined CO coverage of 0.66 ML, the integral CO adsorption energy is weaker than on the NSA. However, at 0.33 ML, the CO binding energy is stronger on Pt(111) than on the NSA.

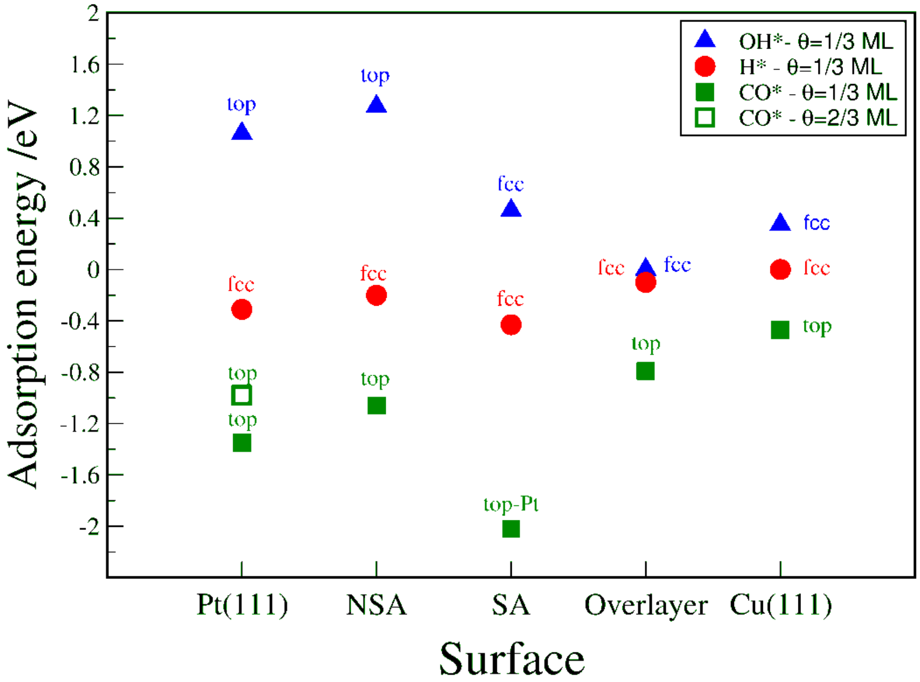

Figure S3. Binding energies of OH, H and CO on different surfaces referenced to H_2O(l), H_2(g) and CO(g) respectively. The adsorption site for each adsorbate is provided.

We note that, the trend in H adsorption correlates well with that of CO on all of the Cu/Pt(111) systems under study, as shown on Figure S4, consistent with the literature.[10]

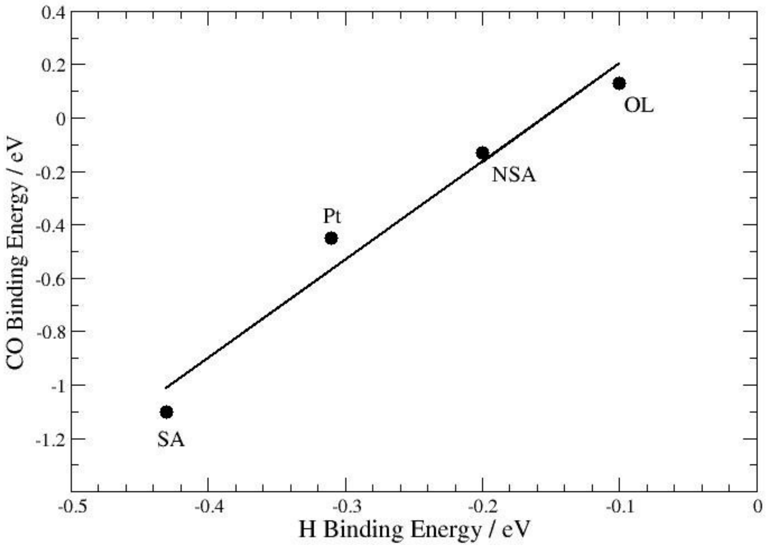

Figure S4: Correlation between hydrogen and CO binding energies on different Cu/Pt(111) systems referenced to H_2(g) and CO(g) respectively.

Volcano plot for CO adlayer electro-oxidation

In order to study the electrochemical oxidation of a CO adlayer we have considered the following steps:

$CO(g) + * \rightarrow *CO$ (2)

$H_2O(l) +$ ~~*~~$*CO \rightarrow *CO + {}^{*}OH + H^{+}(aq) + e^{-}$ (3)

$*OH + *CO \rightarrow CO_2\,(g) + H^{+}(aq) + e^{-} + 2*$ (4)

The first two are elementary reaction steps whereas the last involves both the recombination and the charge transfer step. We assume that CO desorption is irreversible, i.e. that there is no readsorption of CO, via (2) during the course of the oxidation experiment. This assumption is only appropriate for the electo-oxidation of pre-adsorbed *CO when CO is absent from the solution. However, it is not appropriate for the electo-oxidation of CO when CO is dissolved in the solution. The * refers to free sites onto which *CO and *OH can bind, located on a surface which has been preadsorbed with CO to near-saturation CO coverage. It is important to note that these sites can be different, which makes it possible to design bifunctional sites on the catalyst surface, as it is the case of the surface alloy. In addition, there is no direct scaling between the OH and CO binding energies. This means that the two reactivities can be varied more or less independently, making it possible to have surface sites at which both the OH and CO reactivities are optimal.

A good catalyst for the electrochemical CO oxidation has to be able to effectively catalyze the three reaction steps given above. It has to bind CO(g), it has to activate water and form *OH, and it has to bind CO and OH not so strongly that it becomes difficult to form CO_2. The free energies of the three reaction steps gives are the following:[9]

$$\Delta G_1 = \Delta G_{*_{CO}} = G(CO^*) - G(CO(g)) - G(*) \qquad (5)$$

$$\Delta G_2 = \Delta G_{*_{OH}} = G(*OH+*CO) + \tfrac{1}{2}G(H_2) - G(H_2O(l)) - G(*CO) - eU - kT\ln(a_{H^+})$$
(6)

$$\Delta G_3 = G(CO_2(g)) + \tfrac{1}{2}G(H_2) + 2G(*) - G(^*OH) - G(^*CO) - eU - kTln(a_{H^+}) \qquad (7)$$

Where the term $(1/2\,G(H_2) - eU - kT\ln(a_{H^+}))$ is the chemical potential of electrons and protons using the computational standard hydrogen electrode.[7] ΔG_1, ΔG_2 and ΔG_3 have to simultaneously be as close to zero as possible. We note that, while these are necessary criteria for good catalysts, there could easily be additional criteria other than those considered here. For example, step 3 involves two elementary steps,[6b] which could mean that ΔG_3 could be more accurately described if further deconvoluted. Only two parameters are catalyst dependent and they are the free energy adsorption of CO, $\Delta G_{*_{CO}}$ ~~$G(^*CO)$~~ and the free energy of adsorption of OH, $\Delta G_{*_{OH}}$ ~~$G(^*OH)$.~~This means that we can plot the overpotential ~~catalyst activity~~ as a function of these two parameters.[7] As discussed above, the overpotential is defined as the maximum positive energy difference between each two successive reaction steps. Mathematically, it can be written as below:

$$U_{\mathrm{Overpotential}} = Max\left[\Delta G_1, \Delta G_2^{\circ}, \Delta G_3^{\circ}\right]/e$$

Where ΔG_{2-3}° are the changes in free energies of the respective ΔG_{2-3} reactions at $U = 0$ vs Reversible Hydrogen Electrode (RHE). Since the first step of the reaction, the adsorption of CO is potential independent, when $\Delta G_1 > 0$ CO does not bind to the surface, regardless of the potential and the reaction will simply not take place.

The activity of the surface toward electrochemical CO oxidation can be related to the overpotential in a simple way without taking into account the kinetics details. We assume that the activation barrier for each electron-proton transfer step is equal to corresponding free energy change and that the trends in the overpotential represent the trends in the activity.[7]

We would like to emphasize that the trends in the overpotential do not go hand-in-hand to experimental measured activity as the kinetics details are not taken into accounts. However, this approach gives us an important insight in understanding the trend in the catalytic activity of electrochemical CO oxidation on different surfaces. The volcano plot for the electrochemical CO oxidation is plotted in Fig. S5 against the free energies of the involved intermediates, *CO and *OH.

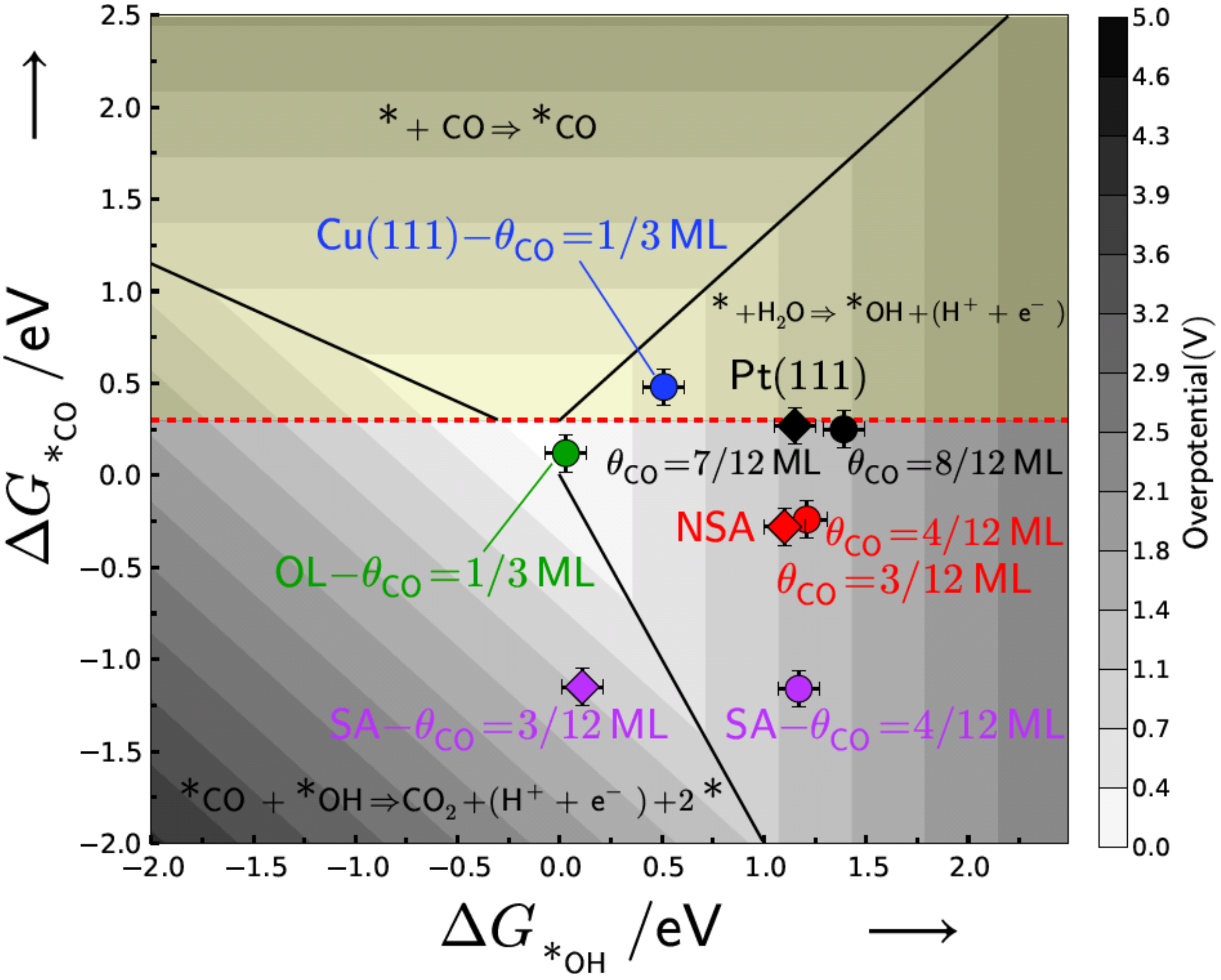

Figure S5. Volcano plot for CO electro-oxidation as a function of the differential free energies of adsorption of CO and OH on different surfaces: Pt(111), Cu(111), Cu/Pt(111) NSA, Cu/Pt(111) SA and Cu-overlayer. $\Delta G_{*_{\mathrm{CO}}}$ is the differential free energy of adsorption of CO when the surfaces are pre-adsorbed with CO, near the corresponding saturation coverage. $\Delta G_{*_{\mathrm{OH}}}$ is the differential free energy of adsorption of OH coadsorbed with CO. The CO coverages are provided for each surface. The circles show the overpotential for CO electro-oxidation when the CO coverage is 2/3 and 1/3 ML on Pt(111) and all the other surfaces, respectively. Diamonds show the overpotential for CO electro-oxidation on NSA, SA and Pt(111) when the CO coverage is 1/12 ML lower than the corresponding saturation coverages. The potential determining step for each region is also provided. The dashed horizontal line denotes the chemical potential of CO in the gas phase, above which value CO does not bind to the surface (yellow region).

Figure S5 shows the volcano plot of the overpotential towards the electrochemical CO oxidation as a function of the free energies for its intermediates, *CO and *OH. The *CO binding energy has been plotted (a) at the most stable coverage of *CO, and (b) at a *CO coverage 1/12 of a monolayer lower than the most stable coverage for the respective structures. This slightly lower coverage would more accurately model the effect of the change in coverage during the course of the voltammogram. The same trends persist at both coverages, i.e. that the overpotential for the reaction increases in the following order: Cu/Pt(111) overlayer < Cu/Pt(111) SA < Cu/Pt(111)

NSA < Pt(111). The figure also shows that Cu(111) is unable to activate *CO, as its binding energy is too weak in comparison to the chemical potential of gas-phase CO.

For all structures, the activity towards *CO electro-oxidation is slightly improved when the *CO coverage is lower, meaning that when *CO starts to be oxidized the reaction becomes more favourable [6b], in agreement with earlier experimental studies. Furthermore, Figure S5 shows that that by lowering the *CO coverage on the Cu/Pt(111) SA, the limiting step changes from the *OH adsorption to CO2 desorption, since at a lower *CO coverages there are more available sites where *OH binds more strongly. In other words, for the lower coverages of *CO on the Cu/Pt(111) SA , *OH binds to the fcc site formed from Cu and Pt atoms. This site is more stable than atop Cu, which is the most stable adsorption site for the equilibrium coverage of *CO of 1/3 ML.

It is worth perusing upon the effect of defects upon the CO-electroxidation activity of the catalysts under study. We do not know what exact form the defects would take on the alloy surfaces under investigation. Nonetheless, we know from earlier surface science studies of these single crystal alloys that the (111) terraces are well ordered.[3, 11]

For Pt(111), there is a general consensus in the literature that the pre-peak, starting at ~0.5 V, is due to CO oxidation facilitated by defects in the crystal whereas the main peak, whose onset starts at 0.7 V and reaches a maximum at ~0.75 V, is primarily due to the reaction of terrace-bound *CO and *OH.[6] According to Figure S5, *OH activation is potential determining for Pt(111), consistent with the literature.[6b] The effect of the defects on the position of the main peak would be related to the decrease in total coverage of *CO, relative to the saturation coverage, that occurs during the pre-peak. As shown in the figure, decreasing the local coverage of CO, where the reaction takes place, from 2/3 ML to 7/12 ML results in a slight decrease of the theoretical overpotential. The local coverage would be primarily determined by the total coverage of CO and its surface diffusivity or mobility.[6b] If we were to assume that the CO is immobile, and that *OH nucleates and grows from the step, the local coverage of *CO would be high at the sites where the reaction takes place. On the other hand, if we were to assume that the CO is highly mobile, then the local coverage of *CO would be slightly lower than the saturation coverage, due to the amount oxidized in the pre-peak. As the voltammogram proceeds beyond the onset of the main peak, the coverage of *CO would decrease and the coverage of *OH would increase, bringing about an autocatalytic effect to the reaction.

In the case of the NSA, there is only a single peak in the stripping voltammogram shown on Figure 3 of the main article text, starting at ~0.6 V and reaching a maximum at ~0.7 V. This absence of a pre-peak is consistent with the notion that the oxidation only occurs at one site, presumably the terrace, and that the role of defects may be less important. Consequently, to model the onset of the peak, it would be appropriate to consider that the coverage is equal to the saturation coverage.

On the CO stripping voltammogram of the SA, shown in Figure 3 of the main body text, there is a pronounced pre-peak, starting at ~0.4 V. The main peak starts at ~0.6 V and reaches a maximum at ~0.65 V. We propose that the pre-peak corresponds to *CO oxidation, facilitated by defects, similar to Pt(111). As shown in the Figure, at the saturation coverage of 1/3 ML *CO, *OH activation is potential determining. However, it can be deduced from Figure S5 that decreasing the coverage of *CO from 1/3 ML to 3/12 ML strengthens the *OH binding by ~1 eV. Therefore, the removal of a small amount of *CO would significantly facilitate the adsorption of *OH; this would mean that the CO oxidation current in the pre-peak would be concomitant with that of *OH adsorption (in the absence of *CO, *OH would be adsorbed at ~0.3 V, as shown in Fig 2 of the main body text). Assuming that amount of *CO oxidized in the pre-peak brings about a lower local *CO coverage where the reaction takes place, at the onset of the main peak, it would be more appropriate to model the reaction at 3/12 ML coverage. At this lower local coverage the reaction rate or overpotential would be limited by the electrochemical recombination of *CO and *OH.

To summarize the above, we anticipate that the pre-peaks exhibited by Pt(111) and the SA are due to defects. The effect of the defects would be to decrease the total *CO coverage on these surfaces at the onset of the main peak, where terrace bound *CO and *OH react. However, as discussed earlier, the reaction overpotential, or catalytic activity, is only slightly sensitive to the *CO coverage for the surfaces under study. At both saturation coverages and slightly lower coverages of *CO, the theoretical model is able to describe the experimental data, where the overpotential increases in the following order: SA < NSA < Pt(111).

Cu dissolution potentials:

In order to calculate the dissolution potential of Cu in different Cu/Pt(111) systems, we consider following derivation.[12] By assuming standard hydrogen electrode as the reference state, electrode reaction that describes the dissolution potential of the metal A in the alloy constituting from A and B atoms, A/B, $\mathrm{A/B} \rightarrow \mathrm{B/B} + \mathrm{A}^{n+} + ne^{-}$,can be written as follows:

$$\mathrm{A/B} + \mathrm{nH}^{+} \rightarrow \mathrm{B/B} + \mathrm{A}^{n+} + \frac{1}{2}\mathrm{H}_2$$

The dissolution potential of metal A in the alloy is related to the chemical potentials through the following equation:

$$U_{diss-A} = (E_{B/B} - E_{A/B} + NE_{A-Bulk} - NE_{B-Bulk} + NnU_{diss-A,Bulk})/n$$

Where $\mathrm{U_{diss-A}}$ is the dissolution potential of metal A in the alloy (from DFT), $\mathrm{E_{B/B}}$ is the total energy of the pure B metal slab (from DFT), $\mathrm{E_{A/B}}$ is the total energy of the alloy slab (from DFT), N is the number of alloying metal atoms (A) per unit cell in the alloy slab, $NE_{\mathrm{A-Bulk}}$ is the total energy of bulk A atoms (from DFT), $\mathrm{NE_{B-Bulk}}$is the total energy of bulk B atoms (from DFT), n is the number of electrons involved in the dissolution of A atoms (n = 2 in the case of Cu dissolution) and $\mathrm{U_{diss-A,Bulk}}$ is the dissolution potential of bulk A atoms. In the calculations for dissolution potential of Cu in different Cu/Pt(111) systems, the value of $U_{diss-Cu,Bulk}$ was taken for a pH of 1 and a Cu concentration of 10^{-6} M.[13] Table 1 shows the dissolution potentials of the Cu in different Cu/Pt(111) systems. It should be noted that the experimentally observed dissolution potentials may be significantly more positive, due to additional kinetic barriers.

Cu/Pt(111) System	Dissolution Potential / V (RHE)
NSA	0.48
SA	0.29
Overlayer	0.28

Table S1: Dissolution potentials of Cu in different Cu/Pt(111) systems.

Preparation of Cu/Pt(111) monolayer, NSA and SA

Pt(111) single crystals, with a diameter of 5mm oriented to < 0.1° and polished to the surface roughness 30nm were used (Mateck, Julich, Germany). Before experiments, the Pt(111) crystals were annealed at 850±20°C in a H_2(5%)+Ar atmosphere for 6 min, followed by annealing in a CO(0.1%)+Ar atmosphere for 2 min at 850±20°C.

The Cu/Pt(111) monolayer was prepared by Cu underpotential deposition (UPD) on Pt(111). The deposition of 1 ML of Cu was performed in 0.1 M $HClO_4$ with 2 mM Cu^{2+}, at 0.4V RHE, for 3 minutes, under which conditions a pseudomorphic Cu overlayer on Pt(111) should be formed.[14] The deposited amount of Cu was controlled by the charge required for the anodic dissolution of the Cu overlayer.

The Cu/Pt(111) NSA was obtained by annealing the Cu/Pt(111) monolayer during 2 minutes at 400°C in Ar/H_2 atmosphere (5% of H_2 in Ar). The SA was subsequently obtained by annealing the Cu-Pt(111) NSA for 2 minutes in Ar/CO atmosphere (0.1% of CO in Ar) and afterwards cooling in the same atmosphere. Adsorbed CO was then electrochemically oxidized in 0.1M $HClO_4$ at 0.57V RHE. The temperature during annealing was controlled with a K-type (Ni/Cr+Ni/Al) thermocouple attached to the back side of the crystal. In-depth surface composition information for the Cu/Pt(111) NSA and SA samples was extracted from angle resolved X-ray photoelectron spectroscopy (AR-XPS) spectra recorded using a Theta Probe instrument from Thermo Scientific. The procedure is described in detail elsewhere.[15]

The system used to prepare the near-surface alloy and surface alloy consists of a custom made electrochemical cell with an induction heater directly attached. The electrochemical component consisted of a Pt counter electrode, a mercury/mercury sulfate reference electrode, and the Pt(111) single crystal as the working electrode, in a hanging meniscus configuration. The atmosphere was controlled through gas inlet and outlet ports. The counter electrode was attached to the cell via a port connecting to a separate purging compartment, with its own gas inlet. This compartment allowed the electrolyte (or rinsing water) to be purged of air, prior to its entry into the working compartment of the cell.

The position of the single crystal could be controlled vertically so it could be lifted up and annealed by the induction heater without the need to expose it to air.

After the experiments, the SA- and NSA-samples were the subject for a special treatment in order to remove surface and subsurface Cu and restore the initial Pt(111) surface. For that, the samples were cycled in 0.1M $HClO_4$ between 0.05V and 1.45V(RHE) for few hours at the scan rate 50 mV/s. Afterwards, the crystals were annealed in Ar/H_2 and Ar/CO atmosphere. Cyclic voltammetry, X-ray photoelectron spectroscopy, and low-energy electron diffraction, ion scattering spectroscopy were used to ensure that the Pt(111) surface was restored and no Cu was present close to the surface.

Electrochemical measurements

A Biologic Instruments SP-150 potentiostat was used to control the measurements.

Before the experiments, the cell was cleaned for 24 hours in a "piranha" solution consisting of a mixture of 96% H_2SO_4 and 30% H_2O_2 (3:1), followed by multiple heating/rinsing with Millipore water (18.2 MΩ cm) to remove sulfates. Swagelok stainless steel tubes were used to supply CO, Ar, Ar/H_2 and Ar/CO pure gases and gas mixtures into the cell. Plastic tubing was avoided to minimise outgassing of organic contamination.

Each experiment was conducted in 0.1 M $HClO_4$ (Merck, Suprapur) in ultrapure water (Millipore Synergy Pak UV >18.2 M Ω cm, 22±2°C).

For the Cu UPD, 0.1M CuO (Aldrich, 99.9999%) was dissolved in a solution of 0.3M $HClO_4$, before adding an aliquot of this solution to the electrolyte to obtain a Cu^{2+} concentration of 2mM.

Stability measurments

DFT calculations predict that Cu in the first layer is oxidized at the same potential on the Cu/Pt(111) OL and on Cu/Pt(111) SA. Experimentally we observed the onset potential for Cu oxidation from the Cu/Pt(111) SA to be around 0.75V (figure S5*a*), which is similar to the stripping potential of copper from the Cu/Pt(111) ML (shown as an insert in figure S5*a*). However, the shape of the oxidation peak is significantly different for these two surfaces. The sharp oxidation peak observed on the Cu/Pt(111) ML indicates strong attractive interactions between copper atoms so when a copper atom is removed, the whole copper monolayer becomes unstable.[16] On the other hand, the broad Cu oxidation peak on the SA could be because the Pt atoms are not dissolved at these potentials. Consequently, Cu dissolution from the SA would result in vacancy or Pt island formation in the surface, which would be less energetically favourable [17] than the simultaneous removal of the first surface layer which occurs in the case of the OL structure. [12],[18]). After Cu stripping from the SA, the voltammogram is drastically different (Fig. S5*b*) compared to that for the initial Pt(111) surface and the corresponding voltammogram for the NSA (see Figs in the manuscript). The voltammogram shown in Fig. S1*b* is rather a fingerprint of a markedly defective surface (peaks in H* adsorption/desorption region and a broader and less reversible OH* adsorption/desorption peaks) [19]. This behavior is expected after Cu removal from the first platinum layer. Notably, after Cu overlayer oxidation from the Pt(111) and subsequent rinsing with 0.1M HClO$_4$ under potential control to remove Cu^{2+}, it was not possible to restore the surface to the initial cyclic voltammogram characteristic of a well ordered Pt(111) surface. The voltammogram of Pt(111) could only be restored if the Cu stripping from the surface alloy was followed by high temperature annealing.

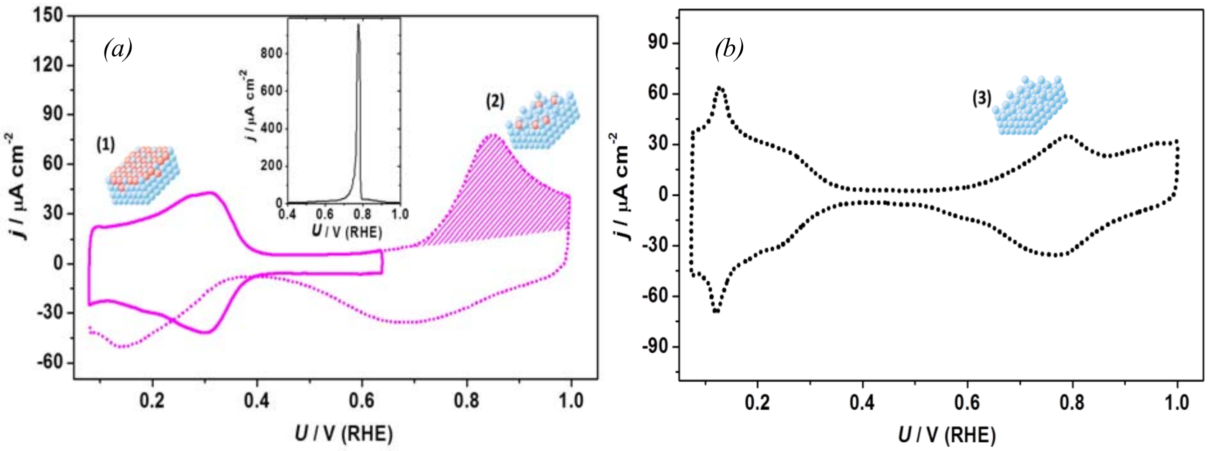

Figure S5: Cyclic voltammograms taken in 0.1M HClO$_4$ characterizing *(a)* (*1*) Cu-Pt(111) SA, (*2*) oxidation of Cu from the Cu-Pt(111) SA and *(b)* (*3*) defective platinum surface remaining after Cu atoms were stripped out from the surface alloy (20th cycle is shown in *b*). Dashed line in *a* also shows the first cycle after Cu oxidation from the SA-surface. d*E*/dt = 50 mV/s

CO displacement and adlayer oxidation on the Cu/Pt(111) overlayer

According to the volcano plot shown in Figure S5, the Cu/Pt(111) overlayer structure should have the very high activity for CO adlayer oxidation, because of its optimal binding to *CO and *OH. However, experiments by Markovic, Ross and co-workers suggest that this structure should be unstable in the presence of CO. [20] They reported that when CO was adsorbed at 0.35V on a Cu/Pt(111) overlayer in perchloric acid solution, the CO displaced the *Cu, leading to its dissolution as Cu^{2+}. Their results suggest that it should not be possible to carry out CO adlayer oxidation on this structure, as the *CO oxidation would instead take place on a clean Pt(111) surface. To clarify this issue, we carried out CO displacement and adlayer oxidation experiments on the Cu/Pt(111) overlayer. In particular, we aimed to answer the following questions (a) does the adsorption of CO result in the displacement of *Cu or the displacement of O* or OH*? (b) do the observed phenomena observed show any potential dependence? (c) if the *Cu is stable, what is its activity for *CO oxidation?

The CO displacement experiments were conducted in accordance to the procedure described by Clavilier and co-workers. [21] Once the Cu monolayer was deposited, the potential was fixed at a given value while the current was recorded. CO was dosed to the cell trough a gas inlet situated 1 cm away from the meniscus, generating a current response.[21] (Figure S6) Once the measured current reached a stable value, the CO flux was stopped. Subsequently, the cell was purged with Ar for 30 minutes under potential control. Finally, the potential was swept to positive values to electrooxidize the adsorbed *CO.

For this study we selected four different potential (0V, 0.1V 0.22V and 0.32V) and repeated the measurements at least two times per selected potential. We observed that there is a strong dependence between the adsorption potential and the obtained charge. (Figure S7). The charge generated during CO adsorption is due to the displacement of charged species in the interphase. For the Cu/Pt(111) overlayer, we expect these displaced species to be *O, *OH, *Cu, either separately or in combination.

In agreement with Ross and coworkers' results,[20] at sufficiently positive potentials, in this case 0.32V (RHE), CO adsorption results in a positive current, consistent with the displacement of a positively charged species, i.e. the dissolution of *Cu. The observed charge of 140μC/cm^2 is smaller than 480μC/cm^2 expected for the oxidation of a full Cu monolayer, since the displacement of copper is accompanied by *OH and *O displacement that produce a negative charge. Furthermore, the cyclic voltammogram for CO electrooxidation, after holding the potential at 0.32V resembles CO electrooxidation on Pt(111). These results confirm that when the CO is adsorbed at 0.32 V, the *Cu is displaced from the surface.

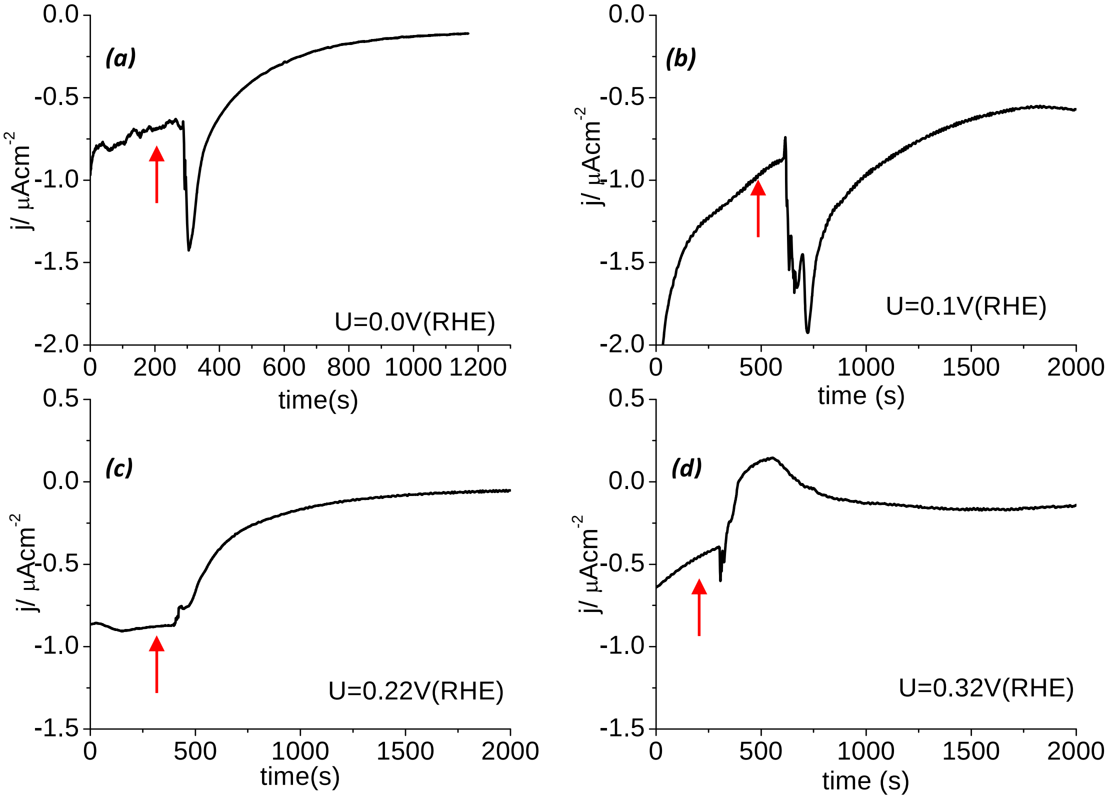

Figure S6: Measured current during the CO adsorption at a fixed potential (*U*=0.0V (*a*), *U*=0.1V (*b*) *U*=0.22V (*c*) and *U*=0.32V (*d*)) The red arrow indicates the time at which CO was dosed into the cell.

On the contrary, when the potential is held at 0.1V and at 0 V (RHE) a negative charge is observed, suggesting the dissolution of a negatively charged species, such as *OH or *O. This confirms the output of the theoretical calculations, which suggested that *O or *OH desorb from the surface. The negative charge of $213\mu C/cm^2$ observed at 0.1V would correspond to close to 1 monolayer of *OH or 1/2 a monolayer *O, while the coverage predicted by DFT are only 0.3 ML for *OH and nearly zero for *O (figure S2). This discrepancy suggests that the measured charge may not only be attributable to chemisorption but also to dipole rearrangements at the interphase.[22] It is also worth noticing that the charge obtained at 0V is considerable different from that obtained at 0.1V, this could be attributed to the adsorption of *H close to 0V. When the CO was adsorbed at 0.22 V, there is no measurable charge. This indicated that at this potential, CO adsorption results in desorption of both positive and negative species, resulting in a net displacement charge of zero.

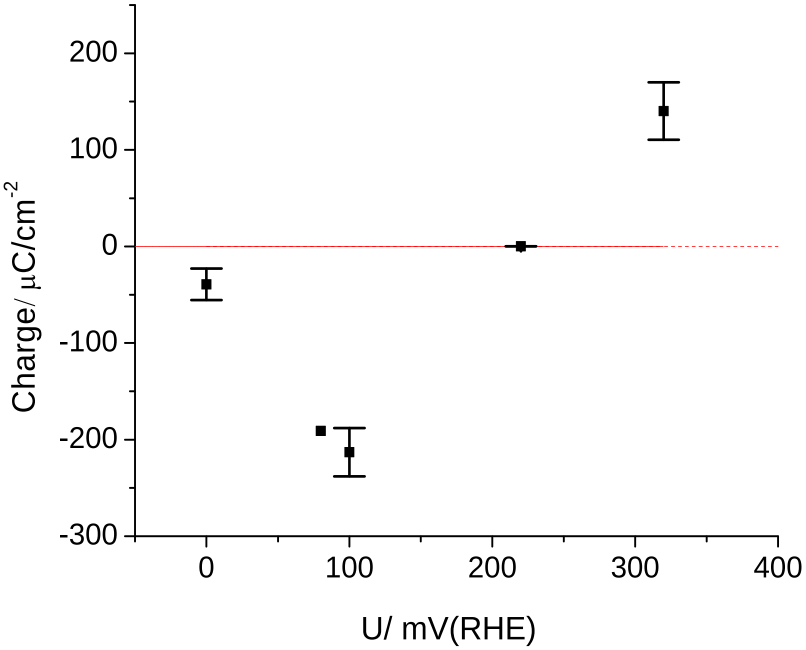

Figure S7: Charge generated during the CO displacement as a function of the adsorption potential.

In summary, the CO displacement experiments confirm that the Cu/Pt(111) overlayer is stable below 0.1 V. At more positive potentials, *Cu is displaced by *CO. This instability of *Cu makes it challenging to obtain reproducible results for the electrochemical oxidation of *CO on the Cu/Pt(111) overlayer. Figure S8 shows the *CO stripping voltammogram on Cu/Pt(111) overlayer after adsorbing CO at a 0.1V (RHE). We interpret the peak at 0.6 V to be *CO oxidation. Consistent with the predictions from theory (see Figure S5), it seems to occur at lower overpotentials that for the other surfaces. We attribute the peak starting at ~0.7 V to be *Cu dissolution. However, the peak is not as sharp as for Cu/Pt(111) overlayer in the absence of *CO, as shown in the inset in Figure S5a. This suggests that some structural changes have occurred to the overlayer during the course of *CO adsorption and oxidation. It is also conceivable that there could be some residual *CO at the surface above ~0.7 V, and that its oxidation would be concomitant with that of Cu in this potential range.

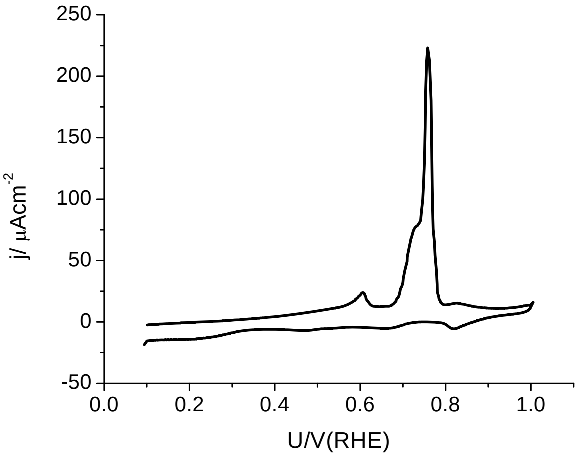

Figure S8: Anodic stripping voltammograms for CO electro-oxidation on Cu/Pt(111) monolayer at 20mV/s

REFERENCES

[1] S. R. Bahn, K. W. Jacobsen, *Comput. Sci. Eng.* **2002**, *4*, 56-66.

[2] I. E. L. Stephens, A. S. Bondarenko, F. J. Pérez-Alonso, F. Calle-Vallejo, L. Bech, T. P. Johansson, A. K. Jepsen, R. Frydendal, B. P. Knudsen, J. Rossmeisl, I. Chorkendorff, *J. Am. Chem. Soc.* **2011**, *133*, 5485-5491.

[3] K. J. Andersson, F. Calle-Vallejo, J. Rossmeisl, I. Chorkendorff, *J. Am. Chem. Soc.* **2009**, *131*, 2404-2407.

[4] aA. A. Peterson, F. Abild-Pedersen, F. Studt, J. Rossmeisl, J. K. Nørskov, *Energy Environ. Sci.* **2010**, *3*, 1311-1315; bP. Ferrin, A. U. Nilekar, J. Greeley, M. Mavrikakis, J. Rossmeisl, *Surf. Sci.* **2008**, *602*, 3424-3431.

[5] D. S. Strmcnik, D. V. Tripkovic, D. van der Vliet, K. C. Chang, V. Komanicky, H. You, G. Karapetrov, J. Greeley, V. R. Stamenkovic, N. M. Markovic, *J. Am. Chem. Soc.* **2008**, *130*, 15332-15339.

[6] aA. Lopez-Cudero, A. Cuesta, C. Gutierrez, *J. Electroanal. Chem.* **2005**, *579*, 1-12; bS. C. S. Lai, N. P. Lebedeva, T. H. M. Housmans, M. T. M. Koper, *Top. Catal.* **2007**, *46*, 320-333; cH. S. Wang, Z. Jusys, R. J. Behm, H. D. Abruna, *J. Phys. Chem. C* **2012**, *116*, 11040-11053.

[7] J. K. Nørskov, J. Rossmeisl, A. Logadottir, L. Lindqvist, J. R. Kitchin, T. Bligaard, H. Jonsson, *Journal of Physical Chemistry B* **2004**, *108*, 17886-17892.

[8] E. Skulason, V. Tripkovic, M. E. Bjorketun, S. Gudmundsdottir, G. Karlberg, J. Rossmeisl, T. Bligaard, H. Jonsson, J. K. Nørskov, *J. Phys. Chem. C* **2010**, *114*, 18182-18197.

[9] B. Hammer, L. B. Hansen, J. K. Norskov, *Physical Review B* **1999**, *59*, 7413-7421.

[10] aJ. Greeley, M. Mavrikakis, *Catal. Today* **2006**, *111*, 52-58; bM. P. Humbert, J. G. G. Chen, *J. Catal.* **2008**, *257*, 297-306.

[11] J. Knudsen, A. U. Nilekar, R. T. Vang, J. Schnadt, E. L. Kunkes, J. A. Dumesic, M. Mavrikakis, F. Besenbacher, *J. Am. Chem. Soc.* **2007**, *129*, 6485-6490.

[12] J. Greeley, J. K. Nørskov, *Electrochimica Acta* **2007**, *52*, 5829-5836.

[13] M. Pourbaix, *Atlas of Electrochemical Equilibria in Aqueous Solutions*, Second ed., National Association of Corrosion Engineers, Houston, Texas, **1974**.

[14] E. Herrero, L. J. Buller, H. D. Abruna, *Chem. Rev.* **2001**, *101*, 1897-1930.

[15] A. S. Bondarenko, I. E. L. Stephens, I. Chorkendorff, *Electrochemistry Communications* **2012**, *in press DOI: 10.1016/j.elecom.2012.06.030.*

[16] J. Greeley, *Electrochimica Acta* **2010**, *55*, 5545-5550.

[17] R. Jinnouchi, E. Toyoda, T. Hatanaka, Y. Morimoto, *J. Phys. Chem. C* **2010**, *114*, 17557-17568.

[18] P. Strasser, S. Koh, J. Greeley, *Physical Chemistry Chemical Physics* **2008**, *10*, 3670-3683.

[19] J. Clavilier, A. Rodes, K. Elachi, M. A. Zamakhchari, *Journal De Chimie Physique Et De Physico-Chimie Biologique* **1991**, *88*, 1291-1337.

[20] aC. A. Lucas, N. M. Markovic, B. N. Grgur, P. N. Ross, *Surf. Sci.* **2000**, *448*, 65-76; bC. A. Lucas, N. M. Markovic, P. N. Ross, *Surf. Sci.* **2000**, *448*, 77-86.

[21] J. Clavilier, R. Albalat, R. Gomez, J. M. Orts, J. M. Feliu, A. Aldaz, *J. Electroanal. Chem.* **1992**, *330*, 489-497.

[22] R. Guidelli, W. Schmickler, in *Modern Aspects of Electrochemistry, Vol. 38* (Ed.: B. E. Conway), Kluwer Academic-Plenum Publishers, New York, **2005**, pp. 303-371.

JOURNAL OF CHEMICAL EDUCATION

Electrochemical Hydrogen Evolution: Sabatier's Principle and the Volcano Plot

Anders B. Laursen,*[†] Ana Sofia Varela,[†] Fabio Dionigi,[†] Hank Fanchiu,[∥] Chandler Miller,[∥]
Ole L. Trinhammer,[§] Jan Rossmeisl,[‡] and Søren Dahl[†]

[†]CINF and [‡]CAMD, and [§]Department of Physics, Technical University of Denmark, 2800 Kgs. Lyngby, Denmark
[∥]Cal Energy Corps, University of California, Berkeley, California 94720, United States

Ⓢ *Supporting Information*

ABSTRACT: The electrochemical hydrogen evolution reaction (HER) is growing in significance as society begins to rely more on renewable energy sources such as wind and solar power. Thus, research on designing new, inexpensive, and abundant HER catalysts is important. Here, we describe how a simple experiment combined with results from density functional theory (DFT) can be used to introduce the Sabatier principle and its importance when designing new catalysts for the HER. We also describe the difference between reactivity and catalytic activity of solid surfaces and explain how DFT is used to predict new catalysts based on this. Suited for upper-level high school and first-year university students, this exercise involves using a basic two-cell electrochemical setup to test multiple electrode materials as catalysts at one applied potential, and then constructing a volcano curve with the resulting currents. The curve visually shows students that the best HER catalysts are characterized by an optimal hydrogen binding energy (reactivity), as stated by the Sabatier principle. In addition, students may use this volcano curve to predict the activity of an untested catalyst solely from the catalyst reactivity. This exercise circumvents the complexity of traditional experiments while it still demonstrates the trends of the HER volcano known from literature.

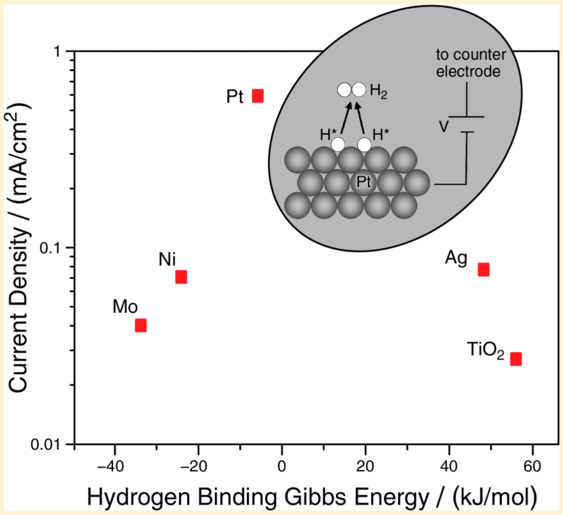

KEYWORDS: *High School/Introductory Chemistry, First-Year Undergraduate/General, Laboratory Instruction, Laboratory Instruction, Physical Chemistry, Hands-On Learning/Manipulatives, Catalysis, Electrolytic/Galvanic Cells/Potentials, Metals, Surface Science*

Electrochemistry gains ever more attention as the need for sustainable energy, often electrical, increases. It is therefore important to introduce students to electrocatalysis. A novel way of introducing students to the Sabatier principle (also see the laboratory exercise in ref 1) is presented and can be used to understand trends in catalytic activity in combination with density functional theory (DFT). This is achieved through a simple exercise using the classic electrochemical reaction for the hydrogen evolution reaction (HER) from water electrolysis:[2,3]

$$2H^+(aq) + 2e^- \leftrightarrow H_2(g) \quad (1)$$

Through this exercise, students test the HER activity of Mo, Ni, Ag, Pt, and TiO_2 and use these activities to understand the way in which DFT calculations and practical electrochemical experiments are used together to predict new catalysts for electrocatalytic reactions.

■ THEORY

It has been shown that the binding energy of the intermediates in a reaction determines how well a catalyst works. Generally, in catalysis, the unlikely situation of more than two molecules colliding simultaneously in the gas phase is circumvented by the binding of the reagents to a surface—thereby dividing the collisions into several sequential steps. That is, the first molecule will collide with the surface resulting in a bound intermediate and the second molecule then collides with the intermediate and reacts and so forth for additional steps. When this occurs, the reagents' internal bonds may be weakened due to the interaction with the catalyst, thereby lowering the energy barrier for a reaction. Hence, a catalyst should bind strongly to the reagents and intermediates so that they are likely to adsorb to the surface, allowing the reaction to occur. However, if the catalyst binds the intermediates or products too strongly, the products formed on the catalyst cannot desorb, leaving the catalyst inhibited. Thus, the Sabatier principle states that the optimal catalyst binds a key intermediate strongly enough so

Published: September 17, 2012

that the reagents will likely bind and react, but weakly enough so that the product will easily desorb.

When the activity of catalyst materials are plotted versus reactivity, a peak-shaped curve known as the Sabatier plot or volcano curve is obtained.[4] This plot clearly illustrates the difference between the reactivity and activity of various catalysts. Reactivity, given by the binding energy of the key intermediate, indicates how much the catalyst interacts with the reactants—positive values indicate a weak interaction and vice versa. Reactivity is in this work obtained from DFT. Activity, which depends on reactivity, is the measured rate of the catalytic reaction and is usually described per unit surface area. In this work, the measured rate is the current per area of the electrode from electrochemical experiments, as this is a direct measure of the electrons consumed in the HER, and the data from the DFT calculations are provided to the students.

EXPERIMENT

Experimental Overview

In the experiments, the students use different materials for the working electrode and measure the current obtained at a given potential to assess the activity of the metal. The measurements are carried out in a simple two-electrode compartment setup described below.

Electrode Preparation

The following electrodes were used:

- Molybdenum foil (Sigma-Aldrich) 3 × 0.5 × 0.05 cm,
- Nickel foil (Goodfellow) 3 × 0.5 × 0.05 cm,
- Silver foil (Goodfellow) 1.5 × 0.5 × 0.05 cm,
- Titanium foil (Sigma-Aldrich) 3 × 0.5 × 0.025 cm,
- Platinum wire (Goodfellow) 1.5 (length) × 0.05 (diameter) cm,
- One carbon rod (Ted Pella, Inc.) 4 cm (length) × 0.25 in. (diameter).

To make the surface of the titanium foil into a thick oxide layer, the foil was sanded and then put in a muffle oven at 200 °C in air for 20 min. All electrodes were masked with nail polish to allow more accurate measurements of the exposed surface areas. To ensure that only a clean nonoxidized metal was exposed to the electrolyte, each electrode, *except* titanium, was sanded with the same type of fine-grade sandpaper on the area exposed to the electrolyte. All circuit contact points were sanded, regardless of the material. The sanding was done immediately prior to starting each measurement.

Experimental Procedure

The two-electrode setup consisted of two 100 mL beakers filled with 0.1 M H_2SO_4 as an electrolyte and connected by a KNO_3 salt bridge (Figure 1). One beaker contained the foil or wire to be measured (working electrode) and was connected to the negative outlet. Nitrogen or argon (AGA technical purity) was bubbled through the solution and the beaker covered with plastic film (household or Parafilm). This kept the beaker with the working electrode essentially free of oxygen, preventing the competing oxygen reduction reaction. The other beaker contained a graphite rod (counter electrode) and was connected to the positive outlet of the power supply. The electrodes were connected to two multimeters: one in parallel with the power supply to measure the applied potential and the other in series between the counter electrode and the power supply to measure the current.

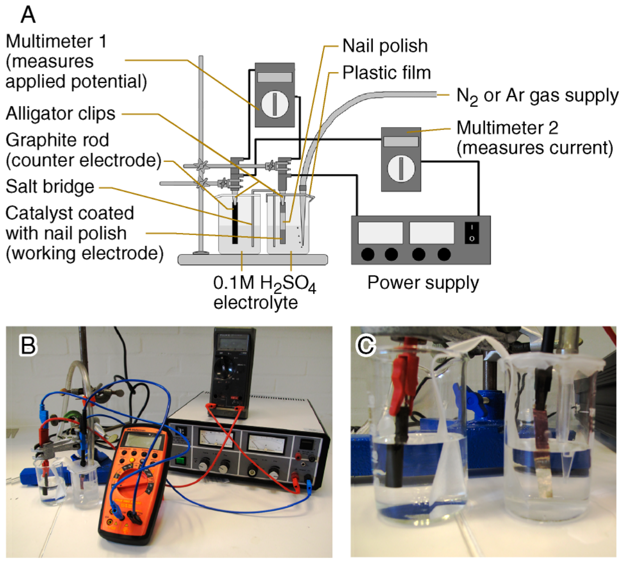

Figure 1. The experimental setup as a (A) schematic drawing, (B) photo of setup, and (C) close-up photo of the electrochemical cell.

With the power supply turned on, the potential was gradually raised to 3 V, held for 3 min, and then lowered to 1.7 V, at which point the current was recorded after the second decimal place had stabilized for 10 s. To ensure accuracy, both the current and potential were measured and adjusted to two decimal places precision, respectively. After the measurement, the working electrode was changed to a new material, and the procedures were repeated.

The precautions for the potentials were taken to ensure that the electrode surface was reduced to the metallic state and not an oxide and that any oxygen introduced by the electrode was completely removed by oxygen reduction. Furthermore, the potential was increased slowly to prevent overloading the multimeters.

Data Processing

Data processing was done by dividing each measured current by the surface area exposed to the electrolyte to obtain the current density. The electrode area is obtained by considering each foil as two rectangular surfaces or the wire as a cylinder. As all electrodes were sanded with the same grade sandpaper, each surface roughness was approximately the same. The resulting values were plotted on a base-10 logarithmic axis versus the corresponding DFT-calculated hydrogen binding Gibbs energy (linear axis) to obtain the Sabatier plot. The exercise required approximately 1 h and 45 min in total: 30 min for setup, 45 min for measurements, and 30 min for data treatment.

HAZARDS

As with all lab experiments, standard safety procedures should be obeyed. Goggles, gloves, and lab coats should be worn at all times. Concentrated sulfuric acid is corrosive and contact can cause severe damage to skin and eyes. The power supplies used here was limited to deliver no more than 10 V and 14 mW.

DENSITY FUNCTIONAL THEORY

To calculate the binding Gibbs energy of the key intermediate for any given reaction, one must know or assume the reaction mechanism. In the case of the HER, there are two proposed reaction mechanisms: the Volmer−Tafel mechanism

$$2(H^+(aq) + e^- + *) \leftrightarrow 2H^* \leftrightarrow H_2(g) + 2* \quad (2)$$

and the Volmer–Heyrovsky mechanism

$$2H^+(aq) + e^- + * \leftrightarrow H^* + H^+ \leftrightarrow H_2(g) + * \quad (3)$$

where the asterisk (*) indicates an empty active site and the H* indicates a hydrogen atom bound to the active site (Figure 2). Both reactions give the overall reaction shown in eq 1.

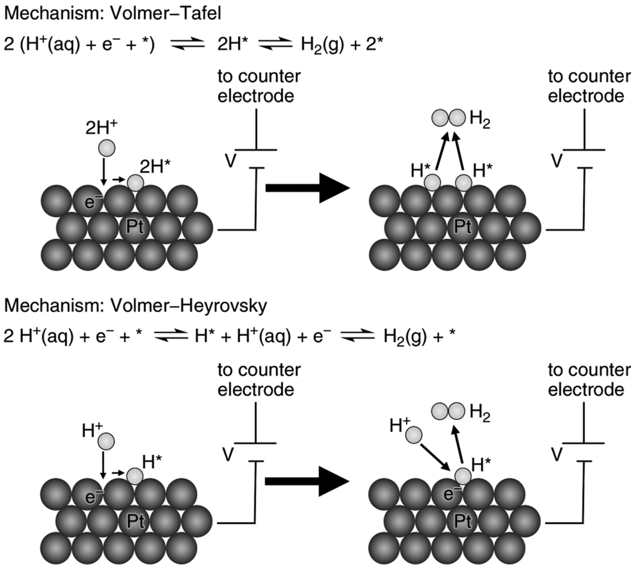

Figure 2. Two mechanisms for the HER reaction: the Volmer–Tafel mechanism and the Volmer–Heyrovsky mechanism on platinum surfaces. The asterisk (*) represents a free active site, whereas H* indicates that the hydrogen atom is bound to the active site.

Regardless of the mechanism, hydrogen is the only intermediate binding to the catalyst and DFT is used to calculate the binding Gibbs energy of hydrogen to the investigated catalysts. The DFT calculation uses the atomic position of the nuclei and the atomic charge to calculate the total energy of a system. In this case, the binding energy of the hydrogen atom to the surface is obtained by subtracting the energy of surface-bound hydrogen from the energy of the clean surface and half the energy of a free hydrogen molecule. Then, using simple estimates for entropy and zero-point energy, the Gibbs energy of binding hydrogen at standard conditions is obtained.[5] This simple method allows the screening of many catalyst systems for HER as for other catalytic reactions. The surfaces investigated in this study with their hydrogen binding Gibbs energies are listed in Table 1.

Table 1. DFT-Calculated Binding Energies for the Bonding of Hydrogen to the Surface of Molybdenum, Nickel, Silver, Titanium Dioxide, and Platinum

Catalyst Material	Binding Gibbs Energy/(kJ/mol)	Experimental Current/(mA/cm^2)
Mo	−33.8	0.025
Ni	−24.1	0.045
Ag	48.2	0.082
TiO_2	56.0	0.016
Pt	−5.8	0.500

RESULTS

The experiment gives a set of currents at a fixed potential for several electrode materials. The resulting current density is plotted versus the hydrogen binding Gibbs energy obtained using DFT calculation. Data generated from the instructor is shown in Figure 3A and by the students in Figure 3B.

As expected, the catalyst electrodes lie on a volcano curve when plotted against the hydrogen bonding Gibbs energies, obtained from theoretical calculations.[6] The peak of the volcano is close to the hydrogen binding Gibbs energy $\Delta G_H = 0$ kJ/mol, in accordance with predictions from literature.[6,7] Furthermore, platinum is located near the top, as it is the best material known for the HER. This illustrates that our simple experimental setup gives the activity behavior expected from more detailed studies.[8]

It should be noted that the potential for this comparison is not chosen arbitrarily. Using lower potentials than the one stated results in currents that are too small for precise measurement in this setup. By contrast, using larger potentials causes the activity of the electrode to be limited by the diffusion of protons to, and gas away from, the electrode. Unavoidable electrical resistances in the circuit will also influence the result if the measurements are done at larger currents.

In Figure 3B, the data obtained from a group of students are plotted versus the hydrogen binding energy from Table 1. It was observed that some students sanded the TiO_2 electrode surface, thereby removing the oxide layer and exposing the pure metallic titanium. Some students also did not sand the electrode contact point. Both gave rise to erroneous results (Not shown in Figure 3B). Additionally, one group experienced decreased activity, likely due to the electrode oxidizing in the electrolyte. It is therefore emphasized that the students should polish the electrodes immediately before submerging them into the electrolyte and that the current is recorded after the second decimal place of the current measurement stabilizes. Usual student data varied with around 6–69% from the data shown here. However, the discrepancy does not significantly affect the logarithmic trends of the Sabatier plot and is thus an indication of the robustness of the experimental procedure.

DISCUSSION

Electrolysis is a well-known method for producing hydrogen from water using electrical energy, and is expected to gain more importance in the future when we have to rely more on renewable energy. The HER is the cathodic half-reaction occurring during electrolysis[9] and is well understood in terms of trends in activity. From the previously stated reaction schemes, eqs 2 and 3, for catalytic hydrogen production, it can be concluded that hydrogen bound to the electrode surface is a key intermediate, regardless which mechanism applies. Hence, this is the key intermediate binding energy calculated in this study, as well as in literature in general.

In literature, one may find Sabatier curves for the HER where the exchange current density is plotted as a function of hydrogen's binding energy.[5,10] However, the measurement of the exchange current density is cumbersome and the concept is above the introductory level intended here. Figure 3 shows that the obtained experimental results also produce a volcano curve similar to that observed in literature, signifying that this simple exercise gives reasonably accurate results. The advantage of this experiment is that, through a simple exercise, students are able to make Sabatier plots and predict the peak to be at least close

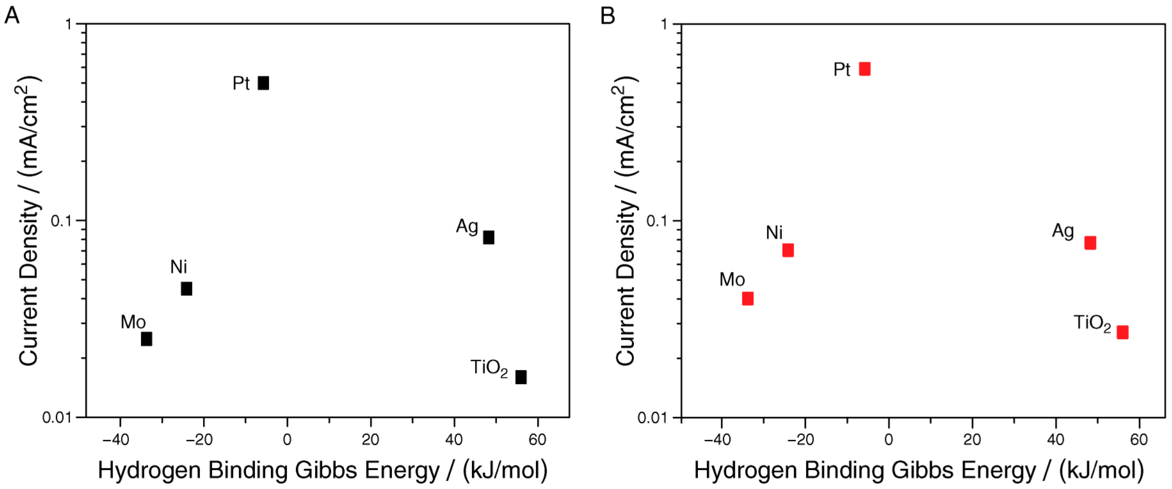

Figure 3. Sabatier plot of the activity of the measured catalysts (A) by the instructors and (B) by students versus the reactivity described by the DFT calculated hydrogen binding energy. Potential: 1.7 V.

to $\Delta G_H = 0$ kJ/mol, which according to previous DFT studies is the top of the volcano.[5,10]

In addition, this experiment effectively demonstrates the difference in electrocatalytic activity obtained using different metals, thereby revealing the reason why platinum is so commonly used in electrolysis units. A discussion with the students on what criteria a catalyst should fulfill is encouraged. Factors such as cost, activity, abundance, and toxicity should be noted.

To demonstrate how the volcano may be used, students were asked to locate the top of the volcano by linear regression, using the measurements for molybdenum and nickel to obtain the left side and silver and titanium dioxide to obtain the right side. Figure 4 shows the resulting volcanoes for the instructor data and for student data. The two predictions fall within 40 kJ/mol from the known peak at 0 kJ/mol. Even though the prediction is not 0 kJ/mol, it is rare that a perfect volcano is found for any Sabatier plot and even rarer that it holds for such a simple experimental setup. This is what makes this experiment a powerful demonstration of how theory and experiments may be used together.

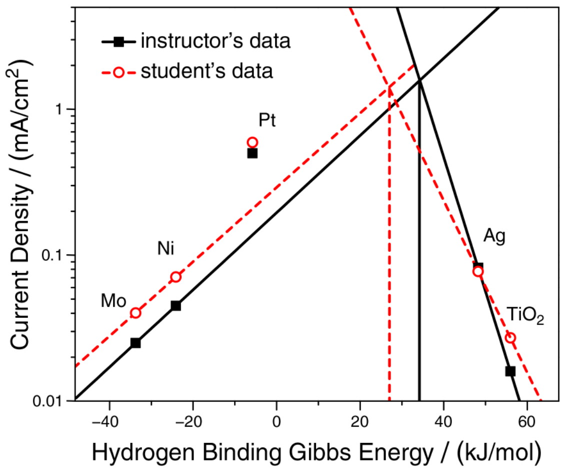

Figure 4. Results of predicting the volcano top by linear regression for the instructor data (square) and for the student data (circle). Potential: 1.7 V.

EXPERIMENTAL VARIATIONS

As a variation of this experiment, students can be suggested to test only the Mo, Ni, Ag, and TiO_2 electrodes and to predict the activity of Pt when given the corresponding hydrogen binding energy. The instructor should then measure the activity of Pt as a demonstration, and students should discuss how the measurement compares with their predictions. This exercise would allow students to understand the predicting power of the Sabatier plot. In addition, there would be a decrease in cost, as only one Pt electrode is needed.

Another experiment could be to measure the potential needed to obtain a current density of approximately 2 mA/cm^2. This resembles a working electrolysis unit more closely, as the current is constant and the potential varied. A volcano is also obtained in this case, when plotting the potential on the logarithmic *y* axis versus the hydrogen Gibbs binding energy. This affords an understanding of how the electrode material greatly affects the potential and energy required to drive the hydrogen production. The difficulty is that students should know the electrode area before measuring to calculate the actual current they need.

CONCLUSION

A simple and inexpensive way of allowing students to have hands-on experience with electrochemical measurements has been devised. Not only does the exercise demonstrate the Sabatier principle through experiments and theoretical calculations, it also shows how the latter is translated into a Sabatier plot. Experimenting with cost-effective and non-hazardous materials such as Ni, Mo, Ag, and TiO_2, students can understand the predictive power of DFT calculations using the Sabatier plot. In addition, the experiment is easy to conduct and requires minimal equipment and preparation. A group of 9th grade students successfully completed and understood the exercise. However, for full benefit, this exercise is recommended for upper-level high school students and undergraduate students.

ASSOCIATED CONTENT

Ⓢ Supporting Information

Notes for the instructor and student instructions. This material is available via the Internet at http://pubs.acs.org.

AUTHOR INFORMATION

Corresponding Author

*E-mail: ablaursen.chemistry@gmail.com.

Notes

The authors declare no competing financial interest.

ACKNOWLEDGMENTS

We gratefully acknowledge the Danish Ministry of Science for funding the CAtalysis for Sustainable Energy (CASE) initiative and Mårten Björketun for the DFT calculations.

REFERENCES

(1) Laursen, A. B.; Man, I. C.; Trinhammer, O. L.; Rossmeisl, J.; Dahl, S. *J. Chem. Educ.* **2011**, *88*, 1711−1715.

(2) Eberhardt, W. H. *J. Chem. Educ.* **1927**, *4*, A591.

(3) Heidman, S. *J. Chem. Educ.* **1986**, *63*, 809−810.

(4) Bligaard, T.; Nørskov, J. K.; Dahl, S.; Matthiesen, J.; Christensen, C. H.; Sehested, J. *J. Catal.* **2004**, *224*, 206−217.

(5) Nørskov, J. K.; Bligaard, T.; Rossmeisl, J.; Christensen, C. H. *Nat. Chem* **2009**, *1*, 37−46.

(6) Nørskov, J. K.; Bligaard, T.; Logadottir, A.; Kitchin, J. R.; Chen, J. G.; Pandelov, S.; Stimming, U. *J. Electrochem. Soc.* **2005**, *152*, J23−J26.

(7) Parsons, R. *Trans. Faraday Soc.* **1958**, *54*, 1052−1063.

(8) Trasatti, S. *J. Electroanal. Chem.* **1972**, *39*, 163−184.

(9) While the hydrogen evolution reaction is taking place at the cathode, an oxidation reaction is occurring at the anode. If we consider that the process taking place is the water electrolysis, the expected anodic reaction is oxygen evolution reaction (OER):

$$2H_2O \rightarrow O_2 + 4H^+ + 4e^-$$

This reaction generates the protons used in the cathode for the HER and completes the water splinting into hydrogen and oxygen. In this case, we can consider that the overall process is

$$2H_2O \rightarrow H_2 + O_2$$

However, there is also the possibility that the carbon of the counter electrode is being oxidized evolving CO_2 instead of O_2. This will occur following the equation:

$$C + 2H_2O \rightarrow CO_2 + 4H^+ + 4e^-$$

Here, as in the case of OER, protons are formed too, while the split water is used to slowly oxidize the graphite electrode.

(10) Skulason, E.; Tripkovic, V.; Bjorketun, M. E.; Gudmundsdottir, S.; Karlberg, G.; Rossmeisl, J.; Bligaard, T.; Jonsson, H.; Nørskov, J. K. *J. Phys. Chem. C* **2010**, *114*, 18182−18197.